Perovskite Materials for Multi-Junction Solar Cell Applications



David P. McMeekin

Linacre College

Department of Physics

University of Oxford

A thesis submitted in fulfilment of the requirements for the degree of Doctor of Philosophy at the University of Oxford

Hilary, 2018

Perovskite Materials for Multi-Junction Solar Cell Applications

David P. McMeekin, Linacre College, University of Oxford

Thesis submitted for the degree of Doctor of Philosophy at the University of Oxford. Hilary, 2018

Abstract

The work presented in this thesis will describe studies on organic-inorganic perovskite materials when being used in tandem and multi-junction solar cell architectures. Perovskite solar cells (PSC) have recently emerged as a viable absorber material for photovoltaic applications, owing to its remarkable optoelectronic properties along with its ease of fabrication. These attributes have led to a rapid progress in device performance, where over the last few years, perovskite solar cells have reached efficiencies that other solar technologies took decades to achieve. Moreover, one unique economic advantage of this technology is its ability to offer solution-processible fabrication. This characteristic enables perovskites to be applied to existing large-scale deposition techniques on rigid or flexible substrates such as roll-to-roll (R2R) processing, blade coating or inkjet printing techniques. These large area film manufacturing techniques have the promise of drastically lowering solar cell fabrication costs and thus transforming the global energy landscape. By offering an affordable and renewable energy source to satisfy our ever-increasing energy needs, the emerging perovskite solar technology can help lead the fight against climate change.

Initially, the work presented in chapters 1 and 2 will serve as an introduction to the theory, background and motivation for the investigation of perovskite solar cells in multi-junction solar cell applications. We also discuss the difficulties encountered by the research community when attempting to design and fabricate a perovskite material suitable for tandem and multi-junction applications. We present in chapter 3 the experimental methods used throughout the thesis.

In chapter 4, we introduce a perovskite system that is suitable for tandem applications with c-Si solar cells. This highly crystalline and efficient formamidinium-cesium mixed-cation lead mixed halide $[HC(NH_2)_2]_{(1-x)}Cs_xPb(I_{(1-y)}Br_y)_3$ exhibits improved thermal and photo-stability over the conventional methylammonium lead mixed halide perovskite $CH_3NH_3Pb(Br_{(1-y)}Br_{(1-y)})_3$. By combining a 1.74 eV $[HC(NH_2)_2]_{0.83}Cs_{0.17}Pb(I_{0.6}Br_{0.4})_3$ perovskite material with a crystalline silicon (c-Si) solar cell, we demonstrated a highly efficient 4-terminal tandem architecture. This paved the way for perovskite materials to be utilized in tandem application with the established c-Si. Chapter 5 will discuss the crystallization kinetics and the control of morphology of this formamidinium-cesium mixed-cation lead mixed-halide perovskite system. We show that colloids, present in the precursor solution in the form of lead polyhalides: $[PbX_3]^{1-}$, $[PbX_4]^{2-}$, $[PbX_5]^{3-}$, $[PbX_6]^{4-}$, can serve as nucleation centers and impact the

final morphology and optoelectronic properties of the perovskite film. Highly crystalline perovskite material with low electronic disorder and long-lived carrier lifetimes can be obtained through careful consideration of the precursor solution. Finally, in chapter 6, we demonstrate fully solution-processed monolithic all-perovskite tandem and triple-junction solar cells. The ability to sequentially process a perovskite layer on top of underlying perovskite layers opens new possibilities for large scale manufacturing of multi-junction perovskite solar cells. The work presented in this thesis demonstrates the feasibility of using perovskite materials as an absorber in tandem and multi-junction solar cell applications.

Acknowledgements

First, I would like to thank my research supervisor, Professor Henry J. Snaith, who has supported and guided me throughout my DPhil. Henry's inexhaustible enthusiasm for science has given me the motivation and courage to persevere through this incredible journey. Henry has never adhered to the idea that everything has been done, which gave me the confidence to identify and solve complex scientific problems. His endless stream of ideas and suggestions sparked the passion and devotion needed to finish this project.

I would like to thank all my past colleagues at Cyrium Technologies for all the mentorship and support they have provided along the way, notably, Simon Fafard, Eric Desfonds, Denis Masson, Steve Wallace, Norbert Puetz, Aline Rugwizangoga, Francine Proulx, Sarah Langstaff, Bruno Riel, Chris Valdivia, Jian Li and Gauthamy Sangarapillai. Cyrium introduced me to the world of research and development, material science and solar cells. This initial exposure caught my scientific curiosity for years to come, which ultimately lead me to the world of perovskite solar cells.

I would also like to thank my family. Dad, thank you for supporting me throughout this DPhil and for having a keen interest in my research. Thank you for the ongoing encouragement you gave me, from very early in my life, to pursue knowledge in mathematics, engineering and sciences. Maman, thank you for your love and support across an ocean during all my studies abroad. Thank you for all your emails of encouragement and care packages that made me feel a little bit closer to home. Kathleen and Kevin, our common interest in science and our love for the preservation of the environment was a big motivator for this thesis, thank you for all your visits, throughout my studies, in Courléon, Lausanne and Oxford. I would like to thank Nadeshda for her love and support, which kept my spirits up over these last three years. Our time spent between Oxford, London, Leiden and New York, along with our trips across Europe and Australia, has meant the world to me.

I would like to thank all my colleagues in Oxford who made the office and the lab an enjoyable workplace to exchange and discuss ideas: Nobuya Sakai, Bernard Wegner, Zhiping Wang, Rebecca Sutton, Matthew Klug, Yasser Hassan, Pabitra Nayak, Suhas Mahesh, Sandeep Pathak and Golnaz Sadoughi. I would also like to thank my collaborators in Stanford: Kevin Bush and Tomas Leijtens. I would like to thank Peimei Da for offering me a tasty selection of teas, and to the fresh DPhil students and friends who will be receiving the Snaithling torch: Jonathan Warby, Kelly Schutt, Michael Farrar, Augustin Zaininger, Olivia Ashton, Laura Schade, and Elisabeth Duijnstee. Finally, I would like to specifically thank my colleagues and friends that made life in Oxford memorable, and a time I'll look back on with great fondness: Derek Hollman, Maximilian Hörantner, Konrad Wojciechowski, Alex

Ramadan, Martina Congiu, James Ball, Federico Pulvirenti, Jongchul Lim, Grey Christoforo, Severin Habisreutinger, Nakita Noel, Jacob Wang, Giles Eperon, Guilio Mazzotta and Alba Pellaroque. I would also like to not thank Jay B. Patel.

Contents

1. Introduction 16
1.1. The Sustainability Issue 16
1.2. The Climate Dilemma 18
1.3. Solar Energy 21
1.4. Perovskite solar cells in tandem application 24
1.5. Structure of the thesis 25
2. Theory and Background 28
2.1. Semiconductors 28
2.1.1. Energy Band Theory 28
2.1.2. Semiconductor doping 33
2.1.3. Absorption, generation and recombination 37
2.1.4. Semiconductor junctions and solar cell operation 42
2.1.5. Solar cell characterization 49
2.2. Organic-Inorganic Halide Perovskite Solar cells 55
2.3. Multi-Junction Solar cells 59
3. Experimental Methods 64
3.1. Substrate preparation 64
3.2. Electron transporting layer 64
3.2.1. Solution processed tin-oxide (SnO_2) layer 64
3.2.2. Chemical bath deposition (CVD) tin-oxide (SnO_2) layer 65
3.2.3. Nanoparticles tin oxide (SnO_2) layer 65
3.2.4. Phenyl-C61-butyric acid methyl ester ($PC_{61}BM$) layer 65
3.3. Hole transporting layer 66
3.3.1. Spiro-OMeTAD hole-transporting layer 66
3.3.2. Spiro$(TFSI)_2$ synthesis 66
3.4.3. Phenyl-C61-butyric acid methyl ester ($PC_{61}BM$) layer in multi-junctions 68
3.5.1. $FA_{0.83}Cs_{0.17}Pb(I_{0.8}Br_{0.2})_3$ and $FA_{0.83}Cs_{0.17}Pb(I_{0.6}Br_{0.4})_3$ perovskite 69
3.5.2. $FA_{0.83}Cs_{0.17}Pb(I_{0.3}Br_{0.7})_3$ perovskite with 2% potassium 69
3.5.3. ACN/MA $MAPbI_3$ perovskite 70
3.5.4. ACN/MA $MAPb_{0.75}Sn_{0.25}I_3$ perovskite 71
3.11.1. Overview 74
3.11.2. Inputs for the Optical and Electrical Models 75
3.11.3. $FA_{0.83}Cs_{0.17}Pb(Br_{0.7}I_{0.3})_3$/$MAPbI_3$Tandem Simulation 76
3.11.4. $FA_{0.83}Cs_{0.17}Pb(Br_{0.7}I_{0.3})_3$/$MAPbI_3$ tandem simulation (optimized) 77

3.11.5. $FA_{0.83}Cs_{0.17}Pb(Br_{0.7}I_{0.3})_3/MAPbI_3/MA_{0.4}FA_{0.6}Pb_{0.4}Sn_{0.6}I_3$ triple-junction simulation (optimized) 78

3.13.1. One-dimensional X-ray diffraction 80

3.13.2. Two-dimensional X-ray diffraction 81

3.15.1. Optical pump 81

3.15.2. Derivation of photoconductivity and charge carrier mobility from change in THz electric field transmission 82

4. A formamidinium-cesium mixed-cation lead mixed-halide perovskite for tandem solar cells applications 84

5. Crystallization kinetics and morphology control of formamidinium-cesium mixed-cation lead mixed-halide perovskite via tunability of the colloidal precursor solution 99

6. Fully-Solution Processed All-Perovskite Multi-Junction Solar Cells 114

7. Conclusion and Outlook 134

8. References 137

Table of Figures

Figure 1: Global primary energy consumption from 1800 to 2016 16

Figure 2: Energy use per capita vs gross domestic product (GDP) 17

Figure 3: Greenhouse gas emissions 19

Figure 4: Anomalous global temperature and global CO_2 concentration 20

Figure 5: Global levelized cost of electricity from utility-scale renewable power generation technologies from 2010 to 2017 22

Figure 6: Available energy per year for solar, biomass, wind, hydroelectricity and geothermal energy sources. 23

Figure 7: The parabolic representation of the dispersion curve for a free electron. 29

Figure 8: Energy versus wavevector k for an electron in a monatomic linear lattice of lattice constant a, showing the discontinuity in energy between the first and second Brillouin zone. 30

Figure 9: Schematic of a band structure diagram showing direct (left) and indirect (right) band gap. 32

Figure 10: Schematic illustration of an intrinsic silicon semiconductor with no impurities (left), an n-type silicon semiconductor with boron as impurity dopant (middle), an p-type silicon semiconductor with phosphorous as impurity dopant (right) 34

Figure 11: Schematic illustration of the band diagrams and Fermi energies of intrinsic, p-type and n-type semiconductors 35

Figure 12: Absorption process that leads to the promotion of an electron from the valence band to the conduction band. After excitation, thermalization and recombination processes can take place. 39

Figure 13: Recombination processes in semiconductors 40

Figure 14: Band diagram of a metal to n-type semiconductor interface 44

Figure 15: Band diagram of a metal to p-type semiconductor interface 45

Figure 16: Band diagram of semiconductor-semiconductor junctions 46

Figure 17: Effect of bias on the energy band diagram 49

Figure 18: Solar irradiance terrestrial spectra of (AM1.5 Global and AM1.5 Direct), and the extraterrestrial spectrum (AM 0). 50

Figure 19: The current-voltage curve for photovoltaic device under light (black) and under the dark (red) conditions. The shaded area represents the maximum power attainable from the device under test. 51

Figure 20: One diode equivalent circuit of a solar cell. 54

Figure 25: Generic ABX_3 cubic perovskite unit cell, with commonly used A-site, B-site and X-site ions for solar cell application. 55

Figure 26: Schematic view of the working principle of p-i-n perovskite solar cell. 59

Figure 21: The Shockley-Queisser efficiency limit of an absorber material for various band gaps. 60

Figure 22: Concept of a perovskite/c-Si tandem solar cell 61

Figure 23: Tandem architectures 62

Figure 24: Combined tandem power conversion efficiency for different top cell and bottom cell bandgap combinations 63

Figure 27: Photographs of perovskite films with Br composition increasing from x = 0 to 1 87

Figure 28: X-ray diffraction pattern (XRD) for 2 theta angles from 5 to 60 degree. 89

Figure 29: Lattice Constant of $FA_{0.83}Cs_{0.17}Pb(I_{(1-x)}Br_{(x)})_3$ perovskite system plotted as a function of bromide content. This linear relationship between lattice constant and bromide content indicates that this system follows Vegard's law. 90

Figure 30: Tauc plot of the $FA_{0.83}Cs_{0.17}Pb(I_{0.6}Br_{0.4})_3$ perovskite composition assuming direct band gap and showing determination of optical band gap from intercept. 90

Figure 31: Material characteristics of $FA_{0.83}Cs_{0.17}Pb(I_{0.6}Br_{0.4})_3$ perovskite material. Normalized photoluminescence (PL) measurement measured after 0, 5, 15, 30 and 60 minutes of light exposure 91

Figure 32: Photoluminescence spectra of $FA_{0.83}Cs_{0.17}Pb(I_{0.6}Br_{0.4})_3$ following excitation with pulse fluence of 0.5 µJcm-2 and laser intensity of 5 Wcm-2 at a wavelength of 405 nm. The high intensity photoluminescence stability was measured by Waqaas Rehman of the Department of Physics, University of Oxford. 92

Figure 33: Mixed-halide perovskite films heated on a 130 ° C hotplate inside a N_2 glovebox (~ 4ppm O_2 and ~ 0.5ppm H_2O) for a period of up to 6 hours 95

Figure 34: Device architecture and I-V characteristics for $FA_{0.83}Cs_{0.17}Pb(I_{0.6}Br_{0.4})_3$ perovskite and Si PV cells 96

Figure 35: Impact of colloids in the precursor solution on the nucleation stage of the $FA_{0.83}Cs_{0.17}Pb(Br_{0.2}I_{0.8})_3$ perovskite system 103

Figure 36: Scanning electron microscopy (SEM) image of the top view of an un-annealed $FA_{0.83}Cs_{0.17}Pb(Br_{0.2}I_{0.8})_3$ as cast thin film, prepared with an acid-free perovskite precursor solution. 104

Figure 37: Impact of mixing colloidal solutions with colloid-free solution on the nucleation stage of the $FA_{0.83}Cs_{0.17}Pb(Br_{0.2}I_{0.8})_3$ perovskite system 104

Figure 38: Growth kinetics of the $FA_{0.83}Cs_{0.17}Pb(Br_{0.2}I_{0.8})_3$ perovskite system with various colloid concentrations. Microscope images using a 50× magnification of post-nucleation thin films heated at 220°C in an air atmosphere; prepared using precursor solutions aged with an acid for a period of time 106

Figure 39: Impact of colloids in the precursor solution on morphology and crystal quality 109

Figure 40: Optoelectronic and crystal properties for $FA_{0.83}Cs_{0.17}Pb(Br_{0.2}I_{0.8})_3$ perovskite prepared with various aging conditions 110

Figure 41: Impact of precursor solution aging time on solar cell device performance 112

Figure 42: Optical characterization of $FA_{0.83}Cs_{0.17}Pb(Br_{0.7}I_{0.3})_3$ perovskite material with 2% potassium additive and current-voltage characteristic of a SnO_2/PCBM/$FA_{0.83}Cs_{0.17}Pb(Br_{0.7}I_{0.3})_3$/Spiro-OMeTAD perovskite solar cell with 2% mol. potassium (K^+) additive 118

Figure 43: Two-terminal (2T) $FA_{0.83}Cs_{0.17}Pb(Br_{0.7}I_{0.3})_3$/$MAPbI_3$ tandem perovskite solar cells 121

Figure 44: Measured solar simulator spectrum compared to the AM1.5G spectrum 123

Figure 45: Impact of varying the composition of A to B-site cations for ACN processed $MAPb_{0.75}Sn_{0.25}I_3$ perovskite materials 124

Figure 46: Impact of varying the composition of A to B-site cations of the ACN/MA $MAPb_{0.75}Sn_{0.25}I_3$ single junction perovskite system 125

Figure 47: $FA_{0.83}Cs_{0.17}Pb(Br_{0.7}I_{0.3})_3$/$MAPbI_3$/$MAPb_{0.75}Sn_{0.25}I_3$ triple-junction perovskite solar cells. 127

Figure 48: Architecture and device characterization of a $FA_{0.83}Cs_{0.17}Pb_{0.5}Sn_{0.5}I_3$ filtered with a $FA_{0.83}Cs_{0.17}Pb(Br_{0.7}I_{0.3})_3$/$MAPbI_3$ dual-junction solar cells 129

Figure 49: Optical properties of the recombination interlayer and hole and electron accepting layers. 130

Figure 50: Optical and electrical modelling of multi-junction perovskite solar cells 132

PEER-REVIEWED PUBLISHED PUBLICATIONS

[1] Y. Hou, X. Du, S. Scheiner, **D. P. McMeekin**, Z. Wang, N. Li, M. S. Killian, H. Chen, M. Richter, I. Levchuk, N. Schrenker, E. Spiecker, T. Stubhan, N. A. Luechinger, A. Hirsch, P. Schmuki, H.-P. Steinrück, R. H. Fink, M. Halik, H. J. Snaith, and C. J. Brabec, "A generic interface to reduce the efficiency-stability-cost gap of perovskite solar cells.," ***Science***, vol. 358, no. 6367, pp. 1192–1197, Nov. 2017.

[2] N. K. Noel, M. Congiu, A. J. Ramadan, S. Fearn, **D. P. McMeekin**, J. B. Patel, M. B. Johnston, B. Wenger, and H. J. Snaith, "Unveiling the Influence of pH on the Crystallization of Hybrid Perovskites, Delivering Low Voltage Loss Photovoltaics," ***Joule***, vol. 1, no. 2, pp. 328–343, Oct. 2017.

[3] **D. P. McMeekin**, Z. Wang, W. Rehman, F. Pulvirenti, J. B. Patel, N. K. Noel, M. B. Johnston, S. R. Marder, L. M. Herz, and H. J. Snaith, "Crystallization Kinetics and Morphology Control of Formamidinium-Cesium Mixed-Cation Lead Mixed-Halide Perovskite via Tunability of the Colloidal Precursor Solution," ***Adv. Mater.***, p. 1607039, May **2017**.

[4] N. Sakai, Z. Wang, V. M. Burlakov, J. Lim, **D. McMeekin**, S. Pathak, and H. J. Snaith, "Controlling Nucleation and Growth of Metal Halide Perovskite Thin Films for High-Efficiency Perovskite Solar Cells," ***Small***, vol. 13, no. 14, p. 1602808, Apr. **2017**.

[5] K. A. Bush, A. F. Palmstrom, Z. J. Yu, M. Boccard, R. Cheacharoen, J. P. Mailoa, **D. P. McMeekin**, R. L. Z. Hoye, C. D. Bailie, T. Leijtens, I. M. Peters, M. C. Minichetti, N. Rolston, R. Prasanna, S. Sofia, D. Harwood, W. Ma, F. Moghadam, H. J. Snaith, T. Buonassisi, Z. C. Holman, S. F. Bent, and M. D. McGehee, "23.6%-efficient monolithic perovskite/silicon tandem solar cells with improved stability," ***Nat. Energy***, vol. 2, no. 4, p. 17009, Feb. **2017**.

[6] Z. Wang, **D. P. McMeekin**, N. Sakai, S. van Reenen, K. Wojciechowski, J. B. Patel, M. B. Johnston, and H. J. Snaith, "Efficient and Air-Stable Mixed-Cation Lead Mixed-Halide Perovskite Solar Cells with n-Doped Organic Electron Extraction Layers," ***Adv. Mater.***, vol. 29, no. 5, p. 1604186, Feb. **2017**.

[7] W. Rehman, **D. P. McMeekin**, J. B. Patel, R. L. Milot, M. B. Johnston, H. J. Snaith, and L. M. Herz, "Photovoltaic mixed-cation lead mixed-halide perovskites: links between crystallinity, photo-stability and electronic properties," ***Energy Environ. Sci.***, vol. 10, no. 1, pp. 361–369, Jan. **2017**.

[8] G. E. Eperon, T. Leijtens, K. A. Bush, R. Prasanna, T. Green, J. T.-W. Wang, **D. P. McMeekin**, G. Volonakis, R. L. Milot, R. May, A. Palmstrom, D. J. Slotcavage, R. A. Belisle, J. B. Patel, E. S. Parrott, R. J. Sutton, W. Ma, F. Moghadam, B. Conings, A. Babayigit, H.-G. Boyen, S. Bent, F. Giustino, L. M. Herz, M. B. Johnston, M. D. McGehee, and H. J. Snaith, "Perovskite-perovskite tandem photovoltaics with optimized bandgaps," ***Science***, **2016**.

[9] S. N. Habisreutinger, **D. P. McMeekin**, H. J. Snaith, and R. J. Nicholas, "Research Update: Strategies for improving the stability of perovskite solar cells," ***APL Mater.***, vol. 4, no. 9, p. 91503, Sep. **2016**.

[10] M. T. Horantner, P. K. Nayak, S. Mukhopadhyay, K. Wojciechowski, C. Beck, **D. McMeekin**, B.

Kamino, G. E. Eperon, and H. J. Snaith, “Shunt-Blocking Layers for Semitransparent Perovskite Solar Cells,” ***Adv. Mater. Interfaces***, vol. 3, no. 10, p. 1500837, May **2016**.

[11] **D. P. McMeekin**, G. Sadoughi, W. Rehman, G. E. Eperon, M. Saliba, M. T. Hörantner, A. Haghighirad, N. Sakai, L. Korte, B. Rech, M. B. Johnston, L. M. Herz, and H. J. Snaith, “A mixed-cation lead mixed-halide perovskite absorber for tandem solar cells.,” ***Science***, vol. 351, no. 6269, pp. 151–5, Jan. **2016**.

[12] Y. Zhang, M. Liu, G. E. Eperon, T. C. Leijtens, **D. McMeekin**, M. Saliba, W. Zhang, M. de Bastiani, A. Petrozza, L. M. Herz, M. B. Johnston, H. Lin, and H. J. Snaith, “Charge selective contacts, mobile ions and anomalous hysteresis in organic–inorganic perovskite solar cells,” ***Mater. Horiz.***, vol. 2, pp. 315–322, **2015**.

MANUSCRIPTS IN PREPARATION

[#]These authors contributed equally to this work.

[1] **David P. McMeekin**, *Suhas Mahesh, Nakita K. Noel, Matthew T. Klug, JongChul Lim, James M. Ball, Laura Herz, Michael B. Johnston, and Henry J. Snaith*, "Fully-Solution Processed All-Perovskite Multi-Junction Solar Cells", *(Submitted).*

[2] Zhiping Wang,[#] **David P. McMeekin**,[#] Joseph J. Berry, Laura T Schelhas, Nicholas Hawkins, Fritz Vollrath, Henry J. Snaith, "Effects of crystallinity of perovskite films on photovoltaic long-term stability", *(In preparation).*

Oral Presentations

[1] A mixed-cation lead mixed-halide perovskite system for tandem applications, ***Supersolar Technical Meeting 2016,*** Winchester, UK

[2] Crystallization Kinetics and Morphology Control of Formamidinium-Cesium Mixed-Cation Lead Mixed-Halide Perovskite via Tunability of the Colloidal Precursor Solution, ***Hybrid and Organic Photovoltaics (HOPV17),*** Lausanne, Switzerland

[3] Crystallization Kinetics and Morphology Control of Formamidinium-Cesium Mixed-Cation Lead Mixed-Halide Perovskite via Tunability of the Colloidal Precursor Solution, Asian-Pacific ***Hybrid and Organic Photovoltaics (AP-HOPV18),*** Kitakyushu, Japan

1. Introduction

1.1. The Sustainability Issue

The intensification of global demand for natural resources has placed an enormous strain on the environmental and ecological systems we rely on to sustain human life on planet Earth. In the past few centuries, we have undergone significant changes in our economies, where agrarian societies have transitioned to industrial societies. This has had a profound impact on the types of resources we consume to meet our ever-growing energy needs. We shifted from renewable energies such as wind, hydro and biomass as main sources of heat and fuel to non-renewable fossil fuels. Figure 1 illustrates this transition that occurred over the past 200 years- from renewable sources to energy sources with higher energetic densities such as oil, coal and natural gas.

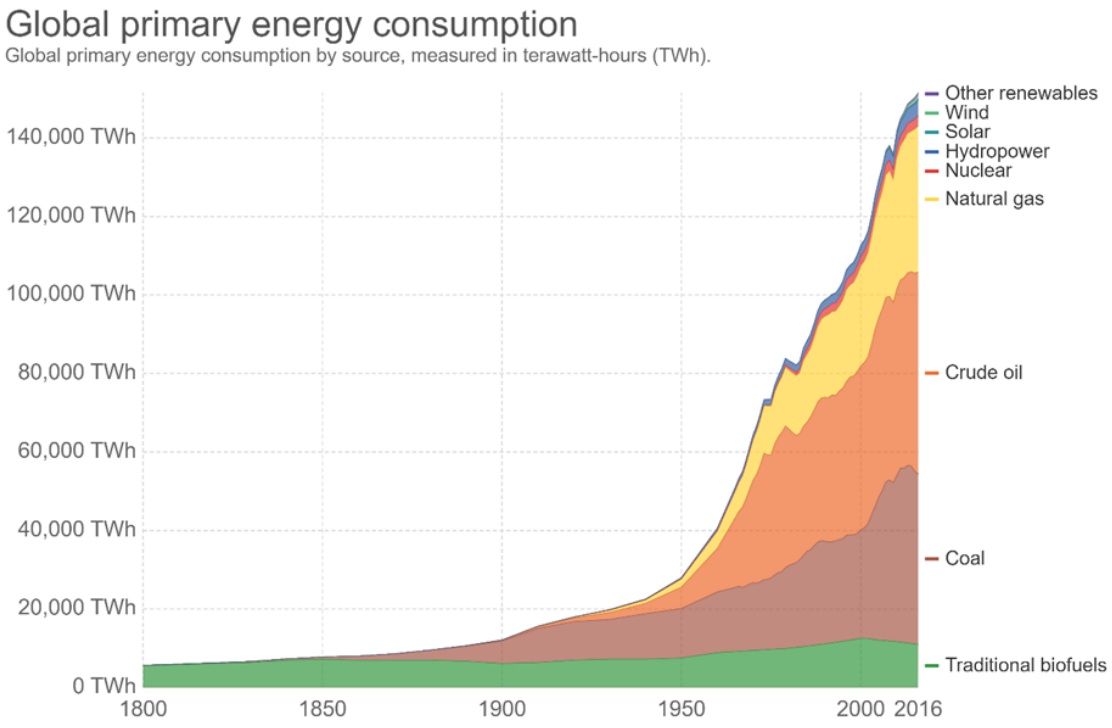


Figure 1: Global primary energy consumption from 1800 to 2016 (Copyright – Hannah Ritchie and Max Roser. Published online at OurWorldInData.org. Source: Vaclav Smil 2017)[1]

This access to abundant, inexpensive and portable sources of energy has driven our global economies to new heights, while simultaneously creating a profound addiction to depletable resources. Energy has become a driving force for economic growth and human prosperity. Through technological advancements and an increase in reliable access to a source of energy, societies have been able to free-up time spent on household chores, to instead focus their efforts on improving their health, education and productivity.[1] In turn, although not necessarily causal in nature, an increase in energy consumption correlates with an increase in gross domestic product (GDP), as shown in Figure 2. Economic growth, measured using GDP, has become a single metric to quantify a society's living standard and prosperity. Although quantifying the prosperity of a society with a single GDP value may be deeply flawed and an oversimplification of a complex system, economists, statisticians and politicians still rely heavily on this value. Nevertheless, it is apparent that modern day economies have become increasingly dependent on access to reliable, cheap and abundant energy sources to sustain their GDP growth.

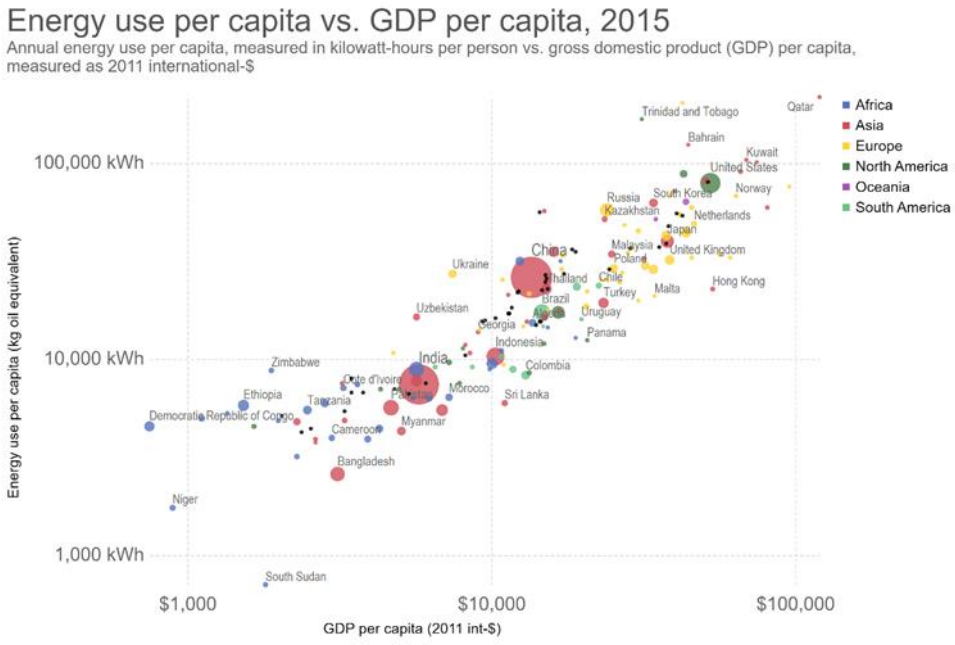


Figure 2: Energy use per capita vs gross domestic product (GDP) *(Copyright – Hannah Ritchie and Max Roser. Published online at OurWorldInData.org. Source: Vaclav Smil 2017)*[1]

Considering this strong relationship between energy consumption and GDP, it is safe to assume that energetic commodities will remain a vital part of our economies for years to come. Some highly industrialised countries have started to taper the energy intensity of their economy (i.e.

quantity of energy needed to produce one unit of GDP growth).[1,2] However, fast growing economies such as BRIC (Brazil, Russia, India, and China), combined with the increase in world population, require immediate action in order to provide the sustainable sources of energy necessary to maintain this level of worldwide prosperity growth.

1.2. The Climate Dilemma

As discussed in Section 1.1, access to energy is a fundamental element for stimulating and supporting economies to improve prosperity and human well-being. The world economy now consumes over 140 000 TW, and this number is expected to increase.[1] However, this energy is primarily produced by non-renewable fossil-fuels that emit carbon dioxide (CO_2), a common heat trapping greenhouse gas. During the combustion process of hydrocarbons, a chemical reaction with oxygen (O_2) occurs, which releases CO_2, water (H_2O), and heat (Figure 3).[3]

$$C_xH_y + N(O_2) \leftrightarrow x(CO_2) + 0.5y + H_2O \quad (1)$$

Where, x refers to the number of carbon (C) atoms, y refers to the number of hydrogen (H) atoms, and N refers to the number of Oxygen (O) atoms required.

This reaction is highly exothermic, where the energy required to break the chemical bond of the hydrocarbon is less than the energy releases in formation of CO_2 and H_2O. Octane (n-C_8H_{18}), a hydrocarbon and an alkane used to produce gasoline, has enthalpy change (Δ) of -5460 KJ mol^{-1} when it undergoes a complete combustion,[4] resulting in an energy density of 44.8 KJ/g , which is roughly 2 to 3 times higher than dry wood (16-19 KJ/g). However, as equation 1 describes, this energy can only be released with the creation of CO_2. Other types of gases such as methane (CH_4), nitrous oxide (N_2O), ozone (O_3) and other fluorinated gases also contribute to the heat trapping effect. However, CO_2 produced from burning fossil fuels to generate energy remains the largest contributor of greenhouse gases (Figure 3).

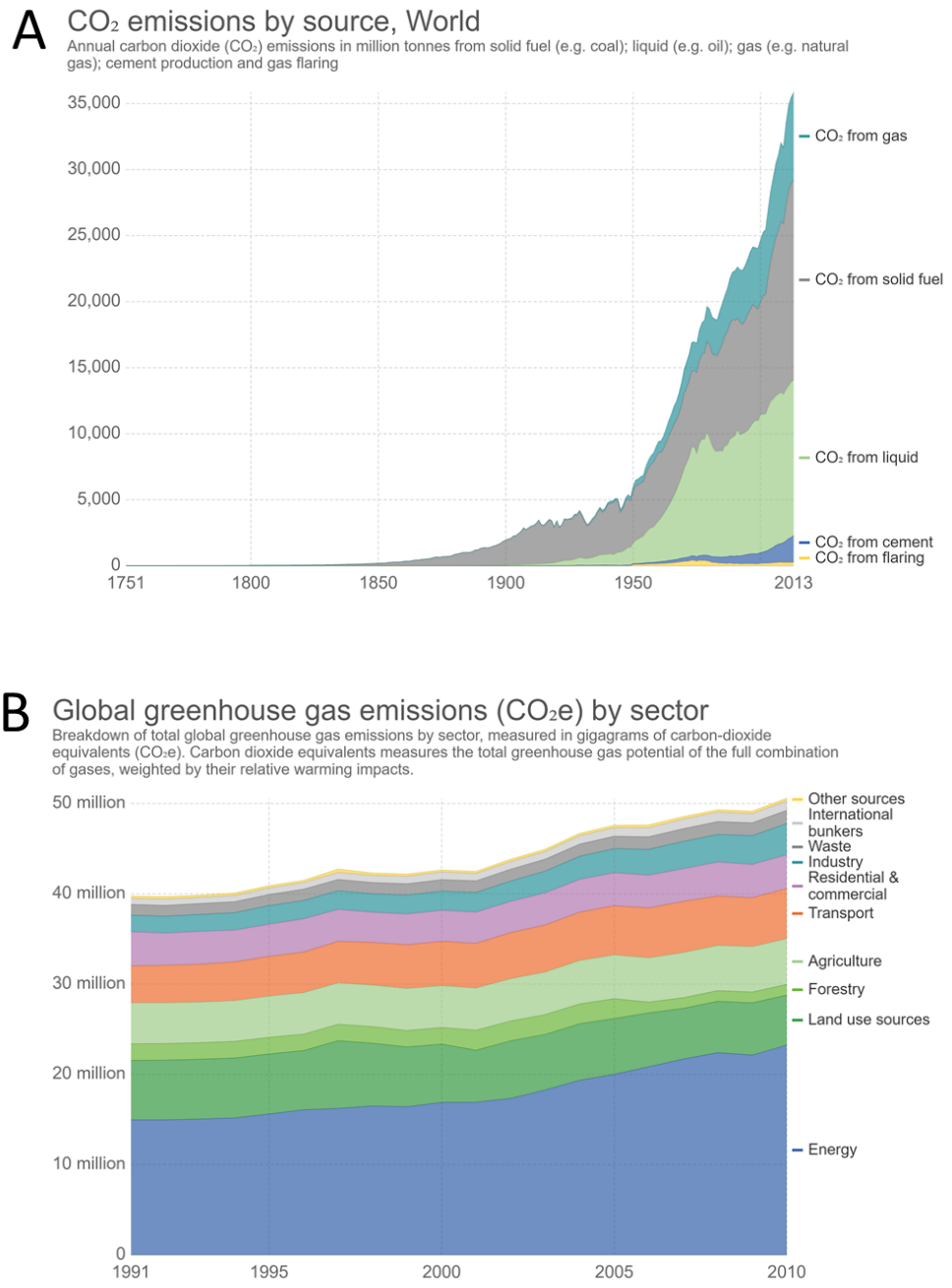


Figure 3: Greenhouse gas emissions. *A) CO2 emission by source B) Global greenhouse gas emission by sector (Copyright – Hannah Ritchie and Max Roser. Published online at OurWorldInData.org. Source: A) CDIAC B) UN Food and Agricultural Organization)*[1]

Greenhouse gases are essential to animal and plant life on planet Earth. Their property to absorb infrared light (IR), allow them to capture heat, without which the earth's surface temperature would plummet from the current 14 °C to approximately −21 °C.[5,6] Furthermore, CO_2 is indispensable to the process of photosynthesis, where light converts carbon dioxide and water into sugar and

oxygen. Nevertheless, if the concentration of greenhouse gases in the atmosphere increases, this can have disastrous consequences for our fragile planetary ecosystem. This is the case for Venus, which is the hottest planet in the Solar System despite being further away from the Sun than Mercury. This is due to a runaway greenhouse effect, which causes surface temperatures to reach over 400 °C.[7] As shown in Figure 4, the average global temperature has risen by a full degree Celsius over the last century, along with the increase of global CO_2 concentrations in the atmosphere.

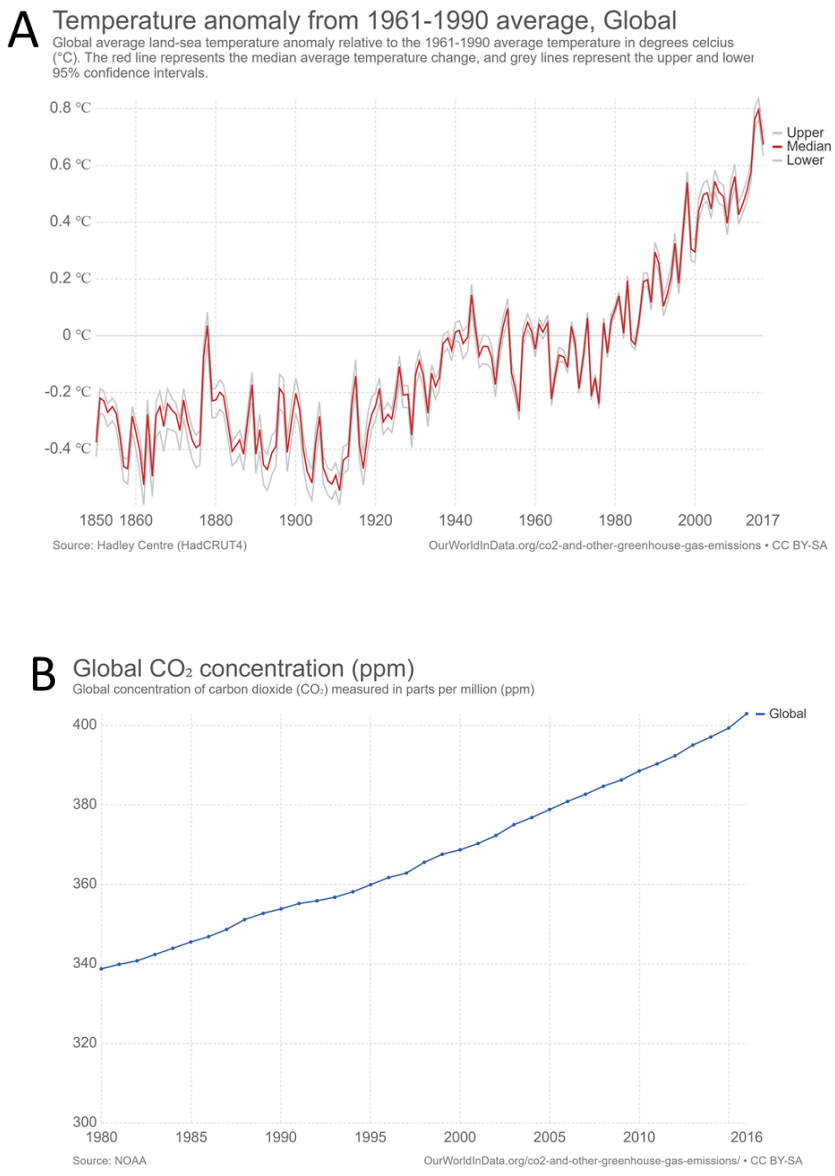


Figure 4: Anomalous global temperature and global CO_2 concentration. *A) Global average temperature measured from 1850 to 2017 B) Global CO_2 concentration measured in parts per million (ppm) (Copyright – Hannah Ritchie and Max Roser. Published online at OurWorldInData.org. Source: A) Hadley Center B) NOAA)*[1]

This small but not insignificant temperature rise may not be noticeable in our everyday lives. However, these changes significantly impact weather patterns, heat waves and drought will become more frequent, while other parts of the world may have to endure more intense floods and hurricanes. The loss of biodiversity is also a major concern, where fragile ecosystems may not be able to adapt to this quick change in climate. The impact of an increase in ocean temperatures can directly be observed on the health of coral life in the Great Barrier Reef. Coral bleaching occurs when stressful environmental conditions, usually caused by heatwaves during El Niño years, result in the expulsion of the algal partner from the coral. As Terry P. Hughes et al. explains, the proportion of reefs experiencing extreme bleaching, defined by > 60% of corals bleached, is 4 times higher in 2016 than in 1998 or 2002.[8,9] According to Preston, Jones et al, a temperature rise between 2 and 3 °C would result in 97% of the Great Barrier Reef being bleached every year.[10] The disappearance of coral life is only one of many stark effects of global warming that humanity will have to endure, if no global political action is undertaken to address climate change. The effects of climate change will not only impact the environment, but will also cause future humanitarians crises. The changing weather patterns and the increase in frequency of extreme weather events will likely increase the number of displacement of people and refugees.[11] Furthermore, armed conflicts may increase due to scarcity of vital resource, such as water, in various regions of the world.[11]

1.3. Solar Energy

An energy revolution will need to take place to sustain life on Earth. Transition from an exhaustible fossil fuel energy era to renewable sources with low CO_2 will inevitably happen. Hence, the question is not whether humanity will shift to renewable energies, but rather when. It is imperative that this change happens sooner rather than later, to mitigate the impacts of global warming. For established and emerging markets to shift their energy policy to renewables, economics incentives must present. Although government subsidies can provide temporary support to emerging renewable technologies, only those which are economically advantageous will prevail in the end. Technologies that can compete with coal on a levelized cost of electricity (LCOE) basis, are true potential alternatives to fossil fuels. LCOE is a measurement of lifetime building and operation costs divided by the energy production over its assumed lifetime. According to the international renewable energy agency (IRENA), biomass, geothermal, hydro and onshore wind have been able to offer power at a rate well under 100 USD/MWh since 2010, competing with fossil fuels that are ranging from 50

to 160 USD/MWh.[12] Due to sharp decline in manufacturing costs of monocrystalline and polycrystalline silicon solar panels, solar power is now able to offer competitive LCOE.

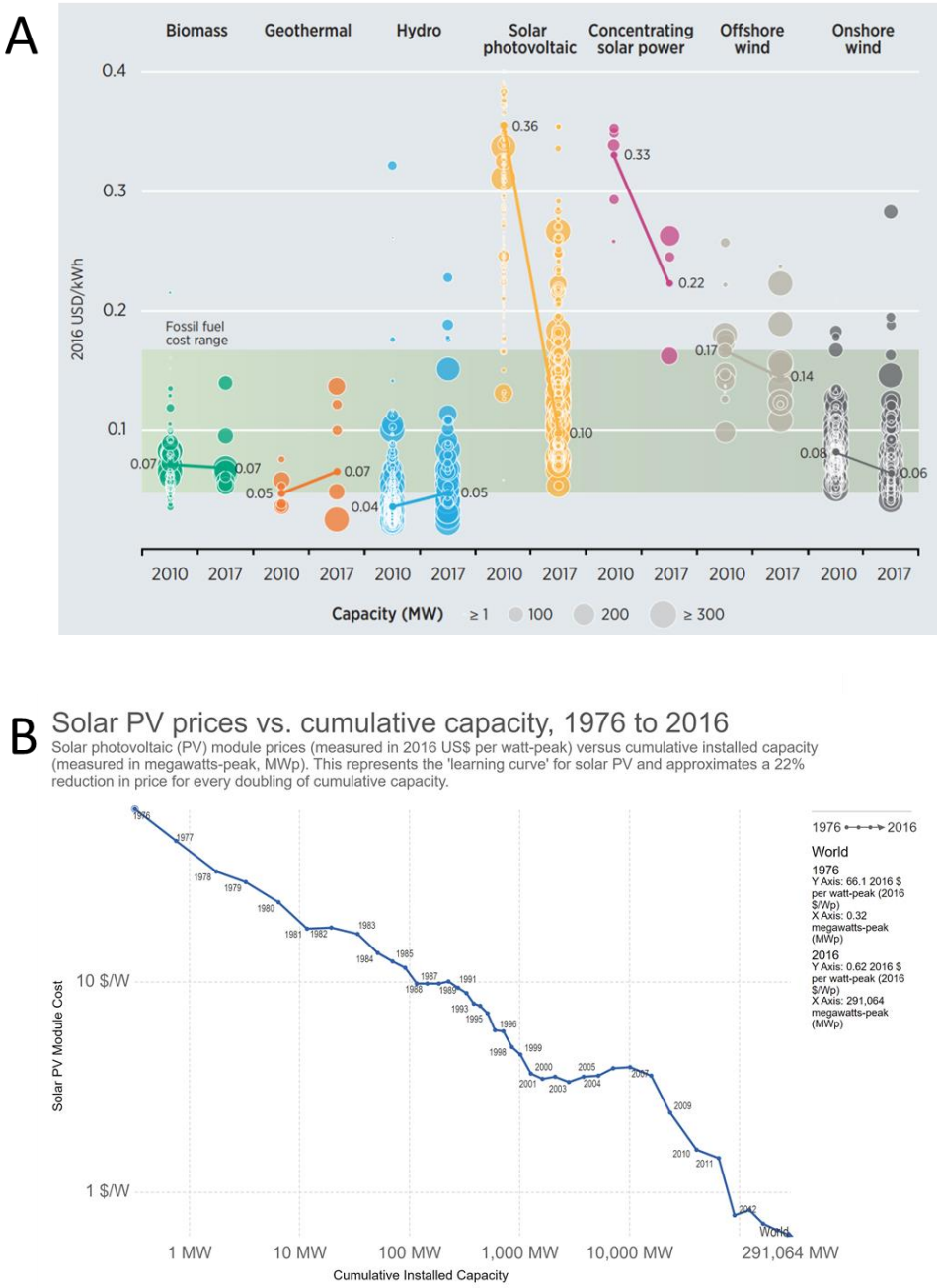


Figure 5: Global levelized cost of electricity from utility-scale renewable power generation technologies from 2010 to 2017. (Copyright – international renewable energy agency (IRENA). Published online at www.irena.org.[12]

Although solar energy is not yet the cheapest form of renewable energy, it is the technology which is dropping cost at the fastest pace. This price drop is driven by technological improvements such as passivated emitter and rear cell (PERC) and diamond wire saws, but also the increase in cumulative capacity and in fierce competition. The price has fallen more than 100-fold since 1976, and will continue to fall at an estimated 22% for every doubling in capacity.[1] Furthermore, compared to other renewable technologies, solar power has a practically inexhaustible amount of available resource at its disposal. The sunlight hitting the earth's surface provides 3 orders of magnitude more energy per year than all the other forms of renewable energy combined.

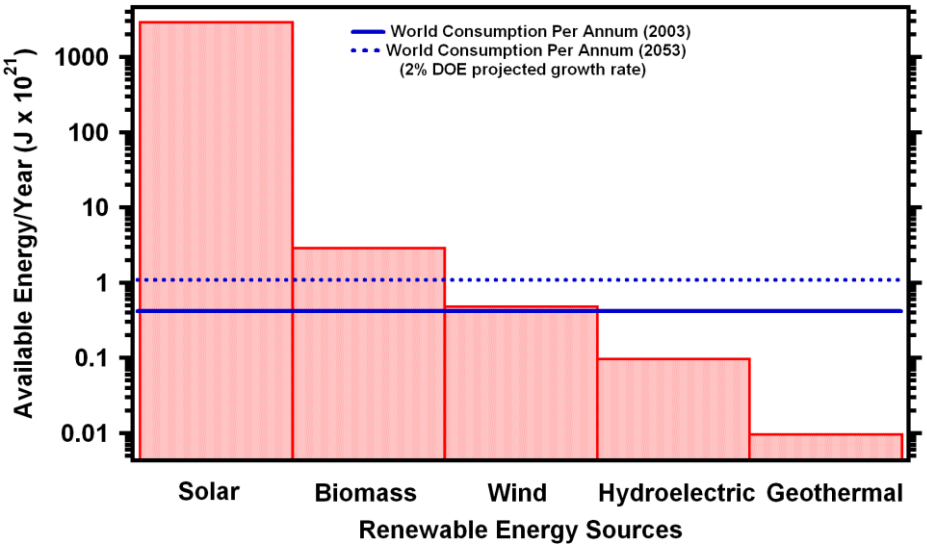


Figure 6: Available energy per year for solar, biomass, wind, hydroelectricity and geothermal energy sources*. (Copyright – S. E. Manahan. CRC Press).*[13]

This limitless amount of available energy suggests that solar prices can remain low as demand rises. This is not necessarily the case for fossil fuels, where the price will eventually rise significantly as scarcity of resources come into play. Using quick "back of the envelope calculation", assuming the Sun shines 120 000 TW of radiation on the surface of the Earth, we can estimate that covering 0.1% of the land on Earth with 17% efficient solar cells would produce more than 20 TW of power, which exceeds today's entire world energy consumption. However, the energy solution of the future will rely on a mixture of renewable energies to average out the photovoltaic performance during sunny and overcast days. Furthermore, energy storage will also need to become increasingly cost effective to cope with daily peak demands.

1.4. Perovskite solar cells in tandem application

To date, silicon-based photovoltaics have dominated the solar market, reaching up to 93% of the market share.[14] Although alternative thin film materials for solar cell application have been studied since the 1970s,[15] specifically, copper indium gallium selenide (CIGS), copper zinc tin sulfide (CZTS), cadmium sulfide/cadmium telluride (CdS/CdTe), dye sensitized solar cell (DSSC) and organic photovoltaics (OPV), they have yet to gain a substantial share of the solar market. Silicon is an abundant, non-toxic and stable material, with a 1.11 eV band gap at 300K and a long charge-carrier lifetime.[16] This combination of properties has provided incentive to investigate this material for solar cell applications. Nevertheless, it is only recently that c-Si and polycrystalline silicon solar cells are manufactured at competitive prices. In turn, motivation to find alternative material to silicon has diminished due to recent affordability of silicon solar cells. However, opportunities still exist for technologies that promise either substantial manufacturing cost reduction or higher PCEs. Another approach is to integrate emerging technologies with silicon-based solar cells to improve its performance, and thus considerably lower its LCOE. This integration between two solar technologies can be realized by creating a tandem architecture with c-Si.

A novel and ambitious thin-film photovoltaic technology has recently been pioneered.[17,18] The first discovery of the organic-inorganic perovskite material dates back to 1994, by a researcher at IBM, David Mitzi.[19–21] Mitzi and co-workers demonstrated that layered organic- inorganic perovskites-based materials could be used in light-emitting diodes (LED) applications. However, it was only a decade later that $CH_3NH_3PbI_3$ ($MAPbI_3$) material was introduced in a solar cell application. Miyasaka and co-workers first showed in 2009 that organic-inorganic perovskite used as light absorbing material was reaching 3.8% PCE, however at that point, it was believed that perovskite was acting as a dye-sensitizer.[17] It is only in 2012 that efficiencies crossed the 9%[22] and 10%[18] PCE mark, but more importantly, Snaith and co-workers showed that perovskite was acting as a semiconductor rather than a sensitizer. They found that it was possible to replace the mesoporous n-type TiO_2 with an insulating Al_2O_3 scaffold, hence electron travel through the perovskite and not via a traditional sensitized process. This understanding gave rise to the fabrication of fully planar perovskite heterojunctions, where the complete removal of the mesoporous scaffold could be realized and simple p-i-n architectures could provide highly efficient devices.[23] This evolution from dye-sensitized solar cells (DSSC) to perovskite solar cells has been one of the major breakthroughs in thin-film solar cell technology in the past decade.

Considering that complete silicon-based modules are now efficient, stable and manufactured from an abundant source of material, it becomes increasingly difficult to justify the complete replacement of this technology. Instead, we can aim to integrate an emerging technology with the already established silicon technology to improve its efficiency. Perovskite materials, with the ABX_3 structure, have the ability to tune their band gap by adjusting the chemical composition. In turn, this property allows perovskite solar cells to be used in tandem architecture with silicon solar cells. Hence, when used in a tandem architecture with silicon, perovskite solar cells can move beyond the Shockley–Queisser limit and hence potentially significantly reduce the LCOE of a silicon-based solar cell. Furthermore, by reducing thermalization losses of photons, an all-perovskite tandem architecture which significantly surpasses the performance of the silicon solar cell, has the possibility to be commercially viable.

1.5. Structure of the thesis

This thesis focuses on the development of perovskite in tandem architecture applications. The tandem configuration allows the reduction of photon thermalization losses, and hence movement beyond the Shockley-Queisser[24] and the Tiedje- Yablonovitch limit.[25] In this work, we discuss the many hurdles that were surpassed in order to integrate perovskite materials in tandem architectures with crystalline silicon and with other perovskites to create a fully-solution processed all-perovskite multi-junction solar cell.

The first chapter provides an introduction to the topic and presents the broader context to the general reader. We highlight the motivations behind pursuing solar power technology as an alternative to fossil fuels. We clearly state and discuss the economic and environmental advantages and incentives to shifting our energy production towards low carbon emission and renewable energy sources.

We then proceed to discuss the background and theory that make tandem perovskite photovoltaics possible. This includes a very broad range of concepts revolving around solid state physics and semiconductors, crystallography, energy band theory and recombination mechanisms observed in photovoltaics. However, we also discuss more applied notions focused around the general working principles of solar cells and the methods and characterization tools needed to improve the many aspects of photovoltaics.

Chapter 3 describes the materials and methods used throughout this thesis. This will detail the solar cell fabrication along with synthesis for various materials. The equipment and characterization techniques are also detailed in full.

In chapter 4 we thoroughly explain the problems which have delayed and limited the use of perovskite materials in tandem applications. Prior to this work, efficient perovskite solar cells have been prepared using materials with a band gap of approximately 1.6 eV. However, the ideal band gap energy for tandem application with silicon solar cells is around 1.7 to 1.8 eV. This ideal band gap energy should be achievable by simply tuning the halide composition. Yet in previous attempts to do this, a critical issue arose, whereby materials with mixed halides tend to suffer from halide segregation resulting in the electronic band gap dropping to that of the $MAPbI_3$ materials (1.57 eV), negating any benefit of tuning the band gap.[26] Additional problems of phase instabilities, increased electronic disorder and much lower charge carrier mobilities have also been observed for perovskites with the 1.7 to 1.8 eV band gap, suggesting that perovskites may ultimately fail to reach the ideal performance in tandems, if we must solely rely on the lower band gap materials.

We resolve many of these issues by designing a stable and efficient wide-band (1.74 eV) gap perovskite material. This mixed-cation lead mixed halide is comprised of formamidinium-cesium lead bromide iodide $FA_{(1-x)}Cs_xPb(I_{(1-y)}Br_y)_3$ perovskite material. By tuning the A-site cation, and partially substituting the organic FA^+ cation with an inorganic Cs^+ cation, we are able to stabilize the perovskite structure throughout the iodide to bromide compositional range. This novel perovskite material can be fabricated with a high degree of crystallinity and texturing. In turn, this material shows surprisingly low level of energetic disorder, comparable to neat halide perovskite system. Removing the highly volatile methylammonium (MA^+) cation from the perovskite structure, and replacing it with an inorganic cation with a lower volatility, substantially improved the thermal stability of the material. This combination of properties allowed for the fabrication of efficient and stable perovskite/c-Si tandem solar cells.

In chapter 5, we investigate the role of the solution in the crystallization kinetics and the control of morphology of the perovskite film. We observed that identical precursor salt compositions can be prepared in solution, however, not all films display the same crystal quality, morphology and optoelectronic properties. By studying the solution, we found that perovskite precursor solutions can display a strong Tyndall effect. We attribute this light scattering effect to undissolved lead polyhalide colloids present in the precursor solution, namely, $[PbX_3]^{1-}$, $[PbX_4]^{2-}$, $[PbX_5]^{3-}$, $[PbX_6]^{4-}$. We characterized the hydrodynamic size of these colloids using a dynamic light scattering (DLS) measurement. We suggest that these colloids act as seeds and serve as nucleation sites, and thus impact the

crystallization kinetics and film morphology of the perovskite film. We show that the colloid concentration can be tuned using hydrohalic acid additive to the precursor solution. Hydrobromic (HBr) an hydroiodic acids (HI) are employed to slowly dissolve the colloids, and thus obtain "full solutions" which do not display strong Tyndal effects. Through these processing methods, we can vary the grain size from hundreds of nanometers to tens of microns. In turn, we measured a significant reduction in microstrain and a two-fold increase in charge-carrier mobilities between films prepared with and without acidic additives. Obtaining high quality $FA_{(1-x)}Cs_xPb(I_{(1-y)}Br_y)_3$ perovskite film with pinhole free morphology enabled both improved stability and efficiency.

We then proceeded to integrate this $FA_{(1-x)}Cs_xPb(I_{(1-y)}Br_y)_3$ into a fully-solution processed all-perovskite multi-junction solar cell, detailed in chapter 6. Fabricating an all-solution processed tandem solar cell opens new avenues for large-scale depositions techniques, namely roll-to-roll (R2R), blade blading, or inkjet printing. We show that using a ACN/MA solvent composite with a low viscosity and boiling point can sequentially process perovskite layers on top of one another, thus forming all-solution processed multi-junctions. The combination of large-scale processing with the theoretically high efficiencies of tandem and multi-junction solar cells has the potential to transform the energy industry as we know it.

Finally, chapter 7 presents the conclusions and summarizes work undertaken in this thesis to achieve a stable and high performing perovskite material for tandem applications. We provide an outlook on the future of perovskite solar cells and their feasibility in tandem applications. We discuss the necessary path and challenges ahead to make this novel perovskite material commercially viable.

2. Theory and Background

This chapter provides a condensed introduction and overview into the fundamental concepts of semiconductor physics in photovoltaic devices. These notions are largely based on "The Physics of Solar Cells" by Jenny Nelson[27], "Physics of solar cells: from basic principles to advanced concepts" Würfel, [28] and "Introduction to Solid State Physics" by Charles Kittel.[29]

2.1. Semiconductors

Semiconductor physics is at the heart of the operating principles of numerous electronic devices, including, transistors, lasers, detectors, and solar cells. A metal is a material or compound which typically exhibits good conductivity, typically in the range of 10^{-6} to 10^{-8} Ωm, while insulators do not transfer electrons efficiently.[30] Electrical conductivity is possible due to electrons that are not bound to atoms, but rather move freely in the crystal. Semiconductors usually have conductivities in-between a metal and an insulator. They can alter their electrical properties by either applying an external electric field, or by introduction of impurities into the crystal structure called doping. This simple but extraordinary property allows semiconductors to create devices that are used for amplification, switching, and energy conversion. These devices propelled the world into a new era: the silicon age.

2.1.1. Energy Band Theory

To properly understand semiconductors, we first need to briefly introduce and explore the theory of quantum mechanics, however, an in-depth study of this quantum physics is beyond the scope of this thesis. In quantum physics, as oppose to classical physics, objects display characteristics of both particles and waves. This concept is referred to as wave-particle duality. Quantum objects can collide with one another and exchange kinetic energy, thus behaving as particles, while simultaneously displaying constructive and destructive interference, thus displaying wave-like properties. Electrons

and photons are elementary particles that exhibit this wave–particle duality. We first present a free-electron model, where there is no periodic potential applied. In this case, the energy is quadratically dependent on k, as describes in equation (2) and plotted in

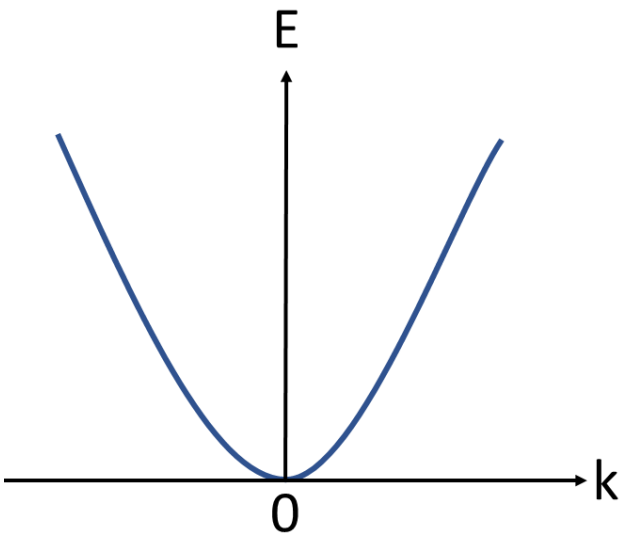


Figure **7:**

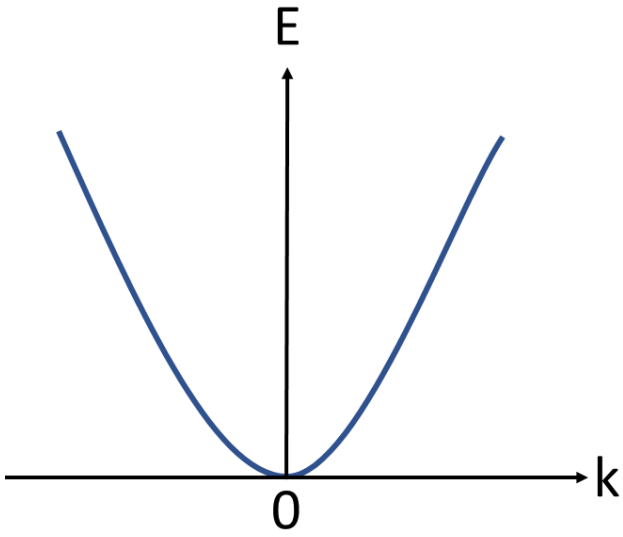


Figure 7: The parabolic representation of the dispersion curve for a free electron.

$$E(k) = \frac{p^2}{2m_0} = \frac{\hbar^2 k^2}{2m_0} \qquad (2)$$

Where E is the energy of the particle, p is the momentum of the particle, k is a wave vector of the particle, $\hbar = \frac{h}{2\pi}$ is the reduced plank constant, m_0 is the mass of the particle.

However, an electron in a crystalline solid behaves differently, due to the periodic potential found in the lattice. Electron waves are reflected at the Brillouin zone boundary from the ion cores. An electron within a periodic crystal can be described with a wave function ψ, by solving the general time-independent Schrödinger equation:

$$\hat{H}|\Psi\rangle = E|\Psi\rangle \tag{3}$$

Where, $\hat{H}$ is the Hamiltonian operator that describes the total energy of the system particle, and E is the energy eigenvalue.

This leads us to Bloch wave function which is obtained by solving the Schrödinger equation for an electron in a lattice-periodic potential. Bloch theorem states that the wavefunction ψ can only change by a constant phase factor e^{ikr} when the particle is shifted by one lattice constant. Hence, the Bloch wave function is the product of a periodic part $U_{nk}(r)$, which is defined by the periodicity of the lattice, and a plane wave part:

$$\Psi_{nk}(r) = U_{nk}(r)e^{ikr} \tag{4}$$

Where n is a crystal band, Ψ is the wave function, $U_{nk}(r)$ is a function with the periodicity of the lattice, k is a wave vector, r is the position vector.

However, for a semiconducting material, an energy gap appears when the Schrödinger equation offers no solution for wavefunction at the Brillouin zone boundaries. When $k = \pm {}^{\pi}/_{a}$, there is an energy discontinuity at the Brillouin boundary, which is caused by the diffraction of the travelling wave at the boundary of the first Brillouin zone and results in a standing wave, hence creating a band gap (E_g).

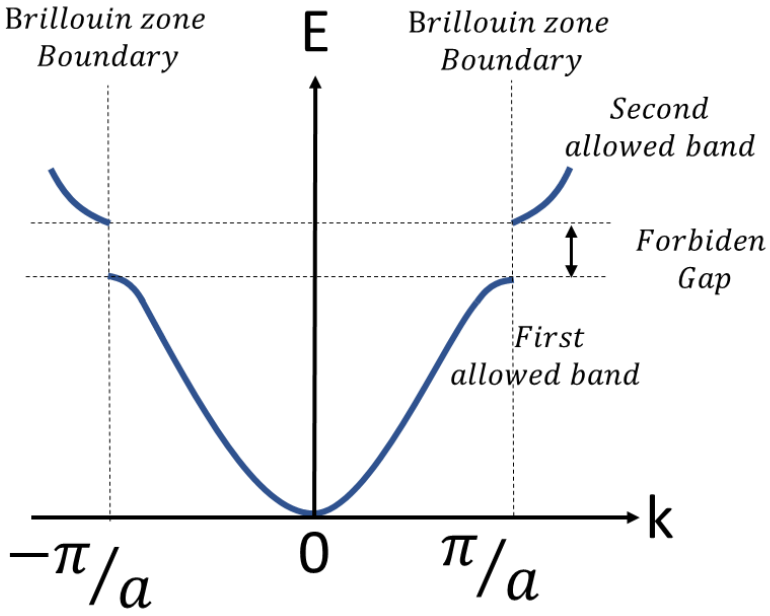


Figure 8: Energy versus wavevector k for an electron in a monatomic linear lattice of lattice constant a, showing the discontinuity in energy between the first and second Brillouin zone.

Stationary states, that can also be described as orbitals, are responsible for mathematically describing the wave-like behavior of electrons in an atom. They refer to functions which depend on the coordinates of an electron, and are used to approximate wave functions. The wavefunction $\Psi(r)$ describes the spatial extent at position r. Orbitals are commonly plotted as a boundary surface inside which there is a 95% probability of finding an electron, in the vicinity of a nucleus. However, we would need to include the entire universe in the orbital to obtain a 100% probability of finding this electron. Hence, a probabilistic interpretation approach is needed to define many behaviors observed in quantum mechanics.

As atoms are brought together to form a crystal, orbitals hybridize, where electrons start to interact with one another to form band of electronic levels, which can be interpreted as a continuum of energy states.[31] This electronic band structure, found in crystals and molecules, describe the allowed range of energies that an electron may occupy. However, semiconductor materials can also have forbidden energy states that arise from the periodicity of atoms and molecules. In solid-state physics, three distinct energy bands are commonly studied: valence band (VB), conduction band (CB) and band gap (E_g). These energy bands dictate the electrical and optical properties of semiconductor materials. At absolute zero, the valence band is defined as the highest completely filled band, while the conduction band is the lowest range of vacant electronic states. However, it is the presence of the

band gap, the difference between the conduction band and the valence band ($E_g = E_C - E_V$), which dominates the properties of semiconductor materials. In Figure 9, we show a schematic of electronic band structures for direct and indirect band gap semiconductors.

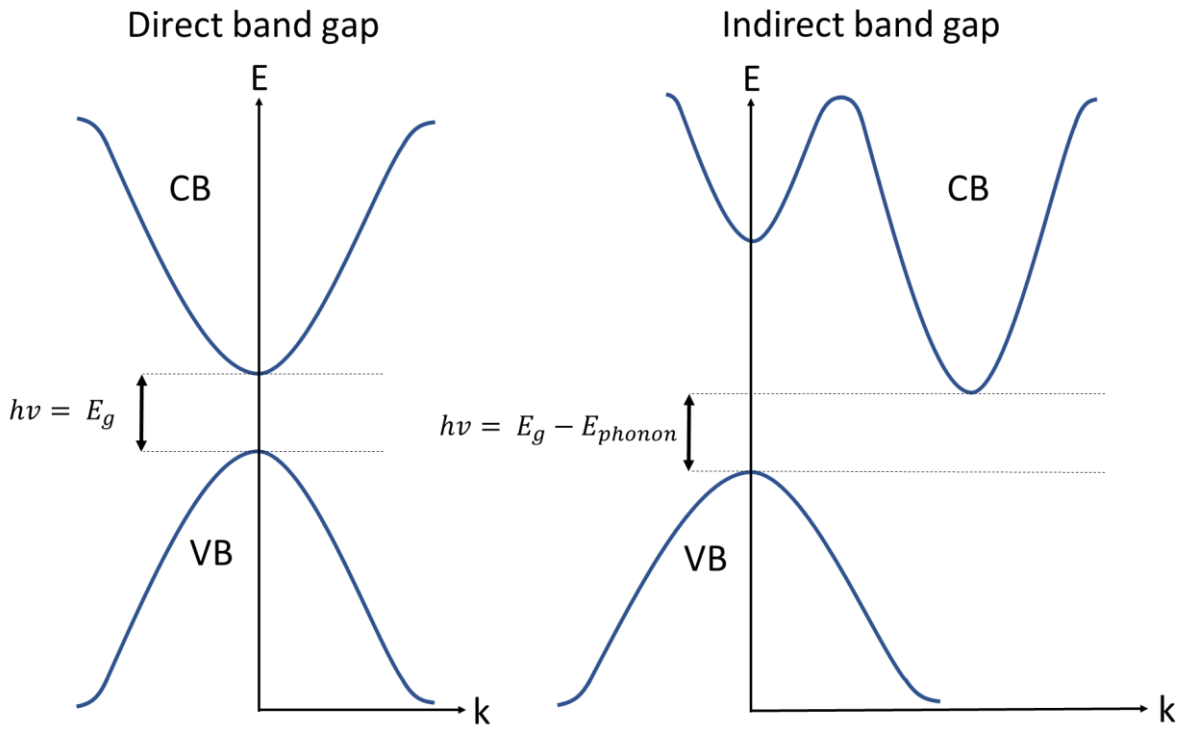


Figure 9: Schematic of a band structure diagram showing direct (left) and indirect (right) band gap.

A direct band-gap semiconductor will have its maximum energy state of the valence band aligned with the minimum energy state of the conduction band, with respect to momentum. Hence, in direct band gap semiconductors, direct recombination can take place, where an electron can directly emit a photon without the involvement of the phonon to carry crystal momentum. In turn, the probability of a radiative recombination is high. The same concept can be applied when a photon is absorbed by the material and a direct band-to-band transition can occur. On the other hand, an indirect band-gap semiconductor will have an offset in momentum between the maximum energy level of the valence band and the minimum energy level of the conduction band. Hence, this process requires a phonon with a momentum equal to the difference between the electron and hole momentum, in order to recombine.

As mentioned, quantum mechanics employs statistics and probability theory to study the average behaviors of quantum systems. The Fermi-Dirac distribution function provides the probability that an energy level, at energy E and temperature T, is occupied by an electron.[32]

$$f(E,T) = \frac{1}{1 + e^{\frac{E-E_F}{k_B T}}} \tag{5}$$

Where E is the energy, E_F is the Fermi energy, k_B is Boltzmann's constant, 8.62×10^{-5} (eV/K), and T is the temperature (K).

This function must obey the Pauli exclusion principle, which states that no two electrons in an atom can have the same set of four quantum numbers (n). Thus, two electrons in an atom can have the same n, l and m value, but must differ in spin quantum number. We note that at $T = 0$, the probability is equal to 1 for $E < E_F$ and zero for $E > E_F$. This means that at absolute zero, the valence band is full and electrons do not have enough kinetic energy to overcome the band gap and be excited to the conduction band. Thus, semiconductors cannot conduct electricity at $T = 0$, and only at finite temperatures can electrons from the VB be excited to the CB via various physical processes, allowing electrical conductivity. At zero kelvin, the fermi level E_F is the highest energy state that an electron can occupy. We note that E_F is the energy level which has a 50% probability of occupancy by an electron, at any temperature.

$$f(E_F) = \frac{1}{1 + e^{\frac{E_F-E_F}{k_B T}}} = \frac{1}{1 + e^{0}} = \frac{1}{2} \tag{6}$$

2.1.2. Semiconductor doping

We have introduced the concept of band structures in Section 2.1.1. In this section we briefly discuss how the energy band structure of a semiconductor can be alerted through the process of doping to modify the electronic and optical properties of an intrinsic semiconductor. An intrinsic semiconductor is a pure crystal that does not contain impurities. The process of doping is commonly done by introducing electron or hole donor impurities that create energy states near the conduction

band and valence band, respectively. A readily used semiconductor, silicon (Si), achieves doping with the introduction of impurities into the crystal lattice, which increases the conductivity of the overall semiconductor by a factor of 10^6. For the case of Si, a group V element, such as: phosphorus (P), arsenic (As), or antimony (Sb) can be introduced to n-dope the Si semiconductor. While, the group III elements, namely boron (B), aluminum (Al), gallium (Ga) are used to p-type the silicon structure. The concept of impurity doping is illustrated in Figure 10, where phosphorous (n-type) and boron (p-type) dopants are introduced in an intrinsic silicon crystal.

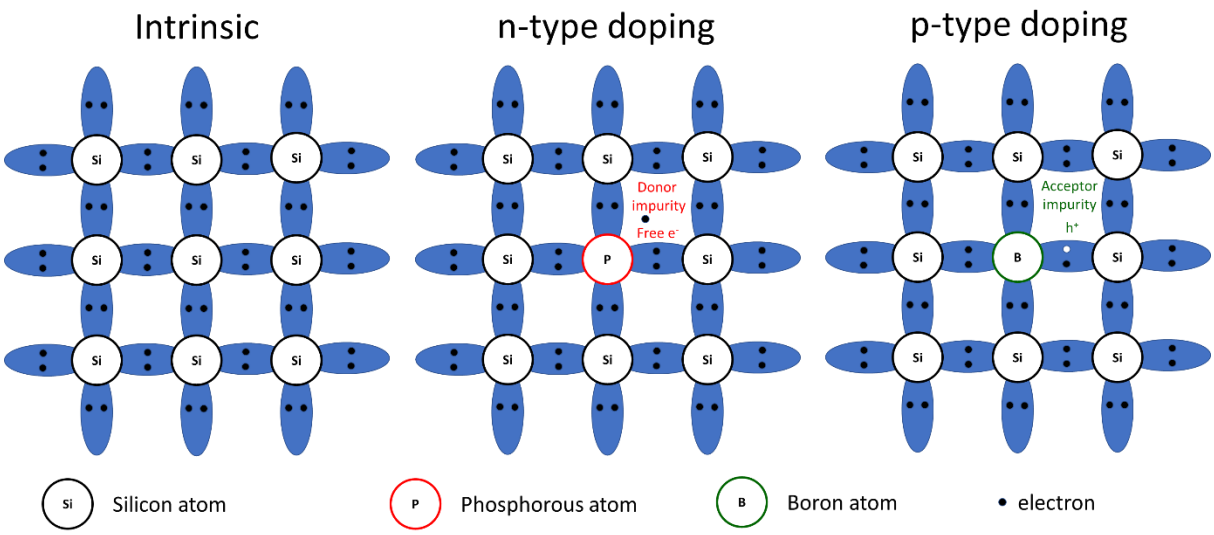


Figure 10: Schematic illustration of an intrinsic silicon semiconductor with no impurities (left), an n-type silicon semiconductor with boron as impurity dopant (middle), an p-type silicon semiconductor with phosphorous as impurity dopant (right)

In turn, these impurities impact the density of carriers in the semiconductor. For n-type semiconductors, the density of electrons is far superior to the hole density, hence the principal charge carriers are negative. Conversely, p-type semiconductors have a high density of positively charged carriers relative to the negatively charged carriers. However, it is important to specify that these impurities must create shallow energy states. Shallow impurities require little energy to ionize. Shallow energy states levels are characterized as being less than $3k_BT$ (~75 meV at room temperature) away from the conduction or valence band.[33] If the new energy levels, introduced by the impurities, are greater than this value, they are considered as deep-level traps, which are an undesirable type of defect. These deep-level defect states offer an intermediate state within the band gap which create a recombination center that shortens the lifetime of charge carriers. Hence, it is important to choose dopants that create energy states that have an ionization energy of the order of

$k_B T$. In Figure 11, we illustrate the effects of doping on the position of the Fermi level in a band diagram of an intrinsic semiconductor.

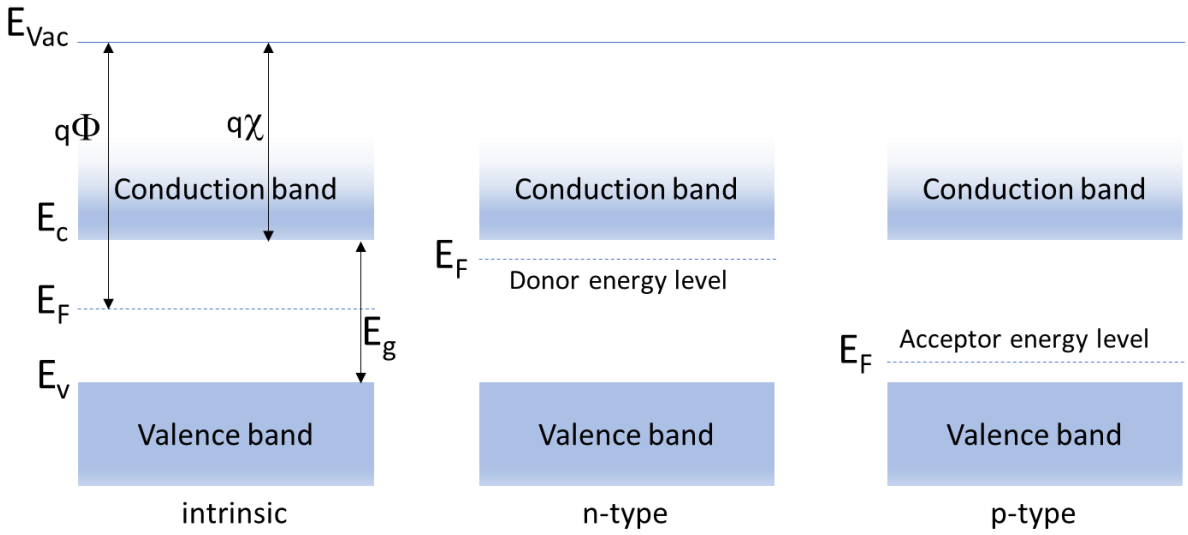


Figure 11: Schematic illustration of the band diagrams and Fermi energies of intrinsic, p-type and n-type semiconductors.

In a semiconductor, the work function is defined by the difference in energy between the fermi level E_F and the vacuum level E_{Vac}. Hence, the work function of the semiconductor, is the least amount of energy required to remove an electron from the crystal lattice to a point in vacuum.

$$\Phi = E_{Vac} - E_F \tag{7}$$

The vacuum level is defined as the potential energy of an electron in vacuum, which is taken as zero. It is the difference in energy between the conduction band and the vacuum level E_{Vac}. In metal, the work function is equal to the electron affinity, since the Fermi level resides in the conduction band.

In intrinsic semiconductors, using Boltzmann approximation for non-degenerate semiconductors, the expression for electron n and hole p carrier densities can be simplified and defined as:

$$n = N_c e^{\frac{E_F - E_c}{k_B T}} \tag{8}$$

$$p = N_V e^{\frac{E_V - E_F}{k_B T}} \tag{9}$$

Where N_c is the effective conduction band density of states, and N_V is the effective valence band density of states.

We can immediately observe that the electron and hole density vary exponentially with respect to the position of the Fermi level in the band gap. We can define the intrinsic carrier density n_i as a constant property of the material with the given relationship:

$$n_i^2 = np = N_c N_V e^{-\frac{E_g}{k_B T}} \tag{10}$$

The position of the Fermi level in equilibrium determines the conductivity of an intrinsic semiconductor. Intrinsic semiconductors have n electron and p holes available for conduction, where conductivity is given by:

$$\sigma = q\mu_n n + q\mu_p p \tag{11}$$

Where μ_n, and μ_p are the mobilities of the electron and holes, respectively, q is the elementary charge, and n and p are the total density of electrons and holes in the crystal.

At room temperature, an intrinsic semiconductor usually exhibits low conductivity. As in the case of intrinsic silicon, which has a conductivity (σ) of 3E-6 Ω^{-1} cm^{-1}, at 300 K.[27] However, by moving the Fermi level closer to the conduction or valence band, via doping, we can effectively control the conductivity of the semiconductor. The density of carriers can be controlled by varying the density of dopants in the crystal lattice, N_d for donor concentration, and N_a for acceptor concentration. For a doping density of $N_d \gg n_i$, and $N_a \gg n_i$ and assuming the donors and acceptors are fully ionised at room temperature, we find

$$n \approx N_d \ , \ p \approx N_a \tag{12}$$

and

$$p = \frac{n_i^2}{N_a} \ , \ n = \frac{n_i^2}{N_d} \tag{13}$$

Hence, the total carrier density for both n and p-doped semiconductors is greatly increased. In turn, the conductivity of these material is also increased. We note that conduction is governed by the majority carriers, electrons in the case of n-type semiconductors, and holes in the case of p-type semiconductors. Finally, we can relate the position of the Fermi level with the dopant concentration by the following:

$$E_F = E_i + k_B T ln\left(\frac{n}{n_i}\right) \tag{14}$$

For n-type semiconductors, and:

$$E_F = E_i - k_B T ln\left(\frac{p}{n_i}\right) \tag{15}$$

For p-type semiconductors.

2.1.3. Absorption, generation and recombination

We have previously discussed the particle-wave dualism property of light. Max Planck and Albert Einstein described it using a quantum-mechanical particle called a photon. This is the smallest unit of light intensity, and does not possess a mass. However, a photon possesses energy, which can be characterized by the given equation:

$$E = hv = \frac{hc}{\lambda} \tag{16}$$

Where h is Planck's constant, c is the speed of light, v is the frequency, and λ is the wavelength.

Furthermore, a photon possesses a momentum of magnitude p in a medium, which is determined by its wavelength in this medium:

$$p = \frac{h}{v} \tag{17}$$

The direction of the motion of the photon is defined by wave vector $\boldsymbol{k}$, with magnitude k

$$k = \frac{2\pi}{\lambda} \tag{18}$$

Finally, the momentum of a photon $\boldsymbol{p}$ is proportional to the wave vector

$$\boldsymbol{p} = \hbar \boldsymbol{k} \tag{19}$$

The photoelectric effect describes the dislodgement of electrons when light shines on a material. However, the emission of an electron, after the impingement of a photon, can only occur if the energy of a photon is equal or greater than the band gap of the material. Hence, for each material, there is a threshold frequency at which light absorption is possible:

$$h\nu \geq E_g \tag{20}$$

Otherwise, light simply passes through the material, and the photon cannot transfer its energy to the electron or the lattice. The absorption of the photon allows for the creation of an electron-hole pair, where an electron gets promoted from the valence band to the conduction band. This lack of an electron in the valence band is called a hole, and treated as a positively charged particle. The excited electron then relaxes down towards the minima of the conduction band by losing its energy through carrier-carrier and carrier-phonon scattering.[34] This thermalisation process, which occurs in the femtosecond regime, represents a complete loss in energy, equating to the difference in energy between the photon and the band gap.

$$E_{therm\ loss} = h\nu - E_g \tag{21}$$

Finally, an electron will recombine with a hole, and within a microsecond, release its energy either by emitting a photon or in the form of lattice vibration. However, in a solar cell, the electron in the conduction band is transported to the electron-collecting electrode via diffusion or drift caused by

an external electric field. We explain in further detail this process in Section 2.1.4. We show a schematic of this entire absorption process in Figure 12.

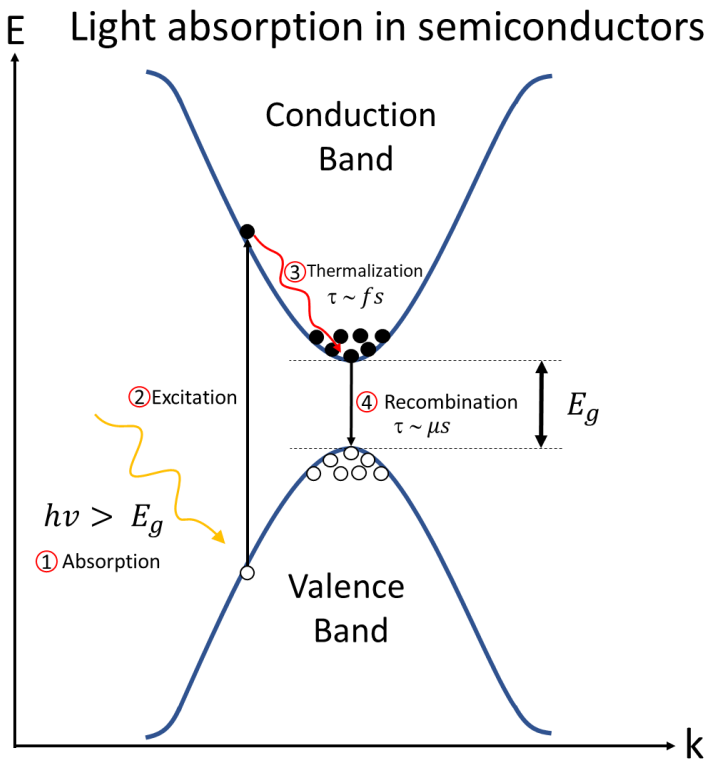


Figure 12: Absorption process that leads to the promotion of an electron from the valence band to the conduction band. After excitation, thermalization and recombination processes can take place.

Understanding the recombination processes that take place in semiconductor devices is key towards improving the performance of the devices. These recombination processes lie at the heart of the working principle of LEDs, which convert energy of the electron-hole pair to light. We refer to recombination as a loss of free electrons or holes that can occur by various mechanisms. To be precise, radiative recombination is required for proper operation, as opposed to non-radiative recombination. Hence, in both LED devices and solar cells, it is imperative to limit and minimize non-radiative recombination pathways, which leads to energy being lost as heat. Three major types of recombination will be discussed in this section: radiative (e.g. band-to-band) recombination, Shockley-Read-Hall (e.g. trap-assisted) recombination, and Auger recombination (shown in Figure 13).

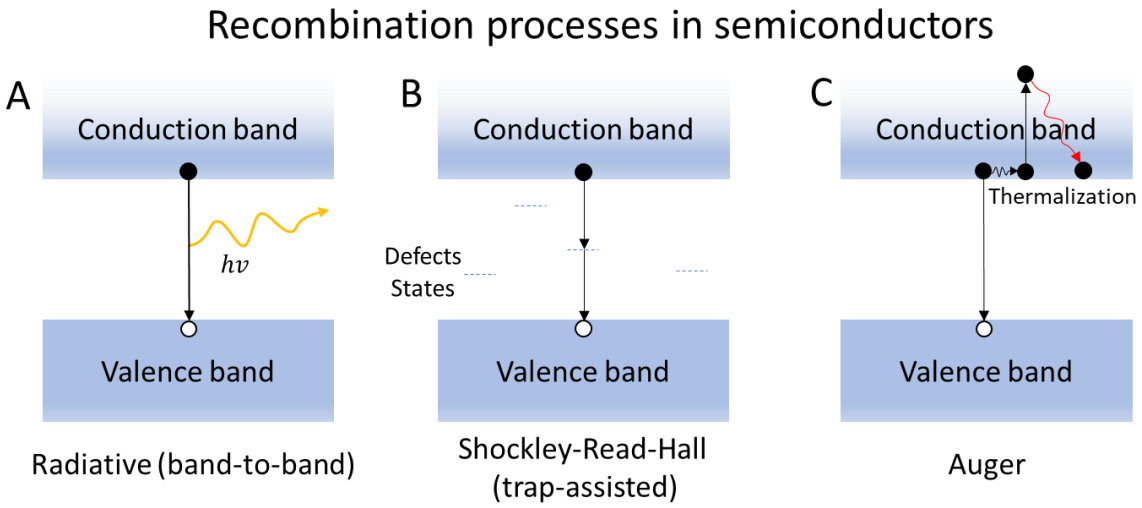


Figure 13: Recombination processes in semiconductors. *A) Radiative (band-to-band) recombination B) non-radiative Shockley-Read Hall (SRH) trap-assisted recombination C) non-radiative Auger recombination.*

As shown in the equation below, we must include the contributions of all three of these recombination mechanisms to obtain the total lifetime for a minority charge carrier. However, we will see that some types of recombination are more likely to occur than others, depending on the properties of the material (e.g. energy band structure), material quality (e.g. defects) and external conditions (e.g. light, applied bias).

$$\frac{1}{\tau} = \frac{1}{\tau_{Rad}} + \frac{1}{\tau_{SRH}} + \frac{1}{\tau_{Auger}} \tag{22}$$

Where τ is the total lifetime for a minority charge carrier, τ_{Rad} is the radiative recombination lifetime, τ_{SRH} is the Shockley-Read-Hall recombination lifetime, and τ_{Auger} is the Shockley-Read-Hall recombination lifetime.

Radiative recombination is an unavoidable recombination process which results in a spontaneous emission of a photon. This process is the basis of LEDs and lasers, which rely on direct band gap material, instead of indirect band gaps, since the rate of radiative recombination is much lower for the latter. For example, in silicon, radiative recombination only plays a significant role at high doping concentrations (>10^{17} cm^{-3}).[35] However, for a direct band gap, such as GaAs, this is a major

concern for identical doping concentrations. We also note that radiative recombination will greatly differ between high and low injection levels. The τ_{Rad} radiative recombination lifetime is given by:

$$\tau_{rad} = \frac{n_0 p_0}{B n_i^2 (n_0 + p_0)} \tag{23}$$

Where n_0 and p_0 are the concentration of electrons and holes at equilibrium, n_i is the intrinsic carrier concentration, and B is the bimolecular recombination coefficient.

Radiative recombination is not as detrimental to performance as non-radiative recombination, since this recombination process creates a photon from a spontaneous emission, which has a probability to be reabsorbed. On the other hand, non-radiative recombination processes, such as SRH and Auger recombination, convert the energy of the electron into vibrational energy of the lattice atoms (i.e. phonons). Hence, in solar cell application, photon energy is ultimately dissipated into heat rather than being converted to electricity. Auger recombination is also an unavoidable recombination process, where an electron recombines with a hole, and instead of generating a photon, the excess energy is transferred to a second electron. This excited electron then relaxes back to the edge of the band and transfers its energy to lattice vibrations. Auger recombination only becomes significant in non-equilibrium conditions when the carrier density is very high. Reducing the doping density in the material can help to reduce Auger recombination. Furthermore, this three-particle interaction is the dominant loss mechanism in pure indirect band gap semiconductors compared to direct band gap, where radiative recombination is predominant. The Auger recombination rate U_{Auger} is given by:

$$U_{Auger} = C_n n^2 p + C_p p^2 n \tag{24}$$

Where C_n and C_p are Auger coefficients.

Lastly, we will discuss an avoidable non-radiative recombination process: Shockley-Read-Hall (SRH) recombination. This recombination process is caused by defects in the crystals structure, which create deep energy levels located within the band gap. These energy levels are mid-gap trap states that act as a recombination center for charge carriers. Here, an electron can relax into the trap, thus

filling this mid-gap level state, whereby the electron falls into an empty valence band state and completes the combination process. This energy is transferred to the lattice in vibration form. These deep-level traps are located in the bulk of the material, in the form of unwanted foreign atoms, doping impurities, native defects, and dislocations, or at the interface, in the form of dangling bonds. The Shockley-Read-Hall recombination rate is given by:

$$U_{SRH} = \frac{np - n_i^2}{\tau_{n,SRH}(p + p_t) + \tau_{p,SRH}(n + n_t)} \tag{25}$$

Where $\tau_{n,SRH}$ and $\tau_{n,SRH}$ are given by:

$$\tau_{n,SRH} = \frac{1}{B_n N_t} \quad , \quad \tau_{p,SRH} = \frac{1}{B_p N_t} \tag{26}$$

Where N_t is the trap concentration.

2.1.4. Semiconductor junctions and solar cell operation

In previous sections, we discussed the charge generation aspects in semiconductors, which transfer energy from a photon to an electron to promote it to an excited state. However, in the case of photovoltaics, we not only need to generate long lived charged-carriers, but we also need to separate these charges to extract them at their respective electrodes. Charge separation is the process of transporting photoexcited free mobile electrons in one direction, while moving their corresponding holes in another. A driving force is required for spatial charge separation to occur. In principle, there are various methods of obtaining this charge separation mechanism in a semiconductor material:[27]

- Vaccum level or work function gradient
- Electron affinity gradient
- Band gap gradient
- Band density of states gradient

These gradients provide means of driving the electrons in the direction of the cathode, while simultaneously driving holes in the opposite direction, where they will be collected by the anode. These gradients, which provide the necessary driving force for the operation of the solar cell, can be achieved by putting into contact metals or semiconductor materials with different work function or band structures, thus creating a heterojunction. Another method relies on varying the doping concentrations and/or doping element from donor to acceptor within a same semiconductor material, hence forming a homojunction. Lastly, we will discuss in this section the use an applied electric field to induce charge separation and extraction.

The metal-semiconductor interface is one of the simplest semiconductor devices. Depending on the choice of metal and semiconductor, this junction can either form a Schottky barrier with a rectifying behaviour, or an ohmic contact with non-rectifying behaviour. The type of contact greatly impacts how electrons and holes can be transferred from one material to another. Furthermore, when these materials are put into contact, a space charged region, also called a depletion region, forms at the interface. As we contact both materials together, electrons and holes diffuse from regions of high concentration to regions with lower concentrations, to create an equilibrium. The departure of an electron from one material to another leaves a positive donor ion behind, or in the case of the migration of a hole, where it leaves a negative acceptor ion behind. This creates an interface with uncompensated ions, which have no mobile charges, thus carriers are depleted, hence the name "depletion region". The width (W) of this region can be approximates with the given relation:

$$W = x_p + x_n = \sqrt{\frac{2\varepsilon}{q} V_{bi} \left(\frac{1}{N_A} + \frac{1}{N_D}\right)} \tag{27}$$

Where,

$$x_p = W \frac{N_D}{N_D + N_A} \quad , \quad x_n = W \frac{N_A}{N_D + N_A} \tag{28}$$

The depletion region produces a built-in field, which is equal to the potential across the depletion region in thermal equilibrium. The potential is equal to the difference in fermi energies of each region. This yields the following expression for the built-in potential:

$$V_{bi} = \frac{kT}{q} \ln\left(\frac{N_A N_D}{n_i^2}\right) \tag{29}$$

However, we note that this equation only holds assuming specific approximations, which may not occur in practical devices. These assumptions include: constant doping concentration, step doping profiles, and that all dopants are ionized.

Due to space charge effects when material contact together, we create a bending of the bands resulting in an energetic gradient at the interface. This band bending provides an energetic offset for electrons to flow in a direction, while holes flow in the opposite direction. In the simple case of a metal-semiconductor junction, where the work function of the metal Φ_m is greater than the work function of the semiconductors Φ_s, a Schottky barrier arises when the materials are put into contact. We show the band structure of the Schottky diode in Figure 14.

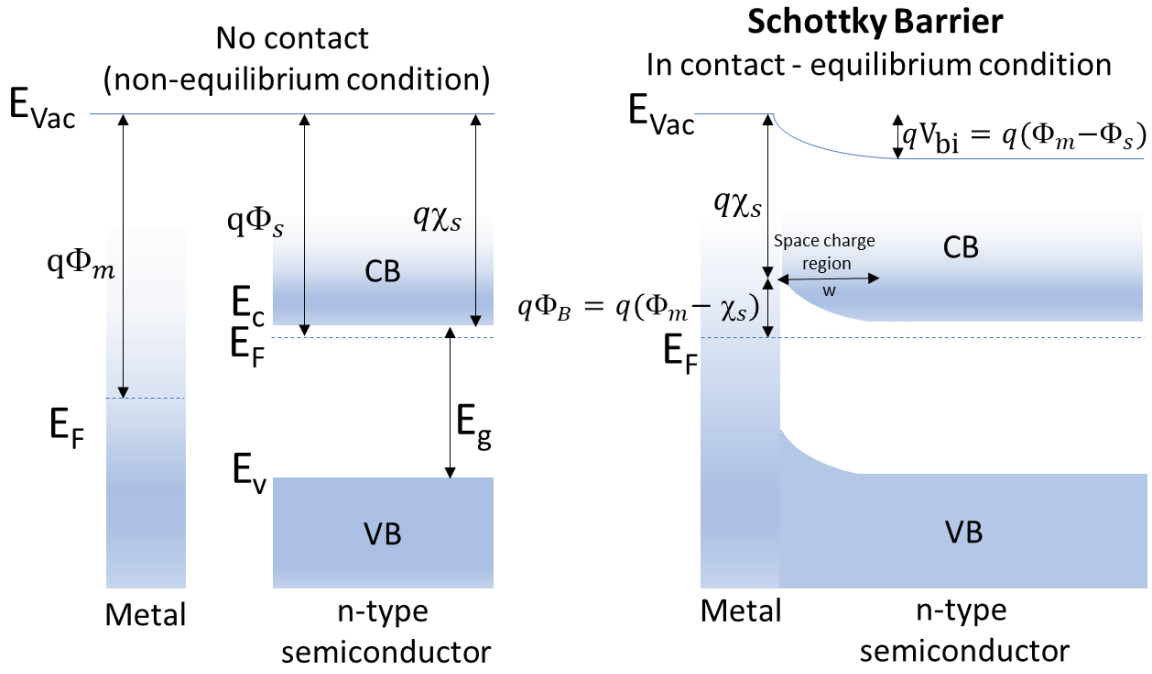


Figure 14: Band diagram of a metal to n-type semiconductor interface. A) In non-contact B) In contact. When in equilibrium, a Schottky barrier forms at the interface.

Once the n-type semiconductor and metal are put into contact, an equilibrium of charges is produced, creating a depletion region. In this particular case, in order for the Fermi levels of both materials to align, an upwards band banding occurs at the interface of the n-type semiconductor. Hence, the valence and conduction band need to bend in accordance with the bending of the vacuum level. This band bending relates to the built-in potential of the device, given by V_{bi}. This specific junction is called a Schottky diode, where an energetic barrier, a Schottky barrier, of magnitude $q\Phi_B$

prevents the electrons in the conduction band of the semiconductor from being transferred to the metal. However, it is important to note that this phenomenon is not true for all metal-semiconductor interfaces. In

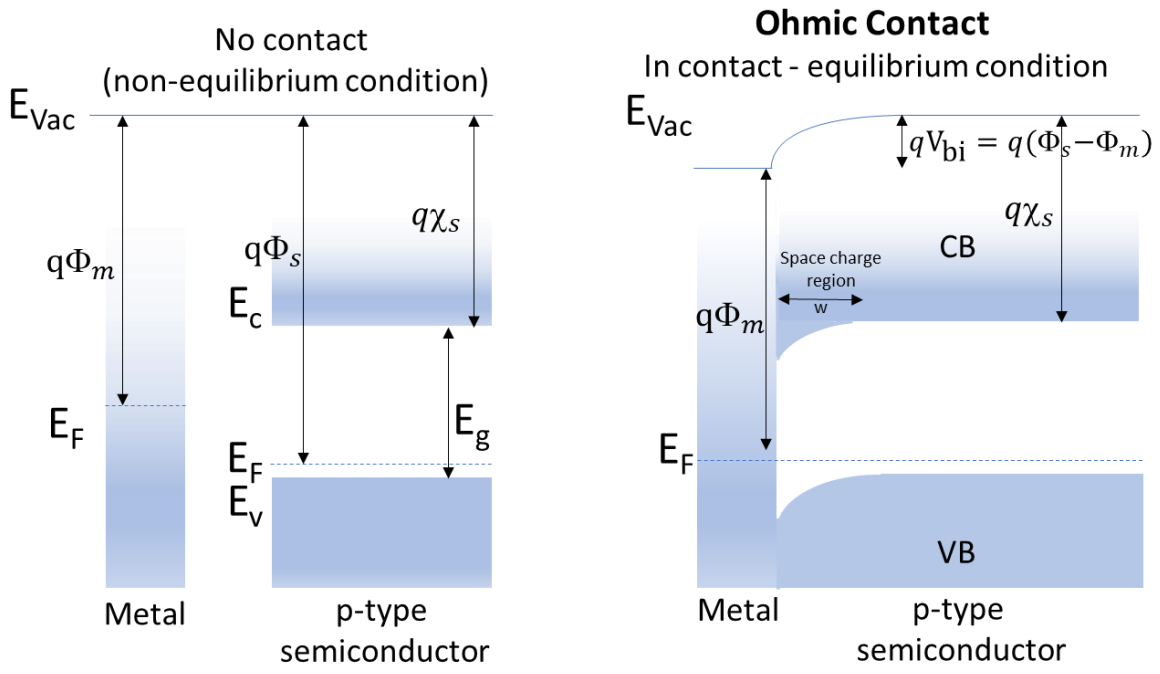


Figure **15**, we show that by changing the Fermi-level of the material, and creating a p-type semiconductor, we effectively create an ohmic contact at the metal-semiconductor interface.

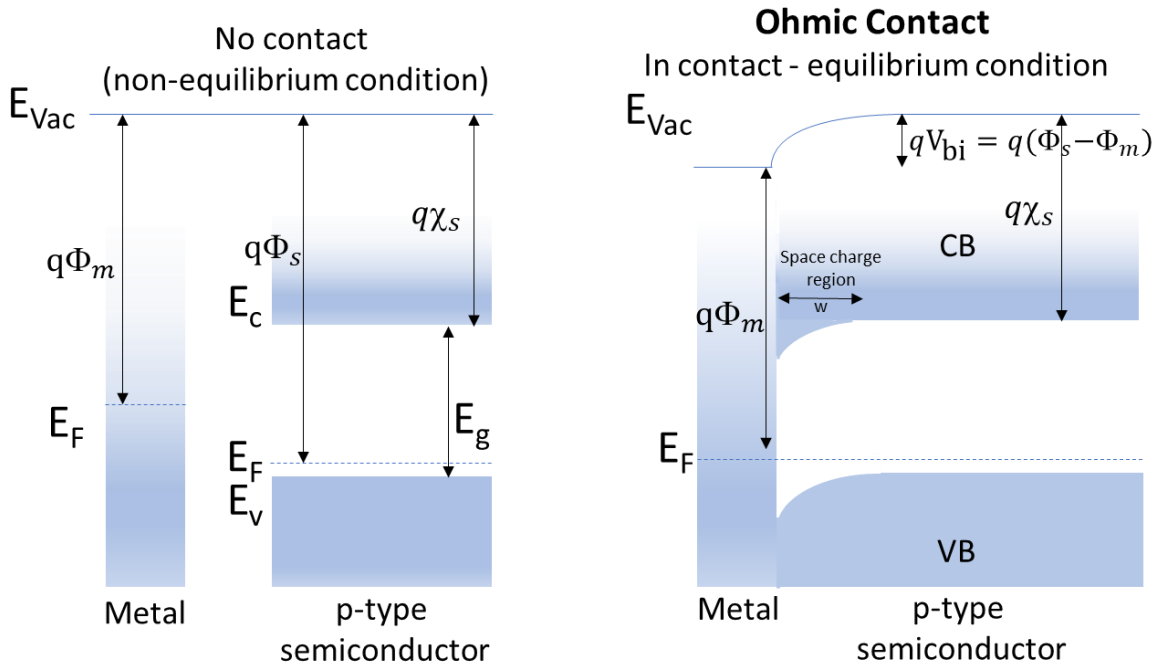


Figure 15: Band diagram of a metal to p-type semiconductor interface. A) In non-contact B) In contact. When in equilibrium, an ohmic contact forms at the interface.

Conversely to the Schottky barrier, the ohmic contact allows for electrons to efficiently travel from the semiconductor to the metal. The ohmic contact represents a low resistance junction between a metal and a semiconductor. In this case, the current is linearly proportional to the voltage. Here, the work function of the metal Φ_m must be lower than the work function of the semiconductors Φ_s.

The metal-semiconductor interface is one of the simplest methods of creating a junction. However, it is not an ideal junction to separate charge for a solar cell application, since this junction does not produce the highest photovoltage. When the barrier height Φ_B is larger than $\sim\frac{E_g}{2}$, an inversion layer is formed close to the interface, where minority carriers outnumber the majority carriers.[27] Furthermore, this junction leads to interface states, which lead to the trapping of charges and interface recombination. Thus, higher complexity junctions with improved performances are employed for solar cell application, namely the p-n and the p-i-n junction. We show in Figure 16 these two frequently employed architectures for solar cell applications.

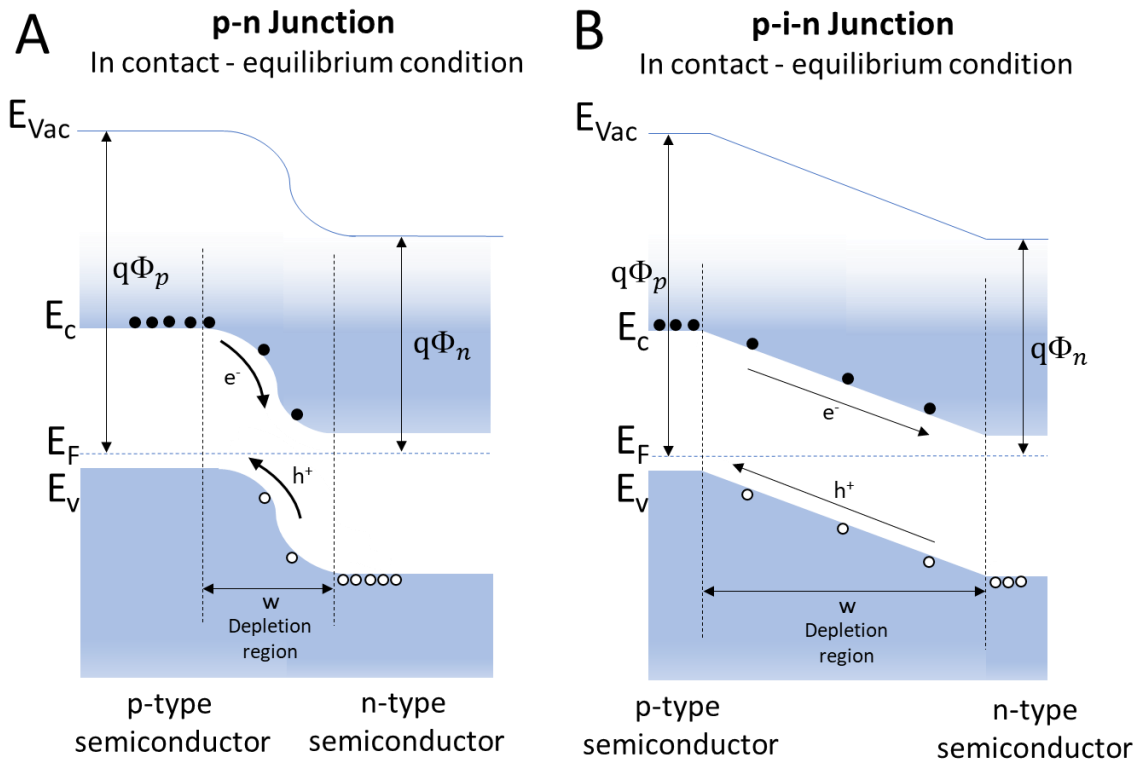


Figure 16: Band diagram of semiconductor-semiconductor junctions*. A) A p-type semiconductor in contact with a n-type semiconductor, forming a p-n junction. B) An intrinsic (i) semiconductor sandwiched in-between a p-type semiconductor and an n-type semiconductor, forming a p-i-n junction.*

The p-n junction is fabricated by doping a semiconductor of the same material with a donor dopant, to create an n-type semiconductor, and an acceptor dopant to create a p-type semiconductor. Once these semiconductors are in contact, they create a homojunction. In this case, the space charged region is depleted of both holes and electrons. In comparison to the Schottky diode, this type of junction has the benefit of significantly reducing defect states located at the metal-semiconductor interface. Thus, a significantly larger built-in voltage can be obtained.

The p-i-n junction uses an intrinsic (undoped) semiconductor, sandwiched in-between a p-type semiconductor and an n-type semiconductor. This architecture can be fabricated using identical semiconductor material, forming a homojunction. In the case of thin-film solar cells, this architecture is necessary to preserve high charge-carrier lifetimes in the absorber layer. When doping materials, we introduce defects, thus lowering the lifetimes of the minority carriers in the semiconductor. This is especially crucial for thin-film technology, where carrier diffusion lengths are usually orders of magnitude lower than un-doped silicon. Hence, when doping of the materials is undesirable, a p-i-n architecture may instead be used to extract charges from the semiconductor. Free-carriers are

generated in the intrinsic layer, and transported to their respective electrodes via the driving forces we have previously identified. The doped semiconductor creates a depletion region across the intrinsic layers. By choosing semiconductors with appropriate conduction and valence band, they can serve as a selective contact layer to a specific carrier, while simultaneously blocking carriers with opposite charge, thus reducing interface recombination.

In standard solar cell application, we can identify two different driving forces in these types of semiconductor junctions, which generate two types of currents: the drift current and the diffusion current. The summation of these two currents result in the total flow of charge through the semiconductor:

$$J = J_{diffusion} + J_{drift} \tag{30}$$

The diffusing current arise from the variation in the carrier concentration across the semiconductor material, which in turn produces an electric field in the junction. This gradient causes charge carriers to move from the high carrier concentration region to the lower carrier concentration region, hence diffusion occurs. This movement of charges results in a net diffusion current. This concentration gradient can be achieved through doping of an intrinsic semiconductor, for example, at the interface of a p-n junction, where a flow of majority carriers towards and across the junction will occur via diffusion. The diffusion current can be characterised using Flicks law, which describes diffusion as the flux F of particles being proportional to the gradient in concentration:

$$F = -D\nabla n \tag{31}$$

Hence,

$$J_n = -qD\frac{dn}{dx} \quad , \quad J_p = -qD\frac{dp}{dx} \tag{32}$$

Where n is the concentration, D is the diffusion coefficient, and J is the diffusion current density.

Conversely, the drift current is created by the motion of charge carriers caused by the force exerted on them by an external electric field, such as the simple case of applying a potential across a metal wire. This potential causes free electrons to move towards the positive electrodes, while holes create a flow in the direction of the negative electrode. The drift current obeys ohms law, given by:

$$J_n = q\mu_n nE \quad , \quad J_p = q\mu_p pE \tag{33}$$

Where μ_n is the mobility of electrons, μ_p is the mobility of holes, E is the Applied Electric Field Intensity and J is the drift current density.

By changing the polarity of the external voltage, we alter the direction of the drift current and impact the bending of the bands. In turn, the applied voltage and polarity causes changes to the width of the depletion region. In forward bias, the positive terminal of the power source is connected to the p-type region, and the negative terminal is connected to the n-type region. This causes the positive terminal to repel the holes in the p-type region and the negative terminal to repel the electrons in the n-type region towards the space-charge region. In turn, the depletion region is narrowed under forward bias, and the inverse scenario occurs for reverse bias, where the depletion region is widened under this condition.

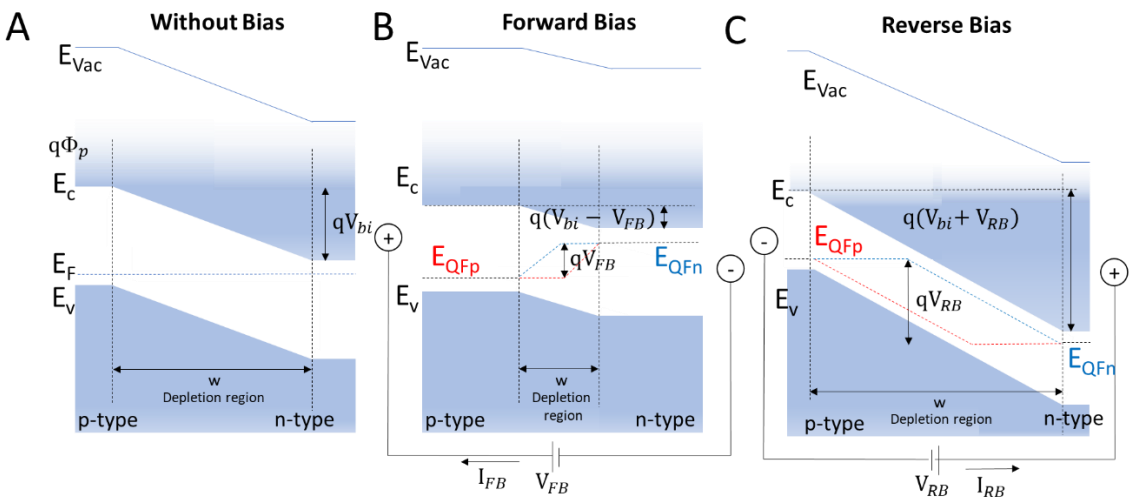


Figure 17: Effect of bias on the energy band diagram*. A) Energy band diagram in equilibrium, without any voltage bias. B) In forward bias C) In reverse bias.*

In thermal equilibrium, the quasi-Fermi levels for both holes and electrons are equal to the Fermi-level. However, an applied voltage alters the populations of electrons in the conduction band and valence band from their equilibrium position, thus, causing the splitting of the quasi-Fermi levels. This quasi-Fermi level splitting is also achievable through the illumination of the p-n junction, due to an increase in the electron and hole population. The difference between the two quasi-Fermi energies, results in the open-circuit voltage.

2.1.5. Solar cell characterization

The purpose of a solar cell is to convert light into electricity. However, the photon energy must be greater than the band gap of the absorbing material ($E_{photon} > E_g$). Hence, only a portion of the solar spectrum can be converted to electricity. The sun has a temperature of approximately 5800 K, which allows us to approximate with a black body radiation spectrum. However, we note that since the temperature is not completely uniform from the core to the surface, it differs slightly from the theoretical black-body radiation spectrum. Furthermore, sunlight is filtered through Earth's atmosphere, which causes scattering and absorption at specific wavelength, primarily due to H_2O, CO_2 and O_2 molecules. Hence, the air-mass (AM) coefficient defines the optical path length through the Earth's atmosphere. This coefficient is characterized as a ratio between the path length through the atmosphere L and the zenith path length L_0 (i.e. normal to the Earth's surface), given by:

$$AM = \frac{L}{L_0} \approx \frac{1}{\cos z} \tag{34}$$

Where z is the zenith angle in degrees.

The air mass number is readily used, since the sun's elevation path through the atmosphere changes throughout the day and year. The AM 1.5 spectrum represents an overall yearly average for mid-latitudes, which corresponds to a solar zenith angle of 48.2°. This spectrum has been selected for standardization purpose.

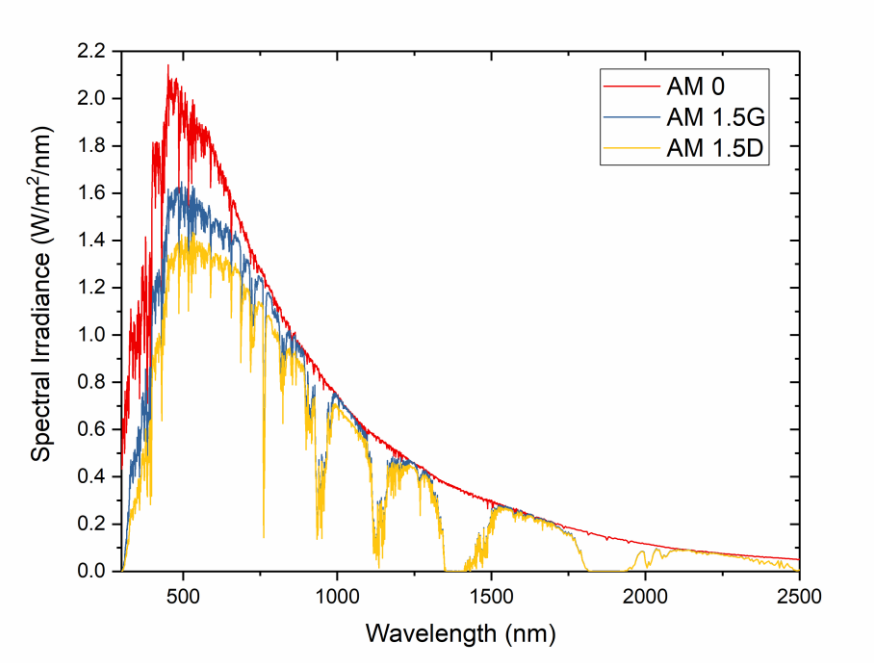


Figure 18: Solar irradiance terrestrial spectra of (AM1.5 Global and AM1.5 Direct), and the extraterrestrial spectrum (AM 0).

The solar intensity is approximately 1367 W/m^2 for the AM0, 1000 W/m^2 for AM1.5G, and 900W/m^2 for the AM1.5D spectrum. The AM 1.5G spectral irradiance, along with the 1000 W/m^2 power density, and a temperature of 25 °C is the standardized incident light spectrum used to characterize the efficiency of a solar cells. By precisely controlling the radiant flux shined upon the surface area of the solar cell, while simultaneously measuring the power output of the device, we can calculate the power conversion efficiency (PCE) of the photovoltaic device:

$$PCE = \frac{Electrical\ maximum\ power\ output}{Incident\ radiation\ flux * Area\ of\ collection} = \frac{P_{max}}{P_{Incident}} \quad (35)$$

Where P_{max}, is the maximum power output generated by the solar cell, and $P_{Incident}$ is the incident light power density.

The power is given by the product of current and voltage. However, the efficiency is reported at the maximum power point, the voltage point at which the power is at its maximum. By sweeping the applied voltage to the solar cell and measuring the current density, we can extract the current-voltage (JV) characteristics of the solar cell, along with its critical parameters such as open-circuit voltage V_{OC}, short-circuit current density J_{SC}, current density at maximum power point J_{mpp}, voltage at maximum power point V_{mpp}, and fill-factor (FF). In Figure 19 we show a typical JV curve response from a solar cell under AM1.5 spectrum at 1000 W/m^2 and under dark.

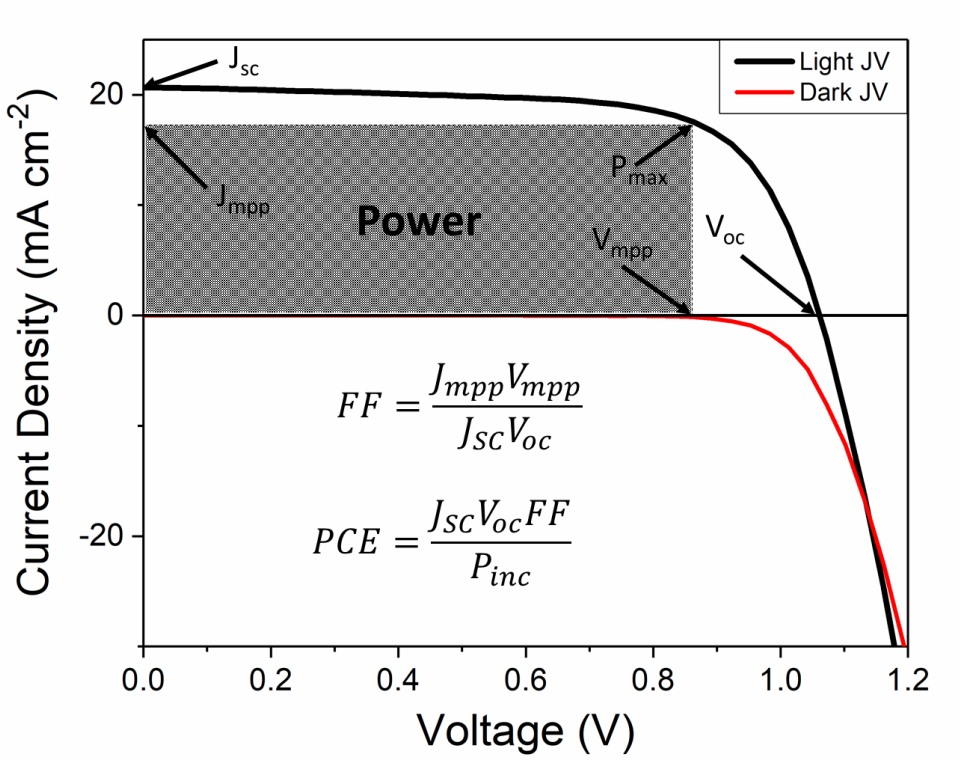


Figure 19: The current-voltage curve for photovoltaic device under light (black) and under the dark (red) conditions. *The shaded area represents the maximum power attainable from the device under test.*

In the dark, the basic solar cell responds as a diode. We can extract valuable information on the diode behavior of the solar cell by simply measuring the current vs voltage curve under dark. The sensitivity of this measurement allows for the extraction of critical parameters from the J-V curve, such as: series resistance (R_s), shunt resistance (R_{shunt}), diode factor (n) and the reverse saturation current (J_0). For an ideal diode, this current-voltage relationship is given by:

$$J_{Dark}(V) = J_0(e^{\frac{qV}{k_B T}} - 1) \tag{36}$$

Under illumination, this ideal diode equation considers the generated short-circuit (J_{SC}), and hence becomes:

$$J_{light}(V) = J_{sc} - J_0(e^{\frac{qV}{k_B T}} - 1) \tag{37}$$

The power generated by the solar cell is dependent upon the load connected to its terminals. The short-circuit condition is created by the photogeneration of carriers that reach their respective contacts. In this condition, the external load is set to zero, hence the J_{SC} is maximized, however, the cell does not generate any voltage, hence the power output is null. The J_{sc} generated by the device is then given by the integration of the product of the external quantum efficiency (EQE) and the solar spectrum:

$$J_{sc} = q \int_0^{\infty} EQE(E)\, \Phi_{\mathrm{AM1.5}}(E) dE \tag{38}$$

Where E is the energy of a photon and $\Phi_{\mathrm{AM1.5}}$ is the photon flux of the AM1.5 spectrum.

The eternal quantum efficiency (EQE) is the probability of an incident photon of energy E delivering one electron to the external circuit, given by:

$$EQE = \frac{Output}{Input} = \frac{number\ of\ eletrons}{number\ of\ photons} \tag{39}$$

On the other hand, the open-circuit condition is when the external load is set to infinite. In this case, the drift current cancels out with the diffusion current, hence all carriers recombine, which results in no net current. The open-circuit voltage is given by:

$$V_{oc} = \frac{kT}{q}\ln(\frac{J_{sc}}{J_0} + 1) \tag{40}$$

We can also relate the V_{oc} to the carrier concentration with the following relation:

$$V_{oc} = \frac{k_B T}{q}\ln(\frac{(N_A + \Delta n)\Delta n}{n_i^2}) \tag{41}$$

Where V_{oc} is the open-circuit voltage, q is the elementary charge, k_B is the Boltzmann's constant, V is the voltage, n is the ideality factor of solar cell, T is the temperature, N_A is the doping concentration, Δn is the excess carrier concentration, and n_i is the intrinsic carrier concentration.

Together with open-circuit voltage and short-circuit current, the fill factor is an important metric for photovoltaic devices. The FF is impacted by both the series resistance (R_s) and the shunt resistance (R_{shunt}). The FF is the ratio of maximum obtainable power to the product of the open-circuit voltage and short-circuit current, thus given by the following relationship:

$$FF = \frac{P_{max}}{P_{Incident}} = \frac{J_{mpp}V_{mpp}}{J_{sc}V_{oc}} \tag{42}$$

Where FF is the fill-factor, P_{max} is the maximum power output, $P_{Incident}$ is the power of the incident light, J_{mpp} is the current density at maximum power point, V_{mpp} is the voltage at maximum power point, J_{sc} is the short-circuit current-density, and V_{oc} is the open-circuit voltage.

The shunt and series resistances are parasitic resistances which affect the ideal J-V characteristic curve, and hence impact the overall performance of the device. When the series resistance increases, we notice a loss in the steepness of the J-V curve near the V_{oc}. This resistance arises from the combination of all the series resistances in the solar cell, including the intrinsic bulk resistance of all material and the contact resistances. This resistance scales quadratically with the photogenerated current, hence R_s becomes more impactful at high illumination fluences. A decrease in shunt resistance can originate from non-uniformities in the absorbing layer or the electron or hole accepting layer, and cause shunt paths. The device with low R_{shunt} results in a slope between the J_{sc} and the J_{mpp} of the JV curve. This creates a leakage current, which is considered a loss to the net current density, and must be subtracted from the ideal diode equation:

$$J(V) = J_L - J_0\left(e^{\frac{q(V+JR_s)}{nk_BT}} - 1\right) - \frac{V + JR_s}{R_{shunt}} \tag{43}$$

Where J is the current-density, J_L is the photogenerated current density, J_0 is the reverse saturation current density, q is the elementary charge, k_B is the Boltzmann's constant, V is the voltage, n is the ideality factor of solar cell, T is the temperature, R_s is the series resistance, and R_{shunt} is the shunt resistance.

A solar cell which can be represented and modelled using equivalent circuit is shown in Figure 20. An ideal solar can be modelled using a current source in parallel with a diode. Resistances can then be added to the circuit to account for the parasitic losses. The shunt resistance (R_{shunt}) is placed in parallel with the ideal solar cell, while the series resistance R_s is placed in series with the rest of the circuit.

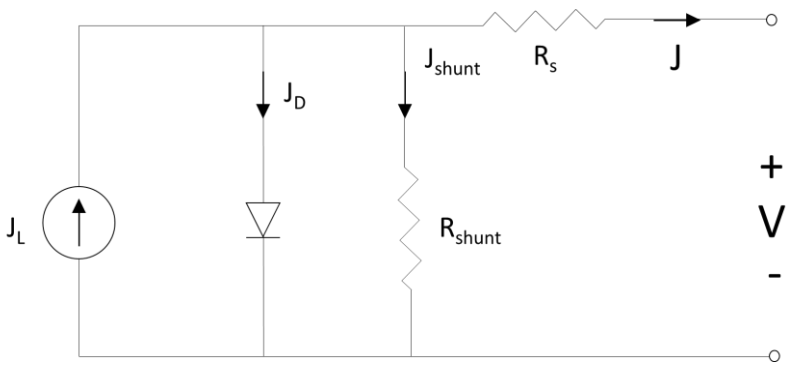


Figure 20: One diode equivalent circuit of a solar cell.

2.2. Organic-Inorganic Halide Perovskite Solar cells

Perovskites are a class of compounds which share the same crystal structure as calcium titanate, $CaTiO_3$. This generic ABX_3 crystal structure is represented in Figure 21. The overall charge of this crystal is neutral. However, this semiconductor compound consists of positively charged ions, cations, and negatively charged ions, anions. Oxide perovskite structures (ABO_3), where A and B-site are cations with +2 and +4 charges to compensate for the three O^{-2}, have been studied for their thermoelectric, ferromagnetic and superconductive properties. Furthermore, fluoride perovskite (ABF_3) have been used for battery applications.[36,37] However, it is only recently that organic-inorganic perovskites have gained attraction for solar cell application. These ABX_3 perovskites employ an organic or inorganic cation with a +1 charge at the A-site, a divalent metal cation with a +2 charge at a B-site, and a halide anion with a -1 charge at the X-site. For an ideal cubic three-dimensional (3D) perovskite structure, the B-site cation is in 6-fold coordination, surrounded by an octahedron of anions, while the A-site cation in 12-fold cuboctahedral coordination.[38]

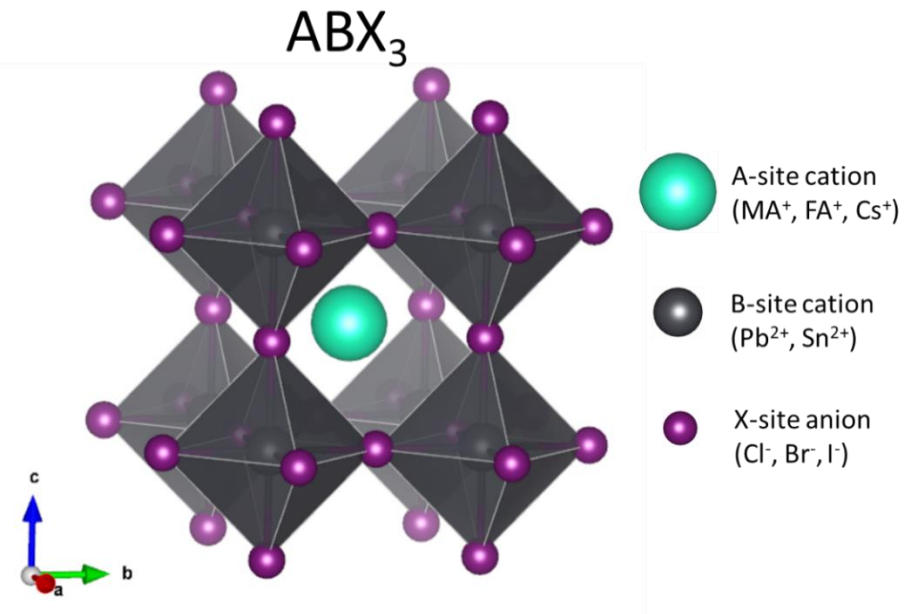


Figure 21: Generic ABX_3 cubic perovskite unit cell, with commonly used A-site, B-site and X-site ions for solar cell application.

For solar cell applications, the A-site cations, commonly used to obtain three-dimensional perovskite structures, are CH_3NH_3, named methylammonium (MA^+), $CH(NH_2)_2$ named formamidinium

(FA^+), and cesium (Cs^+). The B-site is usually composed of either lead (Pb^{2+}) or tin (Sn^{2+}) metal. The X-site is usually a halide anion such as chloride (Cl^-), bromide (Br^-), or iodide (I^-). However, not all ions with the correction charge will necessarily form a 3D perovskite structure. Specific atoms or molecules with an appropriate ionic radius are required to form stable three-dimensional perovskite structures. The Goldschmidt tolerance factor is commonly used to estimate the compatibility of certain ionic sizes to form perovskite structures.[39] The Goldschmidt tolerance factor t is given by:

$$t = \frac{r_A + r_0}{\sqrt{2}(r_B + r_0)} \tag{44}$$

Where r_A is the radius of the A-site cation, r_B is the radius of the B-site cation, and r_0 is the radius of the X-site anion.

In simple terms, the Goldschmidt tolerance factor assess whether the A site cation can fit within the BX_3 framework.[40] If so, it is likely that a stable perovskite arises from the chosen set of molecules or atoms. Surprisingly, non-perfectly ideal perovskites can sometimes still form, however, they do so with a distortion in the crystal lattice, which causes the BX_6 octahedra to tilt. The Goldschmidt tolerance factor t can also help predict the crystal phase of the perovskite. The stable 3D perovskite commonly consists of a corner sharing BX_6 octahedra, which generally occurs for cubic structures, but this corner sharing can also be seen for tetragonal and trigonal crystal structures, such as in the case of $MAPbI_3$ and $FAPbI_3$. It is known that 3D perovskites should form when the tolerance factor falls within a narrow range $t = 0.7 - 1.1$.[39,41,42] However, this simple geometric approach to predicting perovskite structure should also be used with caution. This approach, assumes ions are hard spheres, and hence their radii can be estimated, based on the methodology of Shannon.[43,44] However, in the case of organic-inorganic perovskites, the organic cations are non-spherical, and thus creates ambiguity when defining the A site ionic radius. Furthermore, as Travis et al. explains, heavier halides, such as I^-, have lower electronegativity compared to O^{2-} or F^-, hence the assumption that ions are unpolarizable hard spheres is less valid.[40] Therefore, perovskites that lie within the ideal cubic range may not always form a perovskite using this simple geometric calculation. Predicting the ideal ionic composition that will form the most stable perovskite is not trivial, and is still an ongoing research interest.

Halide-based perovskites materials made their first appearance at the end of the 19th century, when H. L. Wells and H. Topsöe investigated their crystal structure of cesium-based perovskites.[45,46] In 1978, organic-inorganic $CH_3NH_3PbX_3$ and $CH_3NH_3SnX_3$ three-dimensional perovskite were subsequently investigated by D. Weber.[47,48] A researcher at IBM, D. Mitzi, later on demonstrated that organic-inorganic perovskite based materials could be used in light-emitting diodes (LED) applications.[19–21] However, it is only in 2009 that Miyasaka and co-workers first showed their usefulness as a light absorbing material in the dye-sensitized solar cell architecture, reaching 3.8% PCE.[17] In 2012, Snaith and co-workers showed that perovskite could reach 10% PCE using an inert insulating Al_2O_3 scaffold, which demonstrated that perovskite was acting as a semiconductor rather than a sensitizer.[18] This also meant that charge-carrier diffusion lengths were long enough to reach their respective electrodes. Later measurements showed that electron-hole diffusion lengths could exceed $1\ \mu m$ in thin film $MAPbI_3$ perovskite.[49] This long diffusion length allowed for the fabrication of planar p-i-n and n-i-p architectures.

Organic-inorganic perovskites have incredible optoelectronic properties, which have allowed them to dramatically increase their efficiencies over a short time span. A critical property for semiconductors, in particular for solar cell application, is the exciton binding energy, which can vary dramatically from merely a few meV to about 100 meV.[50] The exciton binding energy corresponds to a loss in the maximum chemical potential of the photo-excited electron-hole pair. This energy loss is the difference between the electronic band gap and the optical band gap. Hence, a low exciton binding energy is required to achieve highly efficient solar cells. However, to date, reports for the binding energy for the $MAPbI_3$ range broadly from 2 meV to 55 meV.[51–56] Although there is still ongoing debate concerning the exact value of the binding energy, recent reports suggest that the lower values are more plausible. Another crucial metric is the trap density and diffusion length of the bulk material. Studies have measured surprising low trap densities, in the range of 10^{10} cm^{-3}, for single crystals.[57,58] However, intrinsic ionic movement in perovskite materials may result in a measurement artifact when measuring trap density, since ions can potentially fill trap states under an applied bias. Furthermore, charge-carrier diffusion lengths for single crystals were reported in the range from tens to hundreds of microns.[58,59] Low non-radiative trap-assisted and Auger recombination rates have been reported.[60] Moreover, Urbach energies, a measurement of electronic disorder, have been reported to be as low as 15 meV for the $MAPbI_3$ perovskite.[61] The combination of all of these phenomenal optoelectronic properties has given rise to an incredible research effort investigating perovskite materials for solar cell application.

Another important advantage that perovskite material have is their ability to tune their band gap by simply changing their chemical structure. This attractive feature of the material allows for the band gap to vary from 1.24 to 2.3 eV,[62–65] thus allowing the potential for multi-junction solar cells. However, many hurdles need to be overcome in order to surpass the Shockley-Queisser limit. Firstly, the mixed-halide perovskites tend to form with significantly higher levels of electronic disorder compared to neat halide perovskite systems.[66] This increase in Urbach energy causes the performance and open-circuit voltage to be significantly lower than anticipated, hence nullifying any gains from lower photon thermalization losses when fabricating multi-junction solar cells. Furthermore, mixed-halide perovskites are prone to photo-instability, where segregation occurs, and two neat halide perovskite domains form under illumination.[26] This causes the open-circuit voltage to be pinned by the narrower band gap material. To overcome these fundamental problems, highly crystalline and stable perovskite materials are needed for multi-junction perovskite solar cell applications.

Perovskite solar cells can operate in a planar p-i-n or n-i-p junction architecture, as shown in Figure 22. The perovskite is sandwich between an accepting electron layer and a hole accepting layer, forming a heterojunction n-i-p junction architecture. The electron accepting layer, known as the n-type layer, also acts as a hole blocking layer to prevent recombination at the interface. Similarly, the p-type layer, is selective to holes only and repels electrons at the interface. These electron or hole accepting layer can be fabricated from inorganic compounds such as or organic materials with band gaps greater than the perovskite. Metal oxides, such as TiO_2 and SnO_2, and fullerene derivatives, such as phenyl-C_{61}-butyric acid methyl ester ($PC_{61}BM$) or C_{60}, can serve as electron transporting material (ETM). On the other hand, p-type metal oxides such as NiO and organic molecules, such as 2,2',7,7'-tetrakis-(N,N-di-p-methoxyphenylamine)9,9'-spirobifluorene (spiro-OMeTAD), Poly[bis(4-phenyl)(2,4,6-trimethylphenyl)amine Poly(triarylamine) (PTAA), or Poly(4-butylphenyl-diphenyl-amine) poly-TPD, poly(3-hexylthiophene-2,5-diyl) (P3HT), poly(3,4-ethylenedioxythiophene) polystyrene sulfonate (PEDOT:PSS) are commonly used as hole transporting material (ETM). In order to efficiently extract charges and minimize voltage losses, ETM must be selected in order to align its CB or the lowest energy unoccupied molecular orbital (LUMO) level with the CB of the perovskite, while the HTM must have a VB or the highest energy occupied molecular orbital (HOMO) level that aligns with the VB of the perovskite. These transport layers must provide high conductivity and transparency, with the capability to be produced at a low cost.

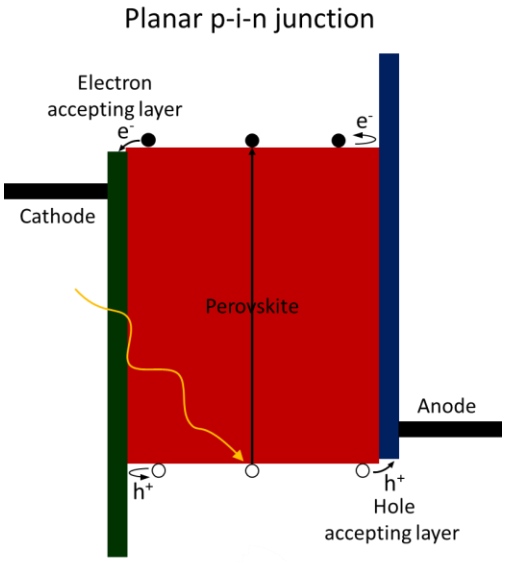


Figure 22: Schematic view of the working principle of p-i-n perovskite solar cell.

2.3. Multi-Junction Solar cells

The theoretical efficiency limit of a single-junction solar cell has been established by Schottky and Queisser dating back to 1961.[24] This limit, also known as the detail balance limit, entails a thermodynamic equilibrium between absorption and emission and makes several assumptions:

1. All photons with energy greater than the band gap are absorbed and create an electron-hole pair.
2. Electron and hole populations relax to band edges, and are in quasi thermal equilibrium with the lattice temperature, resulting in a quasi-Fermi level splitting.
3. Radiative recombination is the only loss mechanism.
4. Carriers have infinite mobilities

This thermodynamic approach, called the detailed balanced, assumes that the sun and the solar cell are acting as blackbodies with temperature of 6000 K and 300 K, respectively. The detailed balance theory can be used to calculate the efficiency limits for every possible band gap. However, there is only one band gap which has the highest possible efficiency. This optimum absorber band gap lies at 1.34 eV, and can theoretically deliver a power conversion efficiency of 33.7 %.[24]

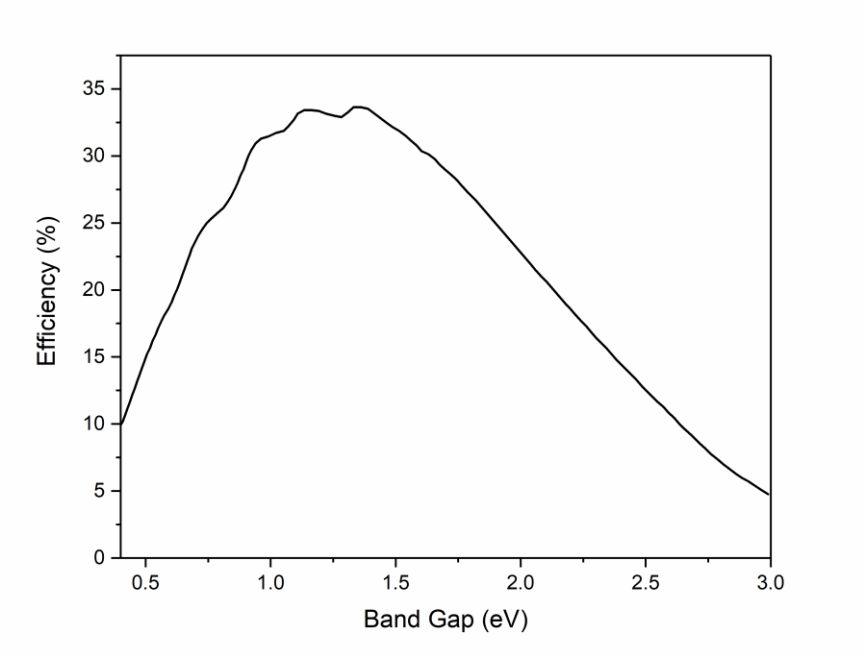


Figure 23: The Shockley-Queisser efficiency limit of an absorber material for various band gaps.

The extension of this detailed-balanced method was proposed by Tiedje-Yablonovitch, which considers free carrier absorption and Auger recombination in addition to radiative losses. Furthermore, an AM1.5 spectrum was used as incident light, instead of the blackbody radiation spectrum. Moreover, instead of assuming the absorption coefficient with a step-function, Tiedje-Yablonovitch employed an absorption coefficient function, including sub-band gap absorption. Hence, taking into account these physical mechanisms result in a more realistic efficiency limit. For c-Si solar cells, the Tiedje-Yablonovitch limiting efficiency is found to be 29.8%.

However, one approach to overcoming the Shockley-Queisser or Tiedje-Yablonovitch limit is to increase the light concentration on the area of the solar cell. The short-circuit current density increases linearly to the light intensity, however, the V_{oc} scales logarithmically to the increase in light intensity. In turn, assuming low parasitic resistances, efficiency gains can be measured for higher solar intensity. Furthermore, another method used for surpassing the Shockley-Queisser limit, lies in the use multiple of absorber layers with different band gaps to absorb photons with different energies. This approach enables absorbed photons to thermalize closer to the band gap energy. This reduction in thermalization losses leads to the improvement in PCE. Ideally, to prevent any thermalization losses, there should be an absorber with a specific band gap for every photon that is absorbed in the incident solar spectrum. By combining these two approaches, a solar cell with an infinity of band gaps measure measured at 1 sun illumination can theoretically achieve 67% PCE, and 88.6 % under infinite suns.

However, in practical application, most commercially available solar cells are limited to only a few junctions, since parasitic optical losses and production costs of every semiconductor layer are considered. The current world record is a wafer bonded four-junction GaInP/GaAs;GaInAsP/GaInAs solar cell which reached 46.0% PCE at 508 suns. In the case of a perovskite/c-Si tandem solar cell, the theoretical efficiency is lower than the world record due to the reduction in junctions, however, lower fabrication costs can outweigh this loss in efficiency. In Figure 24, we show a schematic of the concept of tandem solar cell, using a 1.74 eV perovskite absorber as the wide-band gap material and a silicon absorber as the narrow band gap material.

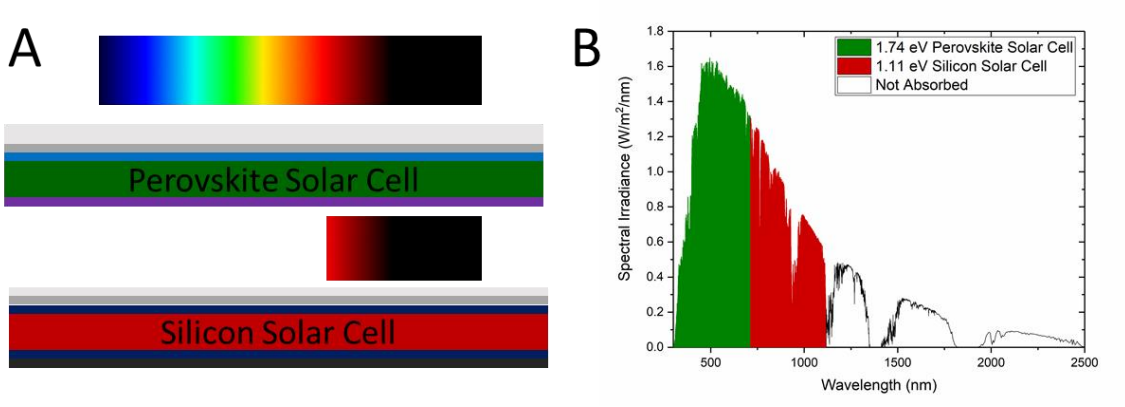


Figure 24: Concept of a perovskite/c-Si tandem solar cell. *A) Schematic of a perovskite solar cell absorbing the high energy photons and the c-Si solar cell absorbing the lower energy photons. B) Wavelength regions of the AM1.5G solar spectrum absorbed for each material.*

Two major architectures are commonly employed for tandem applications: a two-terminal (2T) and four-terminal (4T) architecture, where both of these architectures have their advantages and disadvantages. In Figure 25, we present a schematic for both of these architectures.

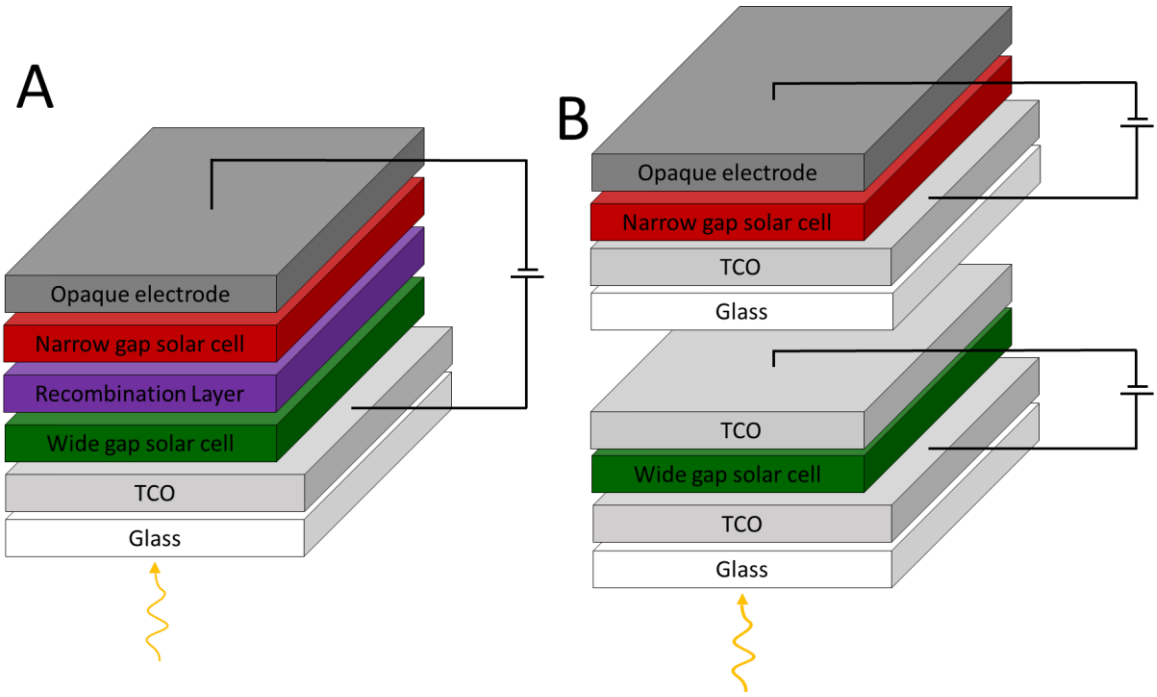


Figure 25: Tandem architectures. *A) Two-terminal and B) Four-terminal tandem solar cell configuration.*

In a two-terminal architecture, the multiple junctions are connected in series and usually mechanically stacked together. This architecture does not require a semi-transparent electrode, which introduces additional optical and electrical losses. Furthermore, this gives the possibility of fabricating the solar cell junctions by sequentially depositing the layers, without fabricating a transparent conductive oxide (TCO) in the middle of the process. However, all the current densities in each sub-cell must be equal, otherwise the entire solar cell will be limited by the lowest current density. This concept of current-matching is critical to fabricating efficient, monolithically stacked tandem solar cells. On the other hand, four-terminal architectures are independently electrically connected, hence, they can generate different currents at their respective junctions. The fact that the 4T tandem architecture does not have current matching as a constraint, allows it to be efficient for a much broader range of band gaps, which results in a slightly higher theoretical efficiency. In Figure 26, we show results obtained by M. Hörantner, where theoretical maximum efficiencies were obtained using a detailed balanced approach, for both 4T and 2T architectures. We notice that the ideal band gap for a top cell absorber is around ~1.75 eV, in order to obtain the optimum efficiency using a 1.11 eV silicon solar cell bottom cell.

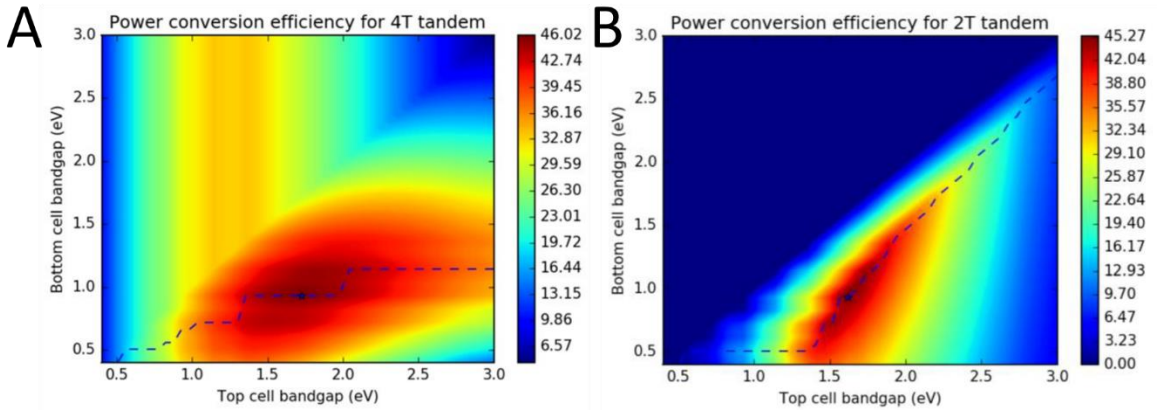


Figure 26: Combined tandem power conversion efficiency for different top cell and bottom cell bandgap combinations *in A) four-terminal and B) two-terminal configurations. (Reproduced with permission from M. Hörantner, Predicting and optimising the energy yield of perovskite-on-silicon tandem solar cells under real world conditions. Energy Environ. Sci.* ***10,*** *1983–1993 (2017))*

3. Experimental Methods

3.1. Substrate preparation

Devices were fabricated on fluorine-doped tin oxide (FTO) coated glass (Pilkington, 7 or 15Ω $\square^{-1}$). Initially, FTO was removed at specific regions where the anode contact will be deposited. This FTO etching was done using a 2M HCl and zinc powder. Substrates were then cleaned with Hellmanex detergent and rinsed with water. Finally, the substrates were then cleaned sequentially in acetone, isopropyl alcohol (IPA), and dried with a compressed air gun.

3.2. Electron transporting layer

The electron accepting layer is composed of a dual layer metal oxide inorganic, followed by an organic layer. The tin-oxide (SnO_2) semiconductor can be deposited by spin coating or by chemical bath deposition (CVD). A subsequent organic layer, namely a phenyl-C_{61}-butyric acid methyl ester ($PC_{61}BM$), is processed on top of the SnO_2 by spin coating.

3.2.1. Solution processed tin-oxide (SnO_2) layer

Prior to deposition, a five-minute oxygen plasma was done to the FTO, in order to remove any organic compounds and to create a hydrophilic surface. Immediately prior to spin coating, we prepared a SnO_2 precursor solution comprised of 17.5mg ml^{-1} tin(IV) chloride pentahydrate ($SnCl_4 \cdot 5H_2O$) (Sigma-Aldrich) dissolved in anhydrous 2-propanol (IPA). The solution was spin-coated in nitrogen at 3000 rpm for 30 s, with a ramp of 200 rpm/s. The substrates were then dried in nitrogen at 100 °C for 10 min. A subsequent annealing step was done in air at 180 °C for 90 min.

3.2.2. Chemical bath deposition (CVD) tin-oxide (SnO_2) layer

Prior to deposition, a five-minute oxygen plasma was done to the FTO, in order to remove any organic compounds and to create a hydrophilic surface. A SnO_2 layer was formed by immersing the cleaned FTO substrate in a bath of 40 mM $SnCl_4$ in aqueous solution for 30 minutes at 80 °C, a variation of the protocol employed by Yong et al.[67] The substrates were immediately rinsed with two consecutive deionized water baths and then sonicated for 10s in an ethanol bath. The substrates were then dried with a nitrogen gun.

3.2.3. Nanoparticles tin oxide (SnO_2) layer

The SnO_2 nanoparticles were synthesized via the hydrothermal method, similar to the method described by Zhang et al[68]. We dissolved 467 mg of $SnCl_4 \cdot 5H_2O$ (98%, Sigma-Aldrich) in 20 ml of deionized (DI) water. After 10 minutes of stirring at room temperature, a fully dissolved, clear solution was obtained. This solution was then transferred to a Teflon-lined stainless-steel autoclave, and heated for 2 hours at 200 °C. After heating treatment, the autoclave was quenched to room temperature using cold water. The precipitates were centrifuged at a speed of 9000 rpm for 15 min. The nanoparticles were re-dispersed in ethanol using a spin-coater. This washing treatment was repeated 3 times. After the final washing treatment, the nanoparticles were also re-dispersed in ethanol. A 2 mg mL^{-1} SnO_2 nanoparticle dispersion in anhydrous ethanol (99.5%, Sigma-Aldrich) was spin coated in air on a clean FTO substrate at 2000 rpm for 45s, and annealed at 150 °C for 60s.

3.2.4. Phenyl-C61-butyric acid methyl ester ($PC_{61}BM$) layer

A Phenyl-C61-butyric acid methyl ester ($PC_{61}BM$) precursor solution was prepared by dissolving a 7.5 mg ml^{-1} $PC_{61}BM$ (99%, solenne) in anhydrous chlorobenzene (CB) (Sigma). We doped the $PC_{61}BM$ using dihydro-1H-benzoimidazol-2-yl (N-DBI) derivatives, specifically 3-dimethyl-2-phenyl-2,3-

dihydro-1H-benzoimidazole (N-DMBI).[69–74] We doped the $PC_{61}BM$ precursor solution with N-DMBI at a 0.25% wt%. This solution was then filtered using a $0.45\ \mu m$ PTFE filter. We spin coated this solution in a nitrogen-filled glovebox at 2000 rpm for 20s with a ramp rate of 1000 rpm/s, and annealed the substrate at 80 °C for 10 min.

3.3. Hole transporting layer

We employed two different 2,2',7,7'-tetrakis-(N,N-di-p-methoxyphenylamine)9,9'-spirobifluorene (spiro-OMeTAD) materials, depending on the perovskite composition used in the device. For lead-based perovskite, we employed spiro-OMeTAD with commonly used dopants: lithium bis(trifluoromethanesulfonyl)imide (Li-TFSI) and 4-tert-Butylpyridine (TBP). We avoided using lithium-based dopants and TBP for tin-based perovskites, to avoid the oxidation period required for Li-TFSI. Instead, we doped spiro-OMeTAD with spiro$(TFSI)_2$ to increase its conductivity.

3.3.1. Spiro-OMeTAD hole-transporting layer

The electron-blocking layer was deposited with a 72.5mg/ml of 2,2',7,7'-tetrakis-(N,N-di-p-methoxyphenylamine)9,9'-spirobifluorene (spiro-OMeTAD) (Lumtec) solution in chlorobenzene. Additives of 38µl of lithium bis(trifluoromethanesulfonyl)imide (170mg/mL in 1-butanol solution) per 1ml of spiro-OMeTAD solution and 21µl of 4-tert-butylpyridine (TBP) per 1mL of spiro-OMeTAD solution. The samples were left to oxidize in a desiccator for 24h. Spin-coating was carried out in a nitrogen-filled glovebox at 2000rpm for 20s with a ramp rate of 1000 rpm/s.

3.3.2. Spiro$(TFSI)_2$ synthesis

The Spiro$(TFSI)_2$ hole-transporting layer used for the $MAPb_{0.75}Sn_{0.25}I_3$ perovskite was prepared using an adapted method described by Nguyen et al.[75] We first dissolved 2,2',7,7'-tetrakis-(N,N-di-p-

methoxyphenylamine)9,9'-spirobifluorene (spiro-OMeTAD) (Lumtec) solution in chlorobenzene (CB) at a 2 mg ml^{-1} concentration. Separately, we dissolved the Silver(I) bis(trifluoromethanesulfonyl)imide (Ag-TFSI) in methanol at a 100 mg ml^{-1}. We slowly mixed identical volumes of both solutions together, while stirring. The final molar ratio is 1 to 0.95 (spiro-OMeTAD to Ag-TFSI). We then left the mixed solution stirring overnight. We filtered the solution with a $0.2\ \mu m$ PTFE filter to remove the Ag colloids. We used a rotary evaporation to remove CB until approximately 5% of the original volume was left. We then added toluene to the remaining flask at a volume of 50% of the initial CB volume. We placed the solution in a refrigerator for 24h, where a fine black powder precipitated. Once the black powder fully settled, we removed excess toluene using a glass frit filter. We washed the powder with a cold 4 °C toluene. Once the powder was dry, we prepared a 20 mg ml^{-1} in methanol solution. This black powder should not have low solubility in methanol, which starts the precipitation process. We refrigerated the solution at 4 °C overnight. The black powder collected at the bottom of the vial. We removed the excess toluene using a glass frit filter, and washed with 4 °C methanol. Once dry, we collected and weighed the Spiro$(TFSI)_2$ powder.

3.3.3. Spiro-OMeTAD doped with 10 wt.% Spiro$(TFSI)_2$ layer

The electron-blocking layer was deposited by dynamically spin coating a spiro$(TFSI)_2$ doped spiro-OMeTAD at 2000 rpm for 30s in a nitrogen glovebox. This precursor solution was prepared with a 72.5 mg ml^{-1} wt.% spiro solution composed of a 7.25 mg ml^{-1} Spiro$(TFSI)_2$ and a 65.25 mg ml^{-1} 2,2',7,7'-tetrakis-(N,N-di-p-methoxyphenylamine)9,9'-spirobifluorene (spiro-OMeTAD) (Lumtec) solution in chlorobenzene. No additives were added to the spiro-OMeTAD solution.

3.4. Tandem recombination interlayer layer

The interlayer was fabricated using both PEDOT:PSS (PH 1000) dispersed in water (Heraeus Clevios) and indium-tin oxide, 30 wt. % in isopropanol (IPA), (ITO) >100nm nanoparticles (NPs) dispersion (Sigma), as precursor solutions.

3.4.1. PEDOT:PSS layer

We first deposited a thin layer of PEDOT:PSS directly on top of the existing spiro-OMeTAD layer. The PEDOT:PSS precursor solution was prepared immediately prior to spin coating by diluting PEDOT:PSS (PH 1000) in anhydrous 2-propanol (IPA) at a volume ratio of 1 to 1.5 (PEDOT:PSS to IPA) and then filtered with a 2.7 μm GF/D membrane filter (Whatman). The substrates were preheated at 80 °C, and we then dynamically spin coated the diluted PEDOT:PSS solution in a dry air atmosphere >10% relative humidity (RHM), at a speed of 6000 rpm for 20 s, and then annealed at 80 °C for 10 min.

3.4.2. Indium-tin-oxide (ITO) layer

We then deposited the ITO NPs layer. We prepared the ITO NPs precursor solution by diluting the 30 wt. % in IPA down to 1 wt. % in IPA. The diluted solution was sonicated, in a sonication bath, for 15 m prior to deposition. We dynamically spin coated the diluted ITO NPs solution in a dry air atmosphere >10% relative humidity (RHM), at a speed of 6000 rpm for 20 s, and then annealed at 80 °C for 10 m.

3.4.3. Phenyl-C61-butyric acid methyl ester ($PC_{61}BM$) layer in multi-junctions

A Phenyl-C61-butyric acid methyl ester ($PC_{61}BM$) precursor solution was prepared by dissolving a 30 mg ml^{-1} $PC_{61}BM$ (99%, solenne) in a mixture of anhydrous chlorobenzene (CB) (sigma) and anhydrous chloroform (CF) solvents. The solvents were mixed at a volume ratio of 2 to 1, CB to CF. We doped the $PC_{61}BM$ using dihydro-1H-benzoimidazol-2-yl (N-DBI) derivatives, specifically 3-dimethyl-2-phenyl-2,3-dihydro-1H-benzoimidazole (N-DMBI).[69–74] We doped the $PC_{61}BM$ precursor solution with N-DMBI at a 0.25 wt%. This solution was then filtered using a $0.45\ \mu m$ PTFE filter. The substrates were preheated at 80 °C, we then dynamically spin coated this solution in a dry air atmosphere >10% relative humidity (RHM) at 4000 rpm for 20s, and annealed the substrate at 80 °C for 10 min.

3.5. Perovskite layer preparation

The perovskite material is prepared using two main deposition routes. The $FA_{(1-x)}Cs_xPb(I_{(1-y)}Br_y)_3$ perovskite is prepared using an acid processing route, which relies on hydrohalic acids (HI/HBr) to remove the colloids inherently present in the precursor solution, allowing us to fully solubilized all the salts and work with full solutions. In turn, this allows for the slow growth of the perovskite, which results in the fabrication of highly crystalline perovskite material with micron size grains. We found that this method increases the overall thermal and light stability of the material. We further discuss this topic in chapter 5. The other route relies on an acetonitrile/methylamine (ACN/MA) solvent system. This highly volatile deposition technique allows for the sequential deposition of perovskite layers on top of one another. This perovskite deposition technique was used for tandem applications.

3.5.1. $FA_{0.83}Cs_{0.17}Pb(I_{0.8}Br_{0.2})_3$ and $FA_{0.83}Cs_{0.17}Pb(I_{0.6}Br_{0.4})_3$ perovskite

The $FA_{0.83}Cs_{0.17}Pb(I_{0.3}Br_{0.7})_3$ with 2% K additive perovskite solutions were prepared by dissolving the precursor salts in anhydrous N,N-dimethylformamide (DMF) to obtain a stoichiometric solution with the desired $FA_{0.83}Cs_{0.17}Pb(Br_{0.7}I_{0.3})_3$ composition and 2% K additive using a molar ratio of 30% to 70% KI to KBr. The precursor solution was prepared using the following precursor salts: formamidinium iodide (FAI), cesium iodide (CsI) (99.9%, Alfa Aesar), lead iodide (PbI_2) (99%, Sigma-Aldrich), lead bromide ($PbBr_2$) (98%, Alfa Aesar), potassium iodide (KI) (99%, Sigma-Aldrich), and potassium bromide (99%, KBr) (Sigma-Aldrich). 27.2 µl/ml of hydroiodic acid (HI) (57 wt. % in H_2O, distilled, stabilized, 99.95%, Sigma-Aldrich) and 54.8 µl/ml of hydrobromic (HBr) (48 wt. % in H_2O) were added to 1ml of 0.75 M precursor solutions. After the addition of the acids, the perovskite precursor solution was aged for 2 days under a nitrogen atmosphere. This aged precursor perovskite solution was spin-coated in a nitrogen-filled glovebox at 2000 rpm for 45s with a 1000 rpm/s ramp rate. The films were dried inside a N_2 glovebox on a hot plate at a temperature of 70 °C for 1 minute. The films were then annealed in an oven in an air atmosphere at 185°C for 90 minutes. During this annealing process, the samples were covered with a large glass container to prevent dust contamination.

3.5.2. $FA_{0.83}Cs_{0.17}Pb(I_{0.3}Br_{0.7})_3$ perovskite with 2% potassium

The $FA_{0.83}Cs_{0.17}Pb(I_{0.3}Br_{0.7})_3$ with 2% K additive perovskite solutions were prepared by dissolving the precursor salts in anhydrous N,N-dimethylformamide (DMF) to obtain a stoichiometric solution with the desired $FA_{0.83}Cs_{0.17}Pb(Br_{0.7}I_{0.3})_3$ composition and 2% K additive using a molar ratio of 30% to 70% KI to KBr. The precursor solution was prepared using the following precursor salts: formamidinium iodide (FAI), cesium iodide (CsI) (99.9%, Alfa Aesar), lead iodide (PbI_2) (99%, Sigma-Aldrich), lead bromide ($PbBr_2$) (98%, Alfa Aesar), potassium iodide (KI) (99%, Sigma-Aldrich), and potassium bromide (99%, KBr) (Sigma-Aldrich). 27.2 µl/ml of hydroiodic acid (HI) (57 wt. % in H_2O, distilled, stabilized, 99.95%, Sigma-Aldrich) and 54.8 µl/ml of hydrobromic (HBr) (48 wt. % in H_2O) were added to 1ml of 0.75 M precursor solutions. After the addition of the acids, the perovskite precursor solution was aged for 2 days under a nitrogen atmosphere. This aged precursor perovskite solution was spin-coated in a nitrogen-filled glovebox at 1200 rpm for 45s with a 600 rpm/s ramp rate. The films were dried inside a N_2 glovebox on a hot plate at a temperature of 70 °C for 1 minute. The films were then annealed in an oven in an air atmosphere at 185°C for 90 minutes. During this annealing process, the samples were covered with a large glass container to prevent dust contamination.

3.5.3. ACN/MA $MAPbI_3$ perovskite

In this work, we found that controlling the MA content in the acetonitrile(CH_3CN)/methylamine(CH_3NH_2) (ACN/MA) $MAPbI_3$ solution resulted in better tandem performance with higher reproducibility. Excess MA in the ACN/MA $MAPbI_3$ solution can potentially percolate through pinholes of thin imperfect interlayers, thus partially or completely dissolving the underlying junction. Thus, solutions with the minimal amount of MA required to dissolve the perovskite were employed. Controlling the MA content in the solution can potentially be done by controlling the MA flow rate and stirring speed, however, precisely controlling these parameters was sometimes challenging. Instead, we prepared two ACN $MAPbI_3$ dispersions, one with excess MA content resulting in a full ACN/MA $MAPbI_3$ solution, and another ACN $MAPbI_3$ dispersion without any MA. Immediately prior to spin coating, we slowly added the ACN/MA $MAPbI_3$ with excess MA to the ACN $MAPbI_3$ dispersion until this dispersion was fully dissolved, and became a full solution. The resulting solution is an ACN/MA $MAPbI_3$ solution at its critical solubility point. The preparations of the ACN/MA $MAPbI_3$ solution and the ACN $MAPbI_3$ dispersion are described below.

The ACN $MAPbI_3$ perovskite precursor solution without any MA was prepared, under nitrogen, using precursor salts methylammonium iodide (MAI) (Dyesol) and lead iodide (PbI_2) (TCI) added into

anhydrous acetonitrile (ACN) (Sigma Aldrich) at a concentration of 1.03 M for MAI and 1 M for PbI_2, resulting in a non-stoichiometric solution (1.03:1 MAI:PbI_2). This solution was then sonicated, in a sonication bath, for 1 h in order to fully react the MAI with the PbI_2, a black perovskite dispersion is then seen at the bottom of the ACN filled vial.

The ACN/MA $MAPbI_3$ perovskite precursor solution was prepared using an adapted method described by Noel et al.[76] We first prepared an ACN/MA $MAPbI_3$ perovskite precursor solution with the identical preparation method as described above. In order to dissolve the perovskite in ACN, a solution of methylamine (MA) in ethanol (Sigma Aldrich, 33 wt%) was placed into an aerator which was kept in an ice bath. Nitrogen was then bubbled into the solution, thus degassing the solution of MA. The MA gas which was produced was then passed through a drying tube filled with a desiccant (Drietire and CaO). The gas was bubbled into the black dispersion, while vigorously stirring the ACN/MA $MAPbI_3$ dispersion using a large magnetic stir bar at a speed of approximately 700 rpm. The dispersion was bubbled for 15 minutes, which resulted in a full dissolution of the black perovskite particles, resulting in a clear, light yellow solution. We note this solution has an "excess" amount of MA in the ACN/MA $MAPbI_3$ solution.

The ACN/MA $MAPbI_3$ precursor perovskite solution (at it's critical solubility point) is immediately dynamically spin coated in a dry air atmosphere >10% relative humidity (RHM) at 5000 rpm for 20s. A post treatment of methylammonium chloride (MACl) was then carried out by dynamically spincoating at 6000 rpm for 20s a 50 µl of MACl (Alfa Aesar, 2 mg/ml in isopropanol). The films were then annealed in an oven in an air atmosphere at 80°C for 90 minutes. During this annealing process, the samples were covered with a large glass container to prevent dust contamination.

3.5.4. ACN/MA $MAPb_{0.75}Sn_{0.25}I_3$ perovskite

To obtain a mixed-metal ACN/MA $MAPb_{0.75}Sn_{0.25}I_3$ perovskite precursor solution, we mixed an ACN/MA $MAPbI_3$ with an ACN/MA $MAPb_{0.5}Sn_{0.5}I_3$ (without any MA) at a 1:1 volume ratio, resulting in an ACN/MA $MAPb_{0.75}Sn_{0.25}I_3$.

The ACN/MA $MAPb_{0.5}Sn_{0.5}I_3$ solution perovskite precursor solution without any MA was prepared, under nitrogen, using precursor salts methylammonium iodide (MAI) (Dyesol), lead iodide (PbI_2) (TCI), and anhydrous tin iodide (SnI_2) beads (TCI) added into anhydrous acetonitrile (ACN) (Sigma Aldrich) at a concentration of 0.8 M for MAI, 0.46 M for PbI_2 and 0.46 M for SnI_2, resulting in a non-stoichiometric solution with 15% excess metal salts (1:1.15 MAI:PbI_2+SnI_2). This solution was then

stirred under nitrogen at 70 °C for 1h, in order to fully react the MAI with the mixed metals, a black perovskite dispersion is then seen at the bottom of the ACN filled vial.

The ACN/MA $MAPbI_3$ perovskite precursor solution was prepared using an adapted method described by Noel et al.[76] We first prepared a ACN/MA $MAPbI_3$ perovskite precursor solution at a 0.8 M for MAI and 0.92 M for PbI_2, resulting in a non-stoichiometric solution with 15% excess metal salts (1:1.15 MAI:PbI_2). In order to dissolve the perovskite in ACN, a solution of methylamine (MA) in ethanol H_2O (Sigma Aldrich, 40 wt%) was placed into an aerator which was kept in an ice bath. Nitrogen was then bubbled into the solution, thus degassing the solution of MA. The MA gas which was produced was then passed through a drying tube filled with a desiccant (Drietire and CaO). The gas was bubbled into the black dispersion, while vigorously stirring the ACN/MA $MAPbI_3$ dispersion using a large magnetic stir bar at a speed of approximately 700 rpm. The dispersion was bubbled for 15 minutes, which resulted in a full dissolution of the black perovskite particles, resulting in a clear, light yellow solution. We note this solution has an "excess" amount of MA in the ACN/MA $MAPbI_3$ solution. The solution was then stored in nitrogen for approximately 3 h with activated 3 Å molecular sieves to remove any H_2O that was introduced during the MA bubbling process.

This precursor perovskite solution is immediately dynamically spin coated in a nitrogen glovebox at 5000 rpm for 20s. A second subsequent spin coating step was used to deposit a methylammonium chloride (MACl) post treatment. A 2 mg ml^{-1} solution of MACl in IPA was dynamically spin coated at 6000rpm for 20s. The films were then annealed in nitrogen at 80°C for 90 minutes.

3.6. Metal electrode

A 100 nm silver or gold electrode was thermally evaporated under vacuum of ≈10^{-6} Torr, at a rate of ≈0.2 nm s^{-1}.

3.7. Metal electrode

A thin layer of ITO (Indium Tin Oxide) nanoparticles (<100nm), from ITO dispersion in isopropanol, was spin coated on hole transport layer as the buffer layer to protect the spiro-OMeTAD during ITO sputtering. Then, a ~120-nm thick layer of ITO was sputter coated on the buffer layer using a PVD 75 Kurt J. Lesker.

3.8. Solar cell characterization

The current density–voltage (J-V) curves were measured (2400 Series SourceMeter, Keithley Instruments) under simulated AM 1.5 sunlight at 100 $mWcm^{-2}$ irradiance generated by an Abet Class AAB sun 2000 simulator, with the intensity calibrated with an NREL calibrated KG5 filtered Si reference cell. For single junctions, the mismatch factor was calculated to be less than 1%. For multi-junctions, the mismatch factor was calculated for each junction and PCE were adjusted accordingly. The active area of the solar cell is 0.0919 cm^{-2}. The forward J–V scans were measured from forward bias (FB) to short circuit (SC) and the backward scans were from short circuit to forward bias, both at a scan rate of 0.25V s^{-1}. A stabilization time of 5 seconds under 1 sun illumination and forward bias of 0.3V above the expected V_{oc} was done prior to scanning.

3.9. External quantum efficiency (EQE) characterization

The multi-junction EQEs were measured by optically biasing the sub-cells that are not being measured with a 3W 470-475 nm LED and a 3W 730-740 nm LED, for the TC and for the BC, respectively. A negative bias equal to V_{oc} of the sub-junction that is being optically biased was applied to the tandem during the measurement. This allows us to measure the response of the tandem in short-circuit condition.

3.10. Transient photoconductivity

The Nd:YAG laser excitation source tuned to 470 nm and pumped at 10 Hz with 7 ns pulses was used at the range of fluences to have various charge carrier density, as described in the main text. This pulse light was illuminated in entire sample area to evenly excite the film. A bias of 24 V was applied across the in-plane (lateral) electrodes. Here, as the contact resistance between perovskite film and Au electrode is fairly small compared to sample resistance, we employed two electrodes conductivity measurement. A variable resistance was placed in series with sample. The resistance is

set to be less than 1 % of the sample resistance. We monitored the voltage drop on variable series resistor through parallel oscilloscope (1MΩ) to determine the potential dropped across the two in-plane Au electrodes (4mm channel to channel distance) in the sample. Perovskite film is scribed to have 5mm channel width, and coated with inert 200nm PMMA. Transient photoconductivity ($\sigma_{\text{Transient-Photo}}$) was calculated by the equation, $\sigma_{Ph} = \frac{\Delta V_{Osc}}{R_r \times (V_{bias} - V_{Osc})} \times \frac{l}{w \times t}$ where, R_r is variable resistor, V_{bias} is bias voltage, *l* is channel-channel length, *w* is channel width, and *t* is film thickness.

3.11. Optical Modelling

3.11.1. Overview

We modelled the optical properties of the stack using a generalized transfer matrix method (TMM).[77] All the calculations were done in Python with heavy use of the NumPy and SciPy libraries. The wavelength dependent complex refractive index, the layer thicknesses and the incidence angle were fed as input.

The TMM model outputs the electric field distribution in the stack. This was used to calculate Transmittance $T(E)$, Reflectance $R(E)$ and the absorption $A(E)$ in each layer. The short circuit current of each sub-cell was then determined by assuming the internal quantum efficiency to be unity:

$$J_{SC} = q \int_0^{\infty} A(E) \cdot \phi_{AM1.5}(E) \cdot dE \tag{45}$$

Here, $\phi_{AM1.5}(E)$ is the photon flux from the AM1.5 spectrum.

The JV curve from each sub-cell was obtained by combining this modelled J_{SC} with the electrical characteristics of state-of-art single junction cells. To do this, we parametrized the JV curves of state-of-the-art single junctions as per the single diode equivalent model:

$$J(V) = J_{sun} - J_0\left(e^{\frac{V+J(V)R_S}{nV_T}} - 1\right) - \frac{V + J(V)R_S}{R_{SH}} \quad (46)$$

Where $n, V_T, R_S, J_0\ and\ R_{SH}$ are respectively the electron charge, thermal voltage at 300K, series resistance, dark current, and shunt resistance. The JV curve of each multi-junction sub-cell is modelled by replacing J_{sun} in the fitted equation with the J_{SC} calculated from the multijunction stack. As the correlation between J_{sun} and other fitting parameters is negligible, we can be sure that J_{sun} can be changed without changing other parameters. The approach of Jain et al.[78] was used to solve the single diode model using the Lambert W function. After calculating the JV curves of all sub-cells, we combined them to obtain the multi-junction JV curve.[79] The maximum point is calculated from this combined JV curve.

3.11.2. Inputs for the Optical and Electrical Models

The refractive indices for ITO[80], FTO[81], PEDOT:PSS[59], PCBM[82], Spiro-OMeTAD[83], Ag[84], $MA_{0.4}FA_{0.6}Sn_{0.6}Pb_{0.4}I_3$[85] and $MAPbI_3$[86] were taken from the literature. The extinction co-efficient k of $FA_{0.83}Cs_{0.17}Pb(Br_{0.7}I_{0.3})_3$ was obtained by measuring the transmittance T and the reflectance R of a thin film of thickness t on glass and using the relations:

$$\alpha = \frac{4\pi k}{\lambda} \quad (47)$$

$$\frac{T}{1-R} = e^{\alpha t} \quad (48)$$

Once $k(\lambda)$ was obtained, we parametrized it in terms of Lorentz oscillators to get an analytical representation, which was transformed into the refractive index $n(\lambda)$ via the Kramers-Kronig transform:

$$n(\lambda) = 1 + \frac{2}{\pi}\int_0^\infty \frac{E'k(E)}{E'^2 - E^2}\,dE' \quad (49)$$

The electrical characteristics for the $MAPbI_3$ [87]and the $MAPb_{0.75}Sn_{0.25}I_3$[88] are taken from best reported cells of same or similar class in the literature. For the $FA_{0.83}Cs_{0.17}Pb(Br_{0.7}I_{0.3})_3$ sub-cell, we use the JV curve of our best $FA_{0.83}Cs_{0.17}Pb(Br_{0.7}I_{0.3})_3$ single junction cell.

To account for the ITO nanoparticles being embedded in PCBM, we model its refractive index as a Bruggeman Effective Medium with 75% ITO and 25% PCBM. The refractive index of this effective medium is calculated by solving:

$$\frac{f_{ITO}(n_{ITO}^2 - n^2)}{(n_{ITO}^2 + 2n^2)} = \frac{(1 - f_{FTO})(n_{PCBM}^2 - n^2)}{(n_{PCBM}^2 + 2n^2)} \quad (50)$$

Where n_{ITO}, n_{PCBM} and f_{ITO} are respectively the complex refractive index of ITO, complex refractive index of PCBM and the fraction of ITO in the effective medium.

3.11.3. $FA_{0.83}Cs_{0.17}Pb(Br_{0.7}I_{0.3})_3/MAPbI_3$Tandem Simulation

The thicknesses used in the optical model are obtained from an SEM cross section of the tandem. The electrical characteristics of $FA_{0.83}Cs_{0.17}Pb(Br_{0.7}I_{0.3})_3$ and $MAPbI_3$ presented are extracted from our own single junction devices. The dotted JV models the performance assuming the $MAPbI_3$ performs as well as the best ACN processed $MAPbI_3$ cell in literature.

Layer	**Thickness**
Glass	2.2mm
ITO	350nm
SnO_2	40nm
PCBM	10nm
$FA_{0.83}Cs_{0.17}Pb(Br_{0.7}I_{0.3})_3$	350nm
Spiro-OMeTAD	250nm

PEDOT:PSS	50nm
ITO Nanoparticles:PCBM 75:25 Effective Medium	50nm
PCBM	80nm
$MAPbI_3$	530nm
Spiro-OMeTAD	180nm
Ag	100nm

3.11.4. $FA_{0.83}Cs_{0.17}Pb(Br_{0.7}I_{0.3})_3/MAPbI_3$ tandem simulation (optimized)

We cap the thicknesses of the non-perovskite layers at 50nm. We add a MgF_2 anti-reflecting coating. We optimize the thicknesses of the perovskite layers and the anti-reflecting coating using a differential evolution algorithm to maximize the limiting current.

The electrical characteristics of the $FA_{0.83}Cs_{0.17}Pb(Br_{0.7}I_{0.3})_3$ are from our own device (Fig S3). The characteristics of the $MAPbI_3$ are from the best cell $MAPbI_3$ in literature.[89] The dotted JV curve models the performance of the tandem- assuming the top cell electrically performs as well as current state-of-the-art in Perovskites. We follow the approach of Hörantner et al [85] for this, and assume $EQE_{EL} = 0.01$, $R_S = 4 \cdot 10^{-2}\ \Omega\, cm^2$ and $R_{SH} = 10M\Omega\, cm^2$.

Layer	Thickness
MgF_2	Search space: 10-500nm Optimized: 104nm
Glass	2.2mm
FTO	50nm
SnO_2	40nm
PCBM	10nm
$FA_{0.83}Cs_{0.17}Pb(Br_{0.7}I_{0.3})_3$	Search space: 100-1500nm Optimized: 381nm

Spiro-OMeTAD	50nm
PEDOT:PSS	50nm
ITO Nanoparticles: PCBM 75:25 Effective Medium	50nm
PCBM	50nm
$MAPbI_3$	Search space: 100-1500nm Optimized: 1382nm
Spiro-OMeTAD	50nm
Ag	100nm

3.11.5. $FA_{0.83}Cs_{0.17}Pb(Br_{0.7}I_{0.3})_3/MAPbI_3/MA_{0.4}FA_{0.6}Pb_{0.4}Sn_{0.6}I_3$ triple-junction simulation (optimized)

The calculations for the triple-junction solar cell are performed exactly as for the tandem solar cell. For the dotted triple junction JV curve, where the top cell has been enhanced, both the bottom and top cells are modelled as current state-of-the-art perovskite cells.

Layer	**Thickness**
MgF_2	Search space: 10-500nm Optimized: 92.8nm
Glass	2.2mm
FTO	50nm
SnO_2	40nm
PCBM	10nm
$FA_{0.83}Cs_{0.17}Pb(Br_{0.7}I_{0.3})_3$	Search space: 100-1500nm Optimized: 296.7nm
Spiro-OMeTAD	50nm
PEDOT:PSS	15nm

ITO Nanoparticles:PCBM 75:25 Effective Medium	50nm
PCBM	50nmnm
$MAPbI_3$	Search space: 100-1500nm Optimized: 583.3
Spiro-OMeTAD	50nm
PEDOT:PSS	15nm
ITO Nanoparticles:PCBM 75:25 Effective Medium	50nm
PCBM	50nm
$MA_{0.4}FA_{0.6}Pb_{0.4}Sn_{0.6}I_3$	Search space: 100-1500nm Optimized: 1382.4
Spiro-OMeTAD	50nm
Ag	100nm

3.12. Williamson-Hall method for microstrain estimation

Broadening and shifts in the XRD peak can be caused by either a reduction in the grain size (Scherrer broadening) and/or non-uniform strain (microstrain). We note that Scherrer broadening will only be significant when the grains are in the range of, or less than 100 nm, and as we will discuss later, we do not expect this to be a significant contribution here. Strain is the relative change in size of an object with respect to its ideal size (or size before experiencing an external force). The microstrain in a crystalline material is a result of small fluctuations in the lattice spacing, induced by crystal imperfections/structural defects including dislocations, vacancies, stacking faults, interstitials, twinning, and grain boundaries.[90,91,92] By simply considering Braggs law for scattering of light of wavelength λ, $n\lambda = 2d\sin\theta$, it is clear that small fluctuations in d spacing (i.e. Δd) will result in small

fluctuations, or broadening, in θ when measuring the X-ray diffraction from the material. We quantify the extent of microstrain in our perovskite crystals by analysing the peak broadening in the diffraction patterns according to the modified Williamson-Hall method.[91,93] The effective observed d-space broadening (Δd_{obs}) determined from the XRD peak width broadening, is a convoluted function of the Gaussian full width half maximum broadening in the 2θ scan due to the instrument response (Δd_{ins}), the grain size (Δd_{size}) and the microstrain (Δd_{ε}). These can be de-convoluted from the observed broadening, via,

$$\Delta d_{obs}^2 = \Delta d_{\varepsilon}^2 + \Delta d_{in\varepsilon}^2 + \Delta d_{size}^2 \quad (51)$$

where the unit-less microstrain ε is defined as $\varepsilon = (\Delta d_{\varepsilon}/d)$, where d is the mean d-spacing.

For single crystals, the size effect induced peak width broadening can be neglected, hence if $\Delta d^2_{size} << \Delta d^2_{obs}$ [19] - we can write,

$$(\Delta d_{obs}^2 - \Delta d_{in\varepsilon}^2)^{1/2} \approx \varepsilon d \quad (52)$$

Therefore, the slope of $(\Delta d_{obs}^2 - \Delta d_{in\varepsilon}^2)^{1/2}$ versus d gives the magnitude of the microstrain, ε, in the crystals.

3.13. X-ray diffraction measurement

3.13.1. One-dimensional X-ray diffraction

X-ray diffraction pattern were obtained using a Panalytical X'Pert Pro x-ray diffractometer, using the copper K-alpha wavelength of 0.154nm. All the perovskite films for XRD measurement were deposited on FTO coated glass substrates.

3.13.2. Two-dimensional X-ray diffraction

The two-dimensional X-ray diffraction pattern were measured using a Rigaku SmartLab X-ray diffractometer with $CuK_{\alpha 1}$ (1.54060 Å) and a HyPix-3000 2D hybrid pixel array detector. All the perovskite films for XRD measurement were deposited on FTO coated glass substrates.

3.14. X-ray diffraction measurement

The dynamic light scattering (DLS) was measured using a Malvern Zetasizer Nano ZS. The measurement was done with a quartz cuvette at room temperature.

3.15. Terahertz (THz) probe spectroscopy

3.15.1. Optical pump

The optical-pump-THz-probe setup uses a Spectra Physics Ti:Sapphire regenerative amplifier to generate 40 fs pulses at a center wavelength of 800 nm and a repetition rate of 1.1 kHz. Terahertz pulses were generated by optical rectification in a 450 µm thick GaP(110) single crystal and detected by electro-optic sampling in a ZnTe crystal (0.2 mm (110)-ZnTe on 3 mm (100)-ZnTe). Pulses for optical excitation of the samples at 400 nm were generated using a beta barium borat frequency doubling crystal. Optical excitation was carried out from the substrate side of the film. The diameters of optical pump and THz probe beams at the sample position were 3.6 mm and 2.4 mm (FWHM), respectively.

Measurements were performed with the entire THz beam path (including emitter, detector and sample) in an evacuated chamber at a pressure of $<10^{-2}$ bar.

3.15.2. Derivation of photoconductivity and charge carrier mobility from change in THz electric field transmission

Assuming the thickness of the perovskite film is smaller than the THz wavelength, the sheet photoconductivity ΔS of a thin film between two media of refractive indices n_a and n_b can be expressed as:

$$\Delta S \approx -\varepsilon_0 c\,(n_a + n_b)\frac{\Delta T}{T} \tag{53}$$

Where, the product $\varepsilon_0\, c$ denotes the invert of the vacuum impedance and $\Delta T/T$ the photoinduced change in THz electric field transmission over total transmission. As the experiment was performed in an evacuated box under vacuum, the films are surrounded by vacuum from one side (n_b = 1) and in direct contact with the z-cut quartz substrate from the other side (n_a = 2.13), through which the photoexcitation of the sample occurs.

The charge-carrier mobility μ can be calculated as follows:

$$\mu \approx \frac{\Delta S\, A_{eff}}{N\, e} \tag{54}$$

where ΔS is the sheet photoconductivity of a thin film, e is the elementary charge and N is the number of photoexcited charge-carriers. A_{eff} is the effective area of the overlap of optical pump and THz probe pulse calculated as follows:

$$A_{eff} = \frac{\pi}{\ln(2)}\,(FWHM_{pump}^2 + FWHM_{probe}^2) \tag{55}$$

The number of photoexcited charge-carriers N can be determined as follows:

$$N = \varphi \frac{E\lambda}{hc} (1 - R_{pump}) (1 - T_{pump}) \quad (56)$$

where φ is the ratio of charge-carriers produced following photon absorption, also known as the photon-to-charge branching ratio, which is assumed to be unity. *E* is the energy contained in an optical excitation pulse of wavelength λ, R_{pump} is the reflectivity of the sample at normal incidence of the excitation beam, and T_{pump} denotes the portion of pump beam which is transmitted through the sample. As φ is declared unknown, we define an effective mobility $\tilde{\mu} = \varphi\mu$ which can be directly obtained from our experiments:

$$\varphi\mu = -\varepsilon_0 c (n_a + n_b) \frac{A_{eff}\, hc}{E\, e\, \lambda (1 - R_{pump}) (1 - T_{pump})} \frac{\Delta T}{T} \quad (57)$$

The ascertained charge-carrier mobility contains contributions from both electrons and holes. Hence, the derived values for mobility represent the sum of electron and hole mobilities. As φ ranges between 0 and 1, the effective mobility describes a lower limit.

Furthermore, the effective carrier mobilities have been corrected by scaling the onset value of $\frac{\Delta T}{T}$ with the relative surface coverage of the respective films, which were obtained by processing SEM images. The surface coverage procedure satisfies our requirement to account for actual effective carrier mobilities in the films as we rule out any excess absorption in possibly thicker films. Due to high absorption coefficients, most of the light is being absorbed within the first hundreds of nanometers, for which reason a thickness correction is not required, especially since the thickness of all measured films exceeds 400 nm.

4. A formamidinium-cesium mixed-cation lead mixed-halide perovskite for tandem solar cells applications

The work in this chapter has been adapted and reproduced in part with permission from:

David P. McMeekin, Golnaz Sadoughi, Waqaas Rehman, Giles E. Eperon, Michael Saliba, Maximilian T. Hörantner, Amir Haghighirad, Nobuya Sakai, Lars Korte, Bernd Rech, Michael B. Johnston, Laura M. Herz, Henry J. Snaith, A mixed-cation lead mixed-halide perovskite absorber for tandem solar cells, *Science* 351**,** 151–155 (2016). Copyright 2016 Science.

4.1. Context and summary

Metal halide perovskite photovoltaic cells could potentially boost the efficiency of commercial silicon photovoltaic modules from ~20 toward 30% when used in tandem architectures. An optimum perovskite cell optical band gap of ~1.75 electron volts (eV), can be achieved by varying halide composition but to date, such materials have had poor photostability and thermal stability. Therefore, the commonly used $MAPb(I_{(1-x)}Br_x)_3$ perovskite system has failed to deliver low-voltage losses for mixed-halide compositions, which limit the performance gains expected for tandem solar cells. Inn this chapter, we present a highly crystalline and compositionally photostable material, $[HC(NH_2)_2]_{0.83}Cs_{0.17}Pb(I_{0.6}Br_{0.4})_3$ with an optical band gap of ~1.74eV, and fabricate perovskite cells which reach open-circuit voltages of 1.2 V and power conversion efficiency of over 16% (stabilized). By combining a crystalline silicon cell with a $[HC(NH_2)_2]_{0.83}Cs_{0.17}Pb(I_{0.6}Br_{0.4})_3$ perovskite with a semi-transparent electrode, we could achieve a PCE of 22.4% (19.8% stabilized) using a four-terminal perovskite/c-Si tandem architecture.

4.2. Introduction

One concept for improving the efficiency of photovoltaics (PVs) is to create a tandem junction, for example, by placing a wide band gap top cell (TC) above a silicon bottom cell (BC). Given the crystalline silicon (c-Si) band gap of 1.1 eV, the top cell material requires a band gap of ~1.75 eV, in order to current-match both junctions.[94] However, suitable wide-band-gap top-cell materials for Si or thin film technologies that offer stability, high performance, and low cost have been lacking. In recent years, metal halide perovskite-based PVs have gained attention because of their high power conversion efficiencies (PCE) and low processing cost.[18,23,95–100] An attractive feature of this material is the ability to tune its band gap from 1.48 to 2.3 eV,[62,63] implying that we could potentially fabricate an ideal material for tandem cell applications.

Perovskite-based PVs are generally fabricated with organic-inorganic trihalide perovskites with the formulation ABX_3, where A is the methylammonium (CH_3NH_3) (MA) or formamidinium ($HC(NH_2)_2$) (FA) cation, B is commonly lead (Pb), while X is a halide (Cl, Br, and I). Although these perovskite structures offer high power conversion efficiencies (PCE), reaching > 20% PCE with band gaps of around 1.5 eV,[101] fundamental issues have been discovered when attempting to tune their band gaps to the optimum 1.7 to 1.8 eV range. In the case of $MAPb(I_{(1-x)}Br_x)_3$, Hoke *et al*. reported that light-soaking induces a halide segregation within the perovskite.[26] The formation of iodide-rich domains with lower band gap result in an increase in sub-gap absorption and a red-shift of photoluminescence (PL). The lower band gap regions limit the voltage attainable with such a material, so this band gap "photoinstability" limits the use of $MAPb(I_{(1-x)}Br_x)_3$ in tandem devices.[26] In addition, when considering real-world applications, $MAPbI_3$ is inherently thermally unstable at 85°C, even in an inert atmosphere (international regulations require a commercial PV product to withstand this temperature).[102]

Concerning the more thermally stable $FAPbX_3$ perovskite, an increase in optical band gap has not resulted in an expected increase in V_{oc}.[63] Furthermore, as iodide is substituted with bromide, a crystal phase transition occurs from a trigonal to a cubic structure; in compositions near the transition, the material is unable to crystallize, resulting in an apparently "amorphous" phase with high levels of energetic disorder and unexpectedly low absorption. These compositions additionally have much lower charge-carrier mobilities in the range of 1 $cm^2V^{-1}s^{-1}$, in comparison to > 20 $cm^2V^{-1}s^{-1}$, in the neat iodide perovskite.[103] For tandem applications, these problems arise at the Br composition needed to form the desired top-cell band gap of ~1.7 to 1.8 eV.

Nevertheless, perovskite/Si tandem PVs have already been reported in a four-terminal[104,105] and two-terminal architectures.[106] However, their reported efficiencies have yet to surpass the optimized single-junction efficiencies, in part because of non-ideal absorber band gaps. It is possible to form a lower band gap triiodide perovskite material and current-match the top and bottom junctions in a monolithic architecture by simply reducing the thickness of the top cell. However, this method results in a non-ideal efficiency.

Herein, we address the issues of forming a photostable FA based perovskite with the ideal band gap for tandem PVs. We partially substitute the formamidinium cation with Cs and make the remarkable observation that the phase instability region is entirely eliminated in the iodide to bromide compositional range, delivering complete tunability of the band gap around 1.75 eV. We fabricate planar heterojunction perovskite PVs, demonstrating PCE of > 17% and stabilized power output (SPO) of 16%. To demonstrate the potential impact of this new perovskite material in tandem solar cells, we create a semi-transparent perovskite device, and measure the performance of a silicon PV after "filtering" the sunlight through the perovskite top cell.

4.3. Results and discussion

The A-site cations that could be used with lead halides to form suitable perovskites for PVs are Cs, MA, and FA. $CsPbI_3$ does form a "black phase" perovskite with a band gap of 1.73 eV, however, this appropriate phase is only stable at temperatures above 200º to 300 °C and the most stable phase at room temperature is a non-perovskite orthorhombic "yellow" phase. MA based perovskites are thermally unstable and suffer from halide segregation instabilities, and are thus likely to be unsuitable.[102] FA based perovskites are the most likely to deliver the best balance between structural and thermal stability.[63,107–111] However, in Figure 27A, we show photographs of a series of $FAPb(I_{(1-x)}Br_x)_3$ films; we observe a "yellowing" of the films for compositions of x between 0.3 and 0.6, consistent with the previously reported phase instability caused by a transition from a trigonal ($x<0.3$) to cubic ($x>0.5$) structures.[63]

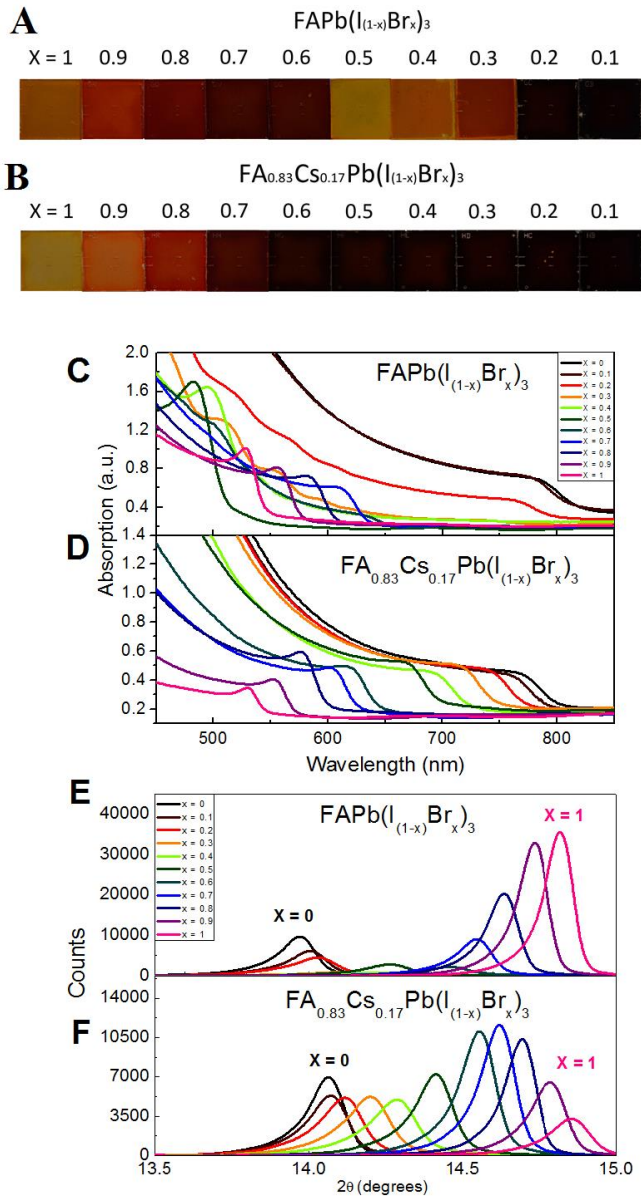


Figure 27: Photographs of perovskite films with Br composition increasing from x = 0 to 1 *for (**A**) $FAPb(I_{(1-x)}Br_x)_3$ and (**B**) $FA_{0.83}Cs_{0.17}Pb(I_{(1-x)}Br_x)_3$. (**C**) UV-Vis absorbance spectra of films of $FAPb(I_{(1-x)}Br_x)_3$ and (**D**) $FA_{0.83}Cs_{0.17}Pb(I_{(1-x)}Br_x)_3$. (**E**) X-ray diffraction (XRD) pattern of $FAPb(I_{(1-x)}Br_x)_3$ and (**F**) $FA_{0.83}Cs_{0.17}Pb(I_{(1-x)}Br_x)_3$. We note that the stated compositions are the fractional compositions of the ions in the starting solution, and the actual composition of the crystallized films may vary slightly.*

We have previously observed that the band gap changes from 1.48 eV for $FAPbI_3$ to 1.73 eV for $CsPbI_3$.[63] Recently it has been shown that mixing Cs with FA or MA, results in a slight widening of the band gap.[112,113] We considered here the possibility that if we partially substitute FA for Cs, we could push this region of structural instability in the Br to I phase-space to higher energies, and thus potentially achieve a structurally stable mixed halide perovskite with a band gap of 1.75 eV. In Figure

27B, we show photographs of thin films fabricated from mixed-cation lead mixed-halide $FA_{0.83}Cs_{0.17}Pb(I_{(1-x)}Br_x)_3$ compositions. Unexpectedly, we do not simply shift the region of structural instability to higher energy, but we observe a continuous series of dark films throughout this entire compositional range. To confirm these observations, we also perform ultraviolet-visible absorption measurements. We obtained a sharp optical band edge for all compositions of the $FA_{0.83}Cs_{0.17}Pb(I_{(1-x)}Br_x)_3$ material (Figure 27C and D), in contrast to $FAPb(I_{(1-x)}Br_x)_3$, which shows weak absorption in the intermediate range.

In order to understand the impact of adding Cs upon the crystallization of the perovskite, we performed x-ray diffraction (XRD) on the series of films covering the I to Br compositional range. In Figure 27E, we show the XRD patterns for $FAPb(I_{(1-x)}Br_x)_3$, zoomed in to the peak around $2\theta \sim 14°$. Quite remarkably, for the $FA_{0.83}Cs_{0.17}Pb(I_{(1-x)}Br_x)_3$, the material is in a single phase throughout the entire composition range. The monotonic shift of the (100) reflection which we observed from $2\theta \sim 14.2°$ to 14.9°, is consistent with a cubic lattice constant shift from 6.306 to 5.955Å as the material incorporates a larger fraction of the smaller halide. The complete diffraction pattern for both $FAPb(I_{(1-x)}Br_x)_3$ and $FA_{0.83}Cs_{0.17}Pb(I_{(1-x)}Br_x)_3$ are shown in Figure 28.

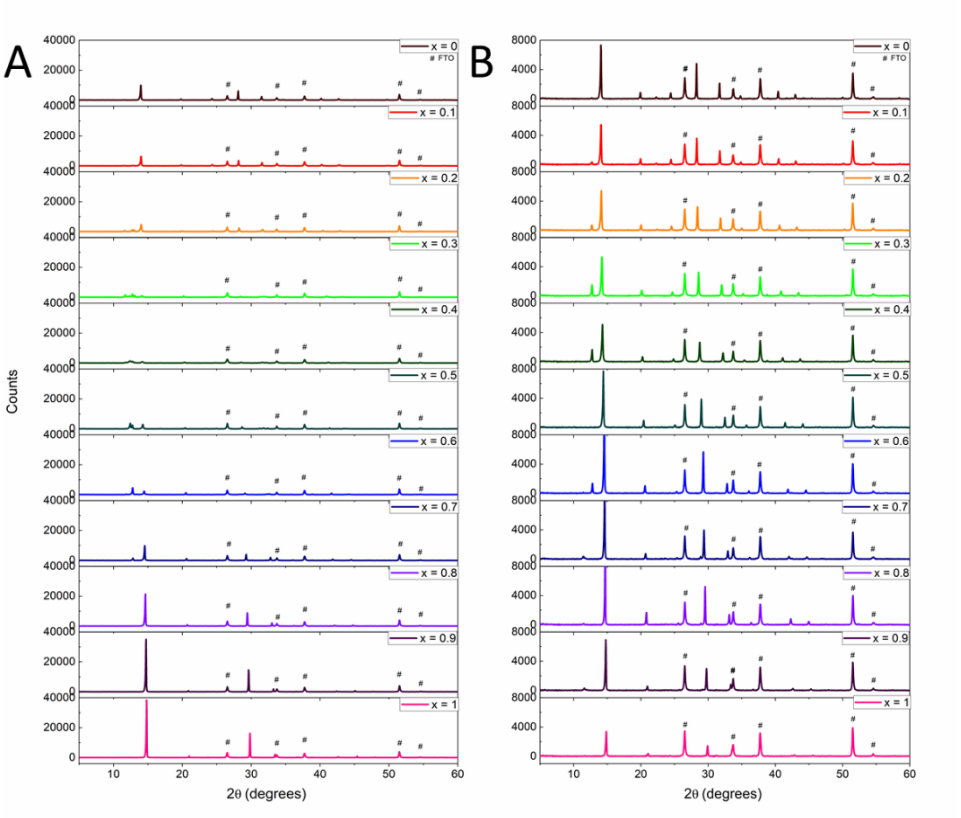


Figure 28: X-ray diffraction pattern (XRD) for 2 theta angles from 5 to 60 degree *for A) $FAPb(I_{(1-x)}Br_{(x)})_3$ perovskites and B) $FA_{0.83}Cs_{0.17}Pb(I_{(1-x)}Br_{(x)})_3$ formed on fluorine-doped tin oxide (FTO) coated glass substrates after annealed at 170°C for 10m.*

Thus, for the $FA_{0.83}Cs_{0.17}Pb(I_{(1-x)}Br_x)_3$ perovskite, we have removed the structural phase transition and instability over the entire compositional range. Quite remarkably over the entire Br to I range, and for a large fraction of the Cs-FA range, the variation in lattice constant, composition and optical band gap precisely follow Vegard's law, shown in Figure 29.

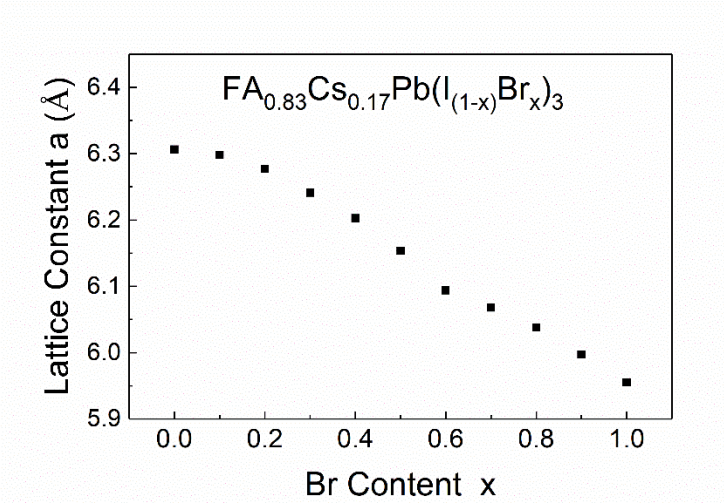


Figure 29: Lattice Constant of $FA_{0.83}Cs_{0.17}Pb(I_{(1-x)}Br_{(x)})_3$ perovskite system plotted as a function of bromide content. *This linear relationship between lattice constant and bromide content indicates that this system follows Vegard's law.*

Hence, we have complete flexibility and predictability in tuning of the composition and its impact upon the band gap. For the results that follow, we will use the precise composition $FA_{0.83}Cs_{0.17}Pb(I_{0.6}Br_{0.4})_3$, which has an optical a band gap of 1.74 eV as determined by a Tauc plot, shown in Figure 30.

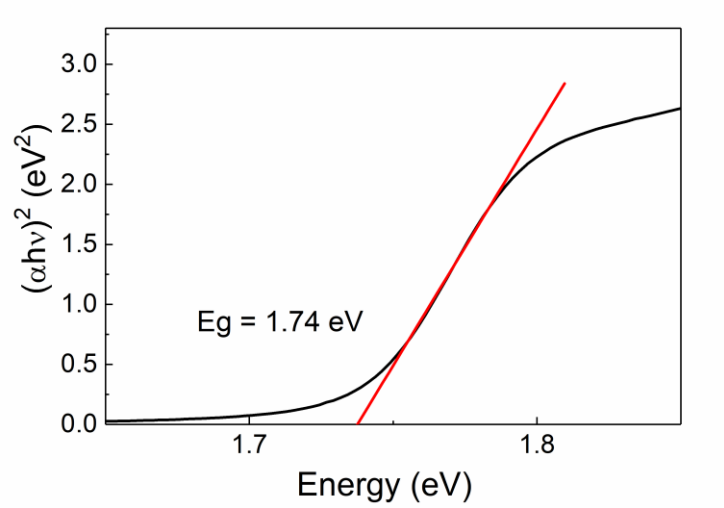


Figure 30: Tauc plot of the $FA_{0.83}Cs_{0.17}Pb(I_{0.6}Br_{0.4})_3$ perovskite composition assuming direct band gap and showing determination of optical band gap from intercept.

Photoinduced halide segregation has been reported in methylammonium lead mixed halide perovskites [26]. A red-shift in PL upon light illumination, for intensities ranging from 10 to

100 mW cm^{-2} occurs, with the shift to lower energies resulting from the formation of iodine-rich domains that have lower band gaps. This limits the achievable open-circuit voltage of the solar cell device by introducing a large degree of electronic disorder. In Figure 31, we show the PL from films of $MAPb(I_{0.6}Br_{0.4})_3$ perovskite and the mixed cation mixed halide material $FA_{0.83}Cs_{0.17}Pb(I_{0.6}Br_{0.4})_3$, immediately after prolonged periods of light exposure, using a power density of ~3 mW cm^{-2} and a wavelength of 550 nm as excitation source. We confirm the results observed by Hoke *et al*., where we see a time-dependent red-shift in PL for the $MAPb(I_{0.6}Br_{0.4})_3$ film, which exhibits a 130 meV PL red-shift after only 1 hour of illumination. In contrast, although we see a rise in PL intensity, we observe no significant red-shift in PL emission for the $FA_{0.83}Cs_{0.17}Pb(I_{0.6}Br_{0.4})_3$ precursor composition after 1 hour of identical light illumination (which we show in Figure 31).

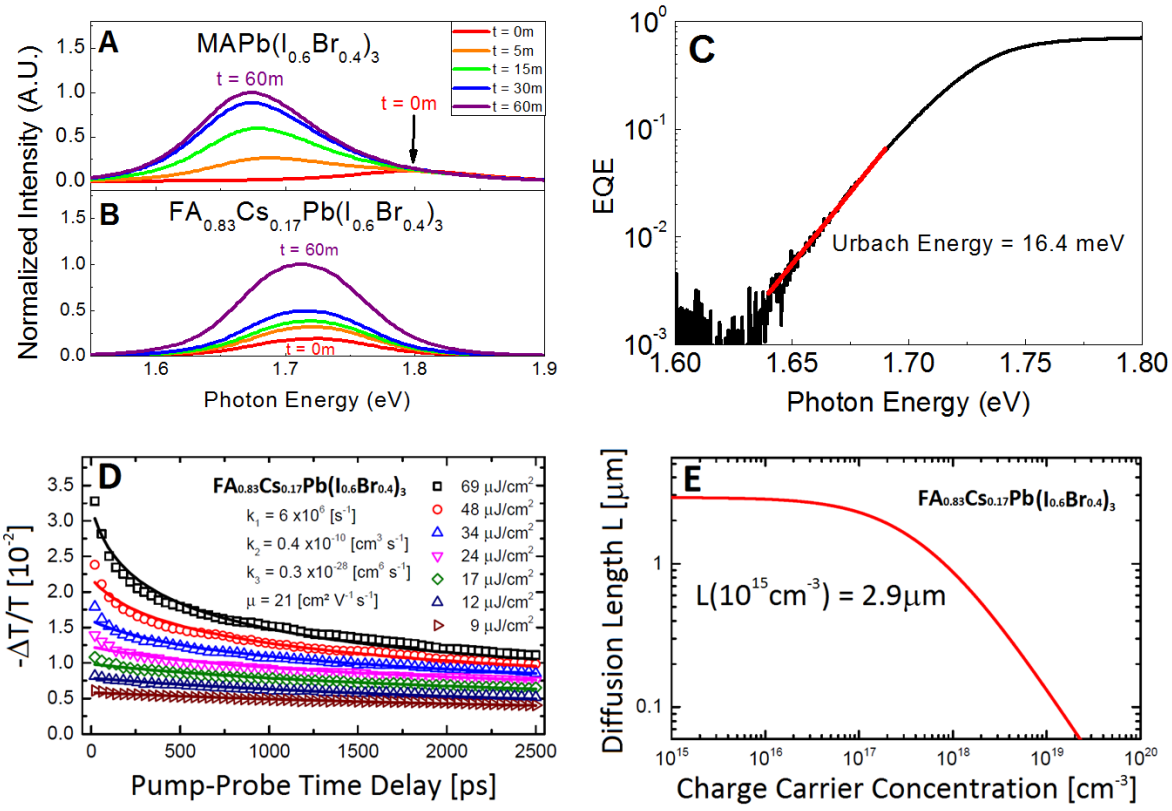


Figure 31: Material characteristics of $FA_{0.83}Cs_{0.17}Pb(I_{0.6}Br_{0.4})_3$ perovskite material. *Normalized photoluminescence (PL) measurement measured after 0, 5, 15, 30 and 60 minutes of light exposure of the (**A**) $MAPb(I_{0.6}Br_{0.4})_3$ and (**B**) $FA_{0.83}Cs_{0.17}Pb(I_{0.6}Br_{0.4})_3$ thin films. (**C**) Semi-log plot of external quantum efficiency (EQE) at the absorption onset for a $FA_{0.83}Cs_{0.17}Pb(I_{0.6}Br_{0.4})_3$ PV cell, measured using FTPS at short-circuit (Jsc). (**D**) OPTP transients for a $FA_{0.83}Cs_{0.17}Pb(I_{0.6}Br_{0.4})_3$ thin film, measured following excitation with a 35fs light pulse of wavelength 400nm with different fluences. (**E**) Charge-carrier diffusion length L as a function of charge concentration. OPTP transients and charge-carrier diffusion*

length were measured by Waqaas Rehman of the Department of Physics, University of Oxford. The Urbach energy was measured by Michael Johnston of the Department of Physics, University of Oxford.

Furthermore, we exposed a similar $FA_{0.83}Cs_{0.17}Pb(I_{0.6}Br_{0.4})_3$ film to monochromatic irradiance of much higher 5 Wcm^{-2} irradiance, and observed no red shift after 240s of illumination, shown in Figure 32. Under these identical conditions, we did observe a red shift in the PL for the single cation $FAPb(I_{0.6}Br_{0.4})_3$ perovskite, as we have previously reported.[103] We have shown that segregation can be significantly suppressed by employing an $FA_{(1-x)}Cs_xPb(I_{(1-y)}Br_y)_3$ perovskite system compared to a $MAPb(I_{(1-y)}Br_y)_3$ perovskite system. Although this shows significant improvements in photostability compared to MA-based perovskite, it remains to be seen whether segregation can be suppressed for a 25-year operational lifetimes.

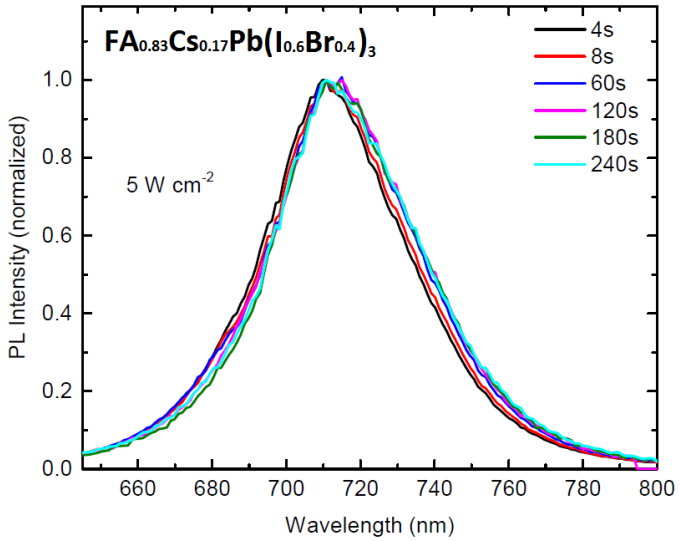


Figure 32: Photoluminescence spectra of $FA_{0.83}Cs_{0.17}Pb(I_{0.6}Br_{0.4})_3$ following excitation with pulse fluence of 0.5 µJcm-2 and laser intensity of 5 Wcm-2 at a wavelength of 405 nm. *The high intensity photoluminescence stability was measured by Waqaas Rehman of the Department of Physics, University of Oxford.*

Beyond halide segregation, a further deleterious observation previously made for mixed halide perovskites has been that the energetic disorder in the material is greatly increased in comparison to the neat iodide perovskites. The ultimate open-circuit voltage a solar cell material can generate is intimately linked to the steepness of the absorption onset just below the band edge, which can be quantified by the Urbach energy (E_u).[114,115] This E_u reported by De Wolf et al. and Sadhanala et

al. for $MAPbI_3$ was 15 meV,[115] where small values of E_u indicate low levels of electronic disorder. In contrast, the E_u for $MAPb(I_{0.6}Br_{0.4})_3$ perovskite increases to 49.5 meV.[66] We determined E_u by performing Fourier-transform photocurrent spectroscopy (FTPS) on complete planar heterojunction solar cells (details of the solar cells will be discussed below) and in Figure 31C we show the semi-log plot of external quantum efficiency (EQE) absorption edge of a device fabricated with the optimized precursor solution and annealing procedure. We calculated an E_u of 16.5 meV, near the values reported for the neat iodide perovskites.

In order to further asses the electronic quantity of $FA_{0.83}Cs_{0.17}Pb(I_{0.6}Br_{0.4})_3$ we have performed optical-pump terahertz-probe (OPTP) spectroscopy, which is a noncontact method of probing the photoinduced conductivity and effective charge carrier mobility in the material. In Figure 31D, we show the fluence-dependence of the OPTP transients, which exhibit accelerated decay dynamics at higher initial photoinjected charge-carrier densities, as the result of enhanced contributions from bimolecular and Auger recombination. We may extract the rate constants associated with different recombination mechanisms by global fits to these transients of the solutions to the rate equation:

$$\frac{dn(t)}{dt} = -k_3 n^3 - k_2 n^2 - k_1 n \tag{58}$$

We find that $FA_{0.83}Cs_{0.17}Pb(I_{0.6}Br_{0.4})_3$ exhibits an excellent charge-carrier mobility of 21 $cm^2V^{-1}s^{-1}$. For comparison, the corresponding neat-FA perovskite $FAPb(I_{0.6}Br_{0.4})_3$ only sustains charge-carrier mobilities <1 $cm^2V^{-1}s^{-1}$ that are related to the amorphous and energetically disordered nature of these materials.[103] Conversely, $FA_{0.83}Cs_{0.17}Pb(I_{0.6}Br_{0.4})_3$ displays a mobility value intermediate to those we have previously determined[103] for $FAPbI_3$ (27 $cm^2V^{-1}s^{-1}$) and $FAPbBr_3$ (14 $cm^2V^{-1}s^{-1}$) suggesting that it is no longer limited by structural disorder. We further assess the potential of $FA_{0.83}Cs_{0.17}Pb(I_{0.6}Br_{0.4})_3$ for incorporation into planar heterojunction PV architectures by deriving the charge-carrier diffusion length (L) as function of the charge-carrier density n:

$$L = \frac{\mu k_B T}{\sqrt{eR}} \tag{59}$$

Where $R = k_1 + nk_2 + n^2k_3$ is the is the total recombination rate, k_B is the Boltzmann constant, T is the temperature, and e is the elementary charge.

In Figure 31E, we show that for charge-carrier densities typical under solar illumination (n~10^{15}cm^{-3}) a value of L~2.9 µm is reached, comparable to values reported for high-quality thin films of neat lead iodide perovskites. [103,116] The high charge-carrier mobility and slow recombination kinetics, and long charge carrier diffusion length imply that this mixed cation, mixed halide perovskite should be just as effective as a high-quality solar cell absorber material as the neat halide perovskite $FAPbI_3$.

Furthermore, we conducted an accelerated thermal stress test on perovskite thin films to compare the thermal stability of the $FA_{0.83}Cs_{0.17}Pb(I_{0.6}Br_{0.4})$ with the $MAPb(I_{0.6}Br_{0.4})_3$ perovskite. Under thermal stressing at 130 °C in nitrogen, we observe distinct optical band gap and the crystal lattice behaviors for $FA_{0.83}Cs_{0.17}Pb(I_{0.6}Br_{0.4})_3$ compared to $MAPb(I_{0.6}Br_{0.4})_3$. In Figure 33 we show that after only the first few hours of thermal stressing, the $MAPb(I_{0.6}Br_{0.4})_3$ loses its band edge and the (100) perovskite peak located at ~14.5° disappears while the $Pb(I_{0.6}Br_{0.4})_2$ peak increases. On the other hand, the $FA_{0.83}Cs_{0.17}Pb(I_{0.6}Br_{0.4})_3$ perovskite maintain its optical band edge and (100) perovskite intensity peak. Although we can observe the rise of the $Pb(I_{0.6}Br_{0.4})_2$ peak, it increases at a significantly slower rate than the MA-based perovskite.

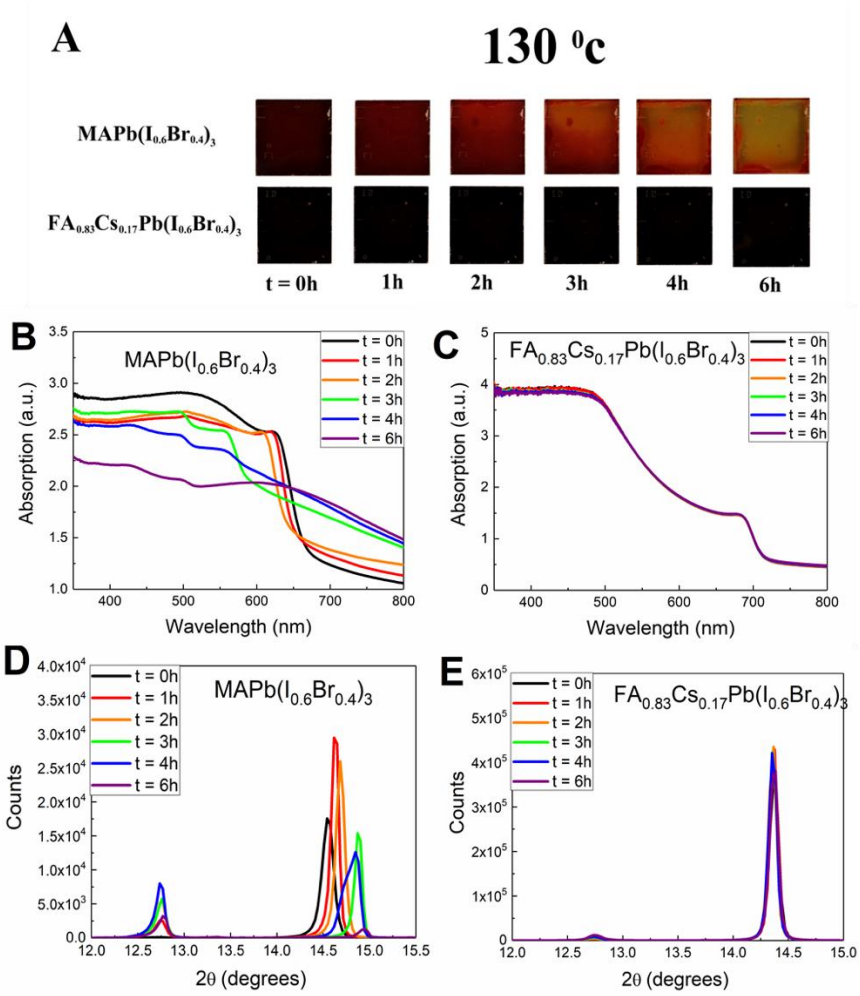


Figure 33: Mixed-halide perovskite films heated on a 130 °C hotplate inside a N_2 glovebox (~4ppm O_2 and ~0.5ppm H_2O) for a period of up to 6 hours. *(**A**) Images (**B**) UV-VIS absorption of $MAPb(I_{0.6}Br_{0.4})_3$ (**C**) UV-VIS absorption of $FA_{0.83}Cs_{0.17}Pb(I_{0.6}Br_{0.4})_3$ (**D**) XRD of $MAPb(I_{0.6}Br_{0.4})_3$ (**E**) XRD of $FA_{0.83}Cs_{0.17}Pb(I_{0.6}Br_{0.4})_3$*

We fabricated a series of planar heterojunction solar cells to assess the overall solar cell performance. We show the device architecture in Figure 34A, which is composed of a SnO_2/phenyl-C_{60}-butyric acid methyl ester ($PC_{60}BM$) electron-selective layer, a solid $FA_{0.83}Cs_{0.17}Pb(I_{0.6}Br_{0.4})_3$ perovskite absorber layer, and Li-TFSI-doped spiro-OMeTAD with 4-tert-butylpyridine (TBP) additive as the hole-collection layer, caped with an Ag electrode. We measured current–voltage (*I-V*) characteristics of such devices under simulated air-mass (AM) 1.5 100 mW cm^{-2} sunlight, and show the *I-V* characteristics of one the highest performing device in Figure 34B. It delivered a short-circuit current density of 19.4 mA cm^{-2}, a V_{OC} of 1.2 V, and a PCE of 17.1 %. By holding the cell at a fixed maximum power point forward bias voltage of 0.95 V, we measured the power output over time reaching a stabilized efficiency of 16% (Figure 34C). In Figure 34D, we show the spectral response of

the solar cell, which confirms the wider band gap of the solar cell, and also integrates over the AM1.5 solar spectrum to give 19.2 mA cm^{-2}, in close agreement to the measured J_{SC}.

This performance is very competitive with the best reported single junction perovskite solar cell reported so far,[114,117] especially considering the wider band gap of our material which should result in a few percent absolute efficiency drop with respect to a 1.57 eV material [118]. Importantly for tandem solar cells, this 1.74 eV material appears to be capable of generating a higher V_{OC} than the 1.57 eV triiodide perovskites in planar heterojunction solar cells. Following Rau *et al.,*[119] from the integration of the EQE over the black body radiation spectrum, we estimate the maximum attainable V_{OC} for our $FA_{0.83}Cs_{0.17}Pb(I_{0.6}Br_{0.4})_3$ device to be 1.42 V, which is 100 mV higher than that estimated for $MAPbI_3$ devices by Tvingstedt *et al*. and Tress *et al*.[114,117]

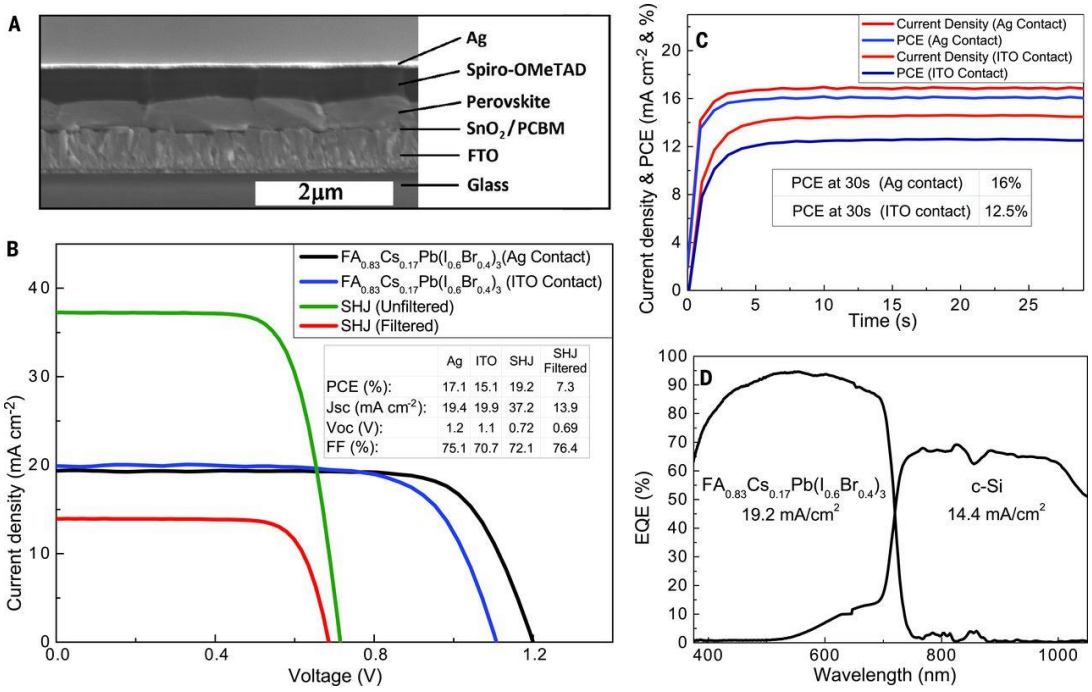


Figure 34: Device architecture and I-V characteristics for $FA_{0.83}Cs_{0.17}Pb(I_{0.6}Br_{0.4})_3$ perovskite and Si PV cells. *(**A**) SEM image of cross-section of a planar heterojunction solar cell (**B**) Forward bias to short-circuit I–V curve for the best perovskite devices fabricated, using either a Ag metal, or semi-transparent ITO top electrode, measured at 0.38V/s scan rate. We also show the current voltage curve of a silicon heterojunction (SHJ) cell, measured with direct light or with the simulated sunlight filtered through the semi-transparent perovskite solar cell [120]. We note that the SHJ cells were measured at the Centre For Renewable Energy Technologies (CREST), Loughborough UK under an extremely well calibrated solar simulator. (**C**) Photocurrent density and power conversion efficiency measured at maximum power point for a 30s time span (**D**) External quantum efficiency (EQE) spectrum measured in short-circuit (Jsc) configuration for the highest efficiency perovskite cell and the SHJ cell measured with the incident light filtered through the semi-transparent perovskite cell. The filtered silicon heterojunction solar cell with the perovskite was measured by Golnaz Sadoughi of the Department of Physics, University of Oxford. The silicon heterojunction solar cell was prepared by Lars Korte and Bernd Rech of the Helmholtz-Zentrum, Institute for Silicon Photovoltaics, Berlin.*

In order to demonstrate the potential impact of using this new perovskite composition in a tandem architecture, we fabricated semitransparent perovskite solar cells by sputter coating ITO on top of the perovskite cells, with the additional inclusion of a thin "buffer layer" of solution processed ITO nanoparticles between the spiro-OMeTAD and the ITO. The efficiency of the semi-transparent $FA_{0.83}Cs_{0.17}Pb(I_{0.6}Br_{0.4})_3$ solar cells is 15.1%, as determined by the *J-V* curve, with a stabilized power output of 12.5%. Because J_{SC} is similar to the cell with the Ag electrode, we expect that the slight drop in V_{OC} and SPO will be surmountable by better optimization of the ITO sputter deposition procedure and buffer layer. We measured a Si heterojunction (SHJ) cell, with and without a semi-transparent perovskite cell held in front of it, and determined an efficiency of 7.3% filtered, and 19.2% when uncovered. These results demonstrate the feasibility of obtaining a combined tandem solar cell efficiency of 19.8%, if we combine with the stabilized power output of the semi-transparent cell. However, significantly higher efficiencies can certainly be attained with simple improvements to the semi-transparent contact, where most of the losses were observed. Considering further minor improvements in the perovskite, optical management and integration and choice of Si rear cell, it is feasible that this system could deliver up to 30% efficiency. In addition, this monotonic tunability of band gap across the visible spectrum within a single crystalline phase, will have direct impact to the color tunability and optimization of perovskites for light emitting applications.

4.4. Conclusion and outlook

In short, this chapter has presented a novel and promising $FA_{(1-x)}Cs_xPb(I_{(1-y)}Br_x)_3$ perovskite system for tandem application, which provides both stability and high efficiency. We eliminated the use of the volatile methylammonium cation, and substituting it with a thermally stable formamidinium-cesium mixed-cation, where the inorganic cesium cation serves to stabilize the $FAPbI_3$ black perovskite by forcing it into a more favorable cubic lattice. This mixed-halide perovskite shows greater stability compared to $MAPb(I_{(1-y)}Br_x)_3$, when stressed under illumination. We also measured low Urbach energies, compared to neat halide perovskite systems, for the specific $FA_{0.83}Cs_{0.17}Pb(I_{0.6}Br_{0.4})_3$ perovskite composition, indicative of low electronic disorder in the semiconductor. Lastly, we measured charged-carrier mobilities and diffusion lengths comparable to neat halide perovskite system, which indicated that the $FA_{(1-x)}Cs_xPb(I_{(1-y)}Br_x)_3$ systems could potentially reach similar efficiencies, assuming non-radiative losses are comparable to MA-based perovskites.

This combination of exceptional properties, allowed for the fabrication of highly efficiency and stable mixed-halide planar devices, reaching 17.1% (16% stabilized) and an open-circuit voltage of over 1.2V, with an opaque electrode. Using an ITO nanoparticle buffer layer and a sputtered ITO layer, we deposited a semi-transparent electrode, which combined with a c-Si cell, allowed us to demonstrate a four-terminal tandem architecture, reaching 22.4% (19.8% stabilized).

5. Crystallization kinetics and morphology control of formamidinium-cesium mixed-cation lead mixed-halide perovskite via tunability of the colloidal precursor solution

The work in this chapter has been adapted and reproduced in part with permission from:

*David P. McMeekin,[1] Zhiping Wang,[1] Waqaas Rehman,[1] Federico Pulvirenti,[2] Jay B. Patel,[1] Nakita K. Noel,[1] Michael B. Johnston,[1] Seth R. Marder,[2] Laura M. Herz,[1] Henry J. Snaith[1]**, Crystallization kinetics and morphology control of formamidinium-cesium mixed-cation lead mixed-halide perovskite via tunability of the colloidal precursor solution, *Adv. Mater. 2017, 29, 1607039*. Copyright 2017 Wiley, Advanced Materials.

5.1. Context and summary

The meteoric rise of the perovskite solar cell field has been fueled by the ease with which a wide range of high-quality materials can be fabricated via simple solution processing methods. However, to date, little effort has been devoted to understanding the precursor solutions, and the role of additives such as hydrohalic acids upon film crystallization and final optoelectronic quality. In this chapter, we establish a direct link between the colloids concentration present in the $[HC(NH_2)_2]_{0.83}Cs_{0.17}Pb(Br_{0.2}I_{0.8})_3$ precursor solution and the nucleation and growth stages of the thin film formation. Using dynamic light scattering analysis, we monitor the dissolution of colloids over a time span triggered by the addition of hydrohalic acids. These colloids appear to provide nucleation sites for the perovskite crystallization, which critically impacts morphology, crystal quality, and

optoelectronic properties. Via two-dimensional X-ray diffraction we observe highly ordered and textured crystals for films prepared from solutions with lower colloidal concentrations. This increase in material quality allows for a reduction in microstrain along with a twofold increase in charge-carrier mobilities leading to values exceeding $20 cm^2V^{-1}s^{-1}$. Using a solution with an optimized colloidal concentration, we fabricated devices that reach current-voltage measured power conversion efficiency of 18.8%, and stabilized efficiency of 17.9%.

5.2. Introduction

In recent years, metal halide perovskite solar cells have gained tremendous attention, reaching certified efficiencies of 22.1% power conversion efficiency.[121,122] This rapid success is partly due to a versatile solution-based fabrication process which allows for a wide range of deposition techniques such as: spin-coating,[17,18] two-step interdiffusion,[97] dip coating,[97] inkjet printing[123,124] and spray pyrolysis.[125] These solution-based fabrication methods of perovskite films have been used in a variety of devices ranging from field-effect transistors,[126] light emitting devices (LED),[127] photo-detectors,[128,129] to solar cells.[18,23,96,97] Although most perovskite thin films are fabricated using a salt-based precursor solution, little effort has been dedicated to characterizing the structure and time dependent evolution of the species present in solution and the impact this has on the quality of the resulting films. Furthermore, it has been shown that additives to the precursor solution can impact the nucleation rate, morphology, grain size and crystallinity of the perovskite. Additives, such as polymers,[130] small molecules,[131,132] metal ions,[133] water[134] or acids,[63,135–140] can play a vital role in material quality, enabling improvements in material stability, optoelectronic properties, and photovoltaic performance.

Work by K. Yan et al. characterized the 1:1 CH_3NH_3I:PbI_2 stoichiometric precursor solution as a colloidal dispersion in a mother solution, rather than a pure solution.[141] When fabricated on planar substrate, this colloidal solution forms films with poor morphology, due to the presence of rod-shaped colloids comprised of a soft coordination complex in the form of a lead polyhalide framework.[141] The authors show that the colloid distribution can be tuned by varying the organic to inorganic compound ratio in the precursor solution, using excess CH_3NH_3I (MAI) and CH_3NH_3Cl (MACl). However, the authors were unable to remove the 1D PbI_2 rod-like structures in the widely used stoichiometric 1:1 precursor solution. Adding excess organic cation to dissolve these colloids may be incompatible with recently published mixed-cation perovskites that contain both organic and inorganic cations,[112,142–144]

since this will alter the precise $[HC(NH_2)_2]^+$ (formamidinium, FA) to Cs ratio, which is required to form the appropriate perovskite composition. In addition, FAI has a lower effective volatility than MACl for instance, and hence excess quantities will not be so readily removed. Herein, we address this problem by utilizing acidic additives to trigger the dissolution of the colloids in the precursor solution. However, after the initial incorporation of the acid, full dissolution of the colloids occurs over a period of tens to hundreds of hours. We show that with a fixed concentration of additional hydrohalic acids, we can transition from a colloidal solution to one without any large colloids by simply using time as a varying parameter, thus decoupling the observed effects from additional coordination of halide ions, as recently reported by J. Pan et al.[138] We show that during this time period, the colloids in suspension gradually dissolve, critically impacting the crystallization kinetics of the thin films. Thus, we show that the colloidal concentration in the precursor solutions plays a significant role in determining the variations in morphology, crystallinity, texture, and optoelectronic properties of the perovskite.

In this work, we focus on the role of hydrohalic acids, specifically hydroiodic (HI) and hydrobromic (HBr), as additives, when incorporated into the mixed-cation lead mixed-halide $FA_{0.83}Cs_{0.17}Pb(Br_{0.2}I_{0.8})_3$ perovskite precursor solution. Although hydrohalic acids have previously been used as additive to precursor solutions to create smoother films, improve their surface coverage,[63,138] alter crystal structure,[137] and even reduce the onset temperature of crystallization of the all inorganic $CsPbI_3$ perovskite,[145] there is still little understanding of what is driving this behavior. Here, using dynamic light scattering (DLS), we link the effect of an acid additive to the dissolution of the lead polyhalide colloidal framework. We show that by dissolving the colloids over a given time period, we can substantially change the nucleation and growth dynamics and hence, the final film morphology of the mixed-cation lead mixed-halide perovskite system. In turn, film quality is improved by increasing grain size, crystallinity, and charge-carrier mobilities. However, we observe a trade-off between morphology and crystal quality, where films with the largest grain size are prone to pinhole formation. Recently, it has been shown that improvements in crystallinity and larger grain sizes can impact the stability of the perovskite thin film.[70,146] Using a precursor solution with an optimized colloidal distribution, we fabricated planar heterojunction n-i-p perovskite solar cells, demonstrating current-voltage determined power conversion efficiencies of over 18.8%, and a stabilized efficiency of 17.9%.

5.3. Results and discussion

Morphology plays a key role in the device performance of perovskite solar cells. Poor morphology can lead to the creation of voids in the perovskite thin film, which will reduce the surface coverage of the light-absorbing layer, thus reducing the short-circuit (J_{SC}) of the device. More importantly, the pinholes will also result in an undesirable contact between the electron and hole selective charge extraction layers. This contact area between the n and p-type layers creates paths of low resistance within the solar cell, thus reducing the shunt resistance (R_{SH}), and ultimately reducing the open circuit voltage (V_{OC}) and fill factor (FF) of the device. Here, we present a simple and effective method of controlling the morphology of the mixed-cation lead mixed-halide perovskite by tuning the density of colloids found in the precursor solution. We suggest that these lead polyhalide colloids, identified as $[PbX_3]^{-1}$, $[PbX_4]^{2-}$, $[PbX_5]^{3-}$, $[PbX_6]^{4-}$ by K. Yan et al.,[141] serve as nucleation centers in the formation of perovskite thin films.

We first show that tuning the distribution of the various colloids within the precursor solution impacts the crystallization kinetics of the perovskite. We first investigate if the addition of hydroiodic (HI) and hydrobromic (HBr) acids to the perovskite precursor solution has an impact upon the colloids in the solution. Our precursor solution is composed of CsI, FAI, $PbBr_2$ and PbI_2 in order to obtain a molar ratio of FA:Cs:Br:I of 0.83:0.17:0.2:0.8 in DMF [N,N-Dimethylformamide] at a 1.15 molar concentration. To this solution we added HI and HBr to obtain a halogen molar ratio of 8:2, resulting in the addition of a volume concentration of 81.7µL/mL of HI (57 wt.% in H_2O) and 17.6µL/mL of HBr (48 wt. % in H_2O). In Figure 35A, we show photographs of films coated from precursor solutions with various aging times after the addition of the acid, after spin-coating and a low temperature 70 °C drying step in a nitrogen atmosphere. We observe a noticeable color change, from black to yellow, as a function of time after addition of the acids. For solutions without an acidic additive, the films turn dark during the spin-coating process, prior to the 70 °C drying step, whereas with hydrohalic acid, the as spun films only show a slight color change. In Figure 35B, we show the DLS intensity distribution of these precursor solutions after the initial addition of the acid. Over the course of time, we see the disappearance of the large hydrodynamic micron-sizes particle distribution. In Figure 35C we show the ultraviolet-visible (UV-vis) absorbance spectra of the corresponding 70 °C dried thin film. We observe the gradual disappearance of the black perovskite absorption onset.

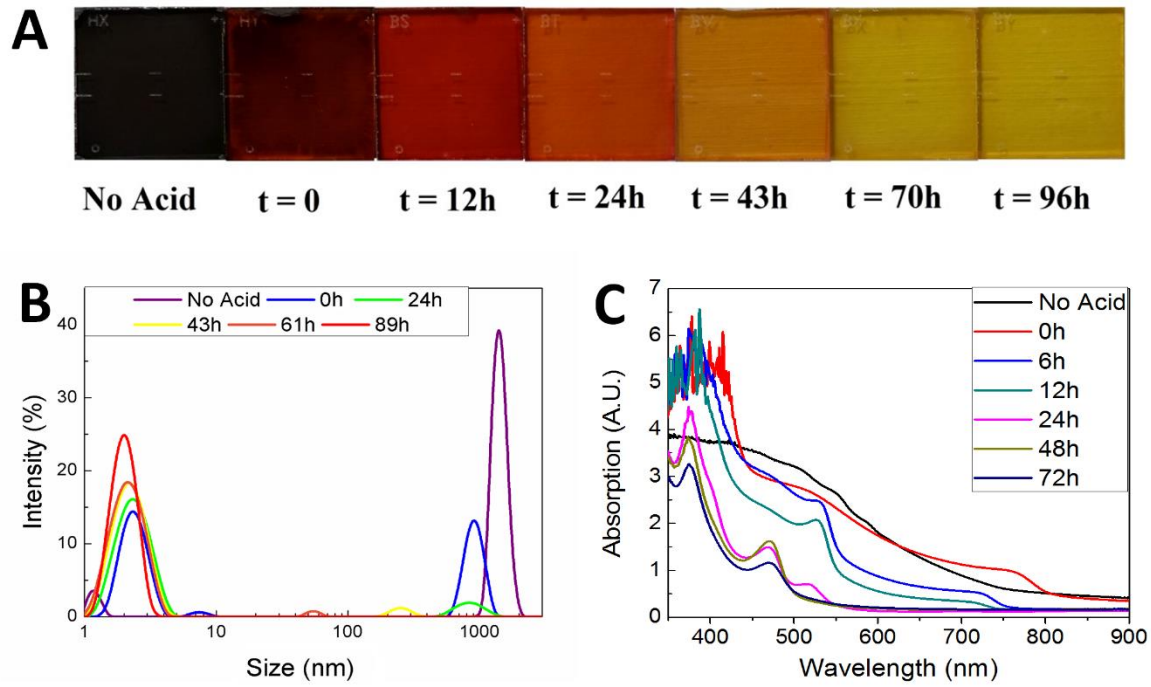


Figure 35: Impact of colloids in the precursor solution on the nucleation stage of the $FA_{0.83}Cs_{0.17}Pb(Br_{0.2}I_{0.8})_3$ perovskite system. *A) A series of photographs of thin films spin-coated and dried at 70°C under nitrogen, prepared with solutions aged in a N_2 atmosphere for various periods of time after the addition of hydrohalic acid. B) Colloidal hydrodynamic size distribution via dynamic light scattering of various perovskite solutions. C) Ultraviolet-visible absorbance spectra of corresponding thin-films.*

The colloids that are initially present in the stoichiometric $FA_{0.83}Cs_{0.17}Pb(Br_{0.2}I_{0.8})_3$ perovskite precursor solution appear to slowly dissolve over the course of days after the addition of the hydrohalic acids. After the addition of the acids, a noticeable increase in solubility can be seen with the naked eye, where the solution loses its opaque or "cloudy" appearance and becomes a translucent yellow solution. Nevertheless, these clear solutions still display a Tyndall effect (light scattering). It has been reported that the measured DLS intensity relates to rod-shaped colloids.[141] As we show in Figure 36, we observe the presence of these nanorods in unheated thin films prepared with an acid-free solution, consistent with observations made by K. Yan et al. and D. Bi et al.[141,147]

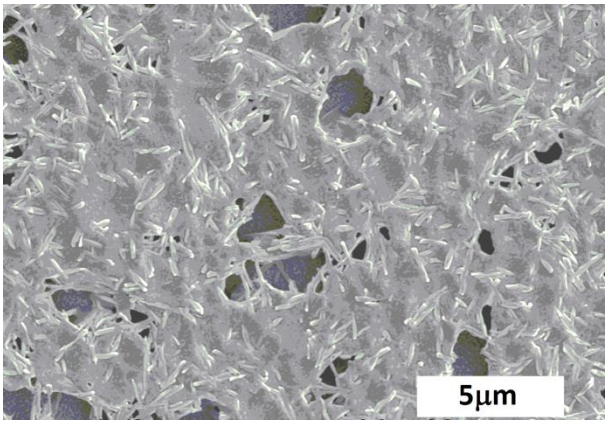


Figure 36: Scanning electron microscopy (SEM) image of the top view of an un-annealed $FA_{0.83}Cs_{0.17}Pb(Br_{0.2}I_{0.8})_3$ as cast thin film, prepared with an acid-free perovskite precursor solution.

The colloid concentration in the precursor solution can be tuned using two methods: by timing the addition of the acid additives, as we show in Figure 35, or simply by mixing a fully aged "colloid-free" solution with a fresh colloidal solution, immediately prior to spin-coating, as we show in Figure 37.

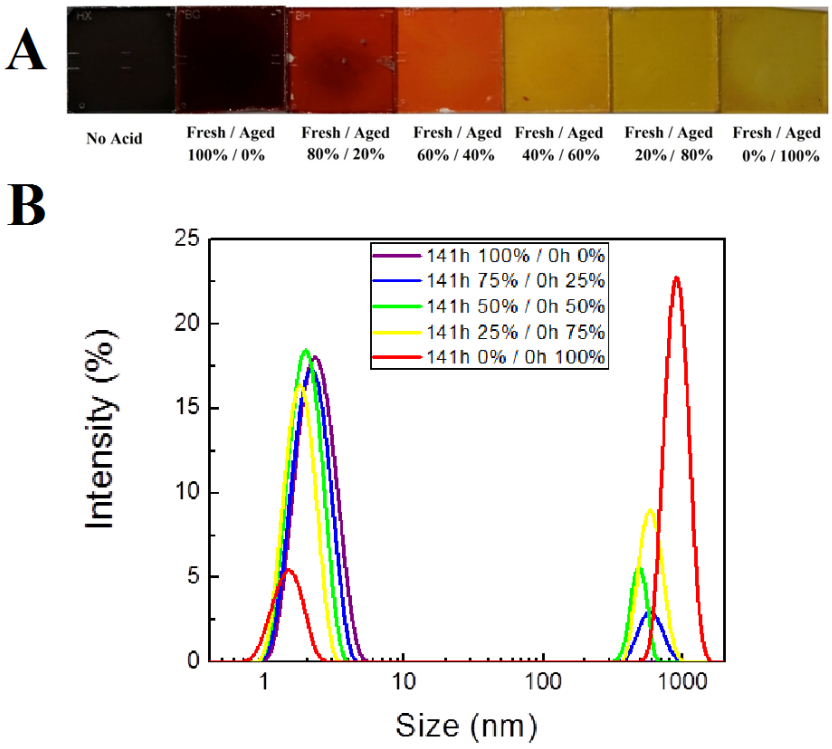


Figure 37: Impact of mixing colloidal solutions with colloid-free solution on the nucleation stage of the $FA_{0.83}Cs_{0.17}Pb(Br_{0.2}I_{0.8})_3$ perovskite system. *A) A series of photographs of thin films spin coated and annealed at 70 °C under nitrogen, prepared by mixing a colloidal solution with a colloid-free solution B) Hydrodynamic size distribution measured via dynamic light scattering of various perovskite solutions prepared via colloidal mixing of solution.*

We also note that the hydrohalic acids have considerable amount of water, ranging from 48 wt% for HBr to 57 wt% for HI. However, the addition of water did not contribute to significant colloid dissolution. Furthermore, we observe a decrease in scattering behavior of the precursor solution, along with a delay in perovskite nucleation, and an increase in grain sizes for films prepared with HPA as additive, a non-halogenated acid, while the addition of iodine and bromine do not result in a nucleation delay or larger grain sizes. Although the addition of HPA lead to poor film morphology for the $FA_{0.83}Cs_{0.17}Pb(Br_{0.2}I_{0.8})_3$ perovskite system, this result points towards the proton being the active component in hydrohalic acids, rather than the halide anions.

We now focus on our investigation of the subsequent high-temperature annealed perovskite films, during crystallization, in more detail. In Figure 38, we show optical micrographs of the films during their annealing process. Although in most films we cannot resolve individual perovskite crystallites and/or nucleation centers in the optical micrograph, we interpret these images to indicate that the density of nucleation sites for crystal growth is reduced, as the solution aging time after acid addition is increased. After the first nucleation stage, a subsequent stage follows where crystal growth occurs. Already in the t = 0 s films, there may have been some degree of growth that is resulting in the red/brown coloration of the films due to the low temperature 70°C drying step. However, for full crystallization, a high-temperature heating process converts all colored films into the black perovskite phase. Furthermore, we observe that solutions with higher colloidal concentrations result in short growth periods, where crystal growth has already largely occurred during the 70 °C drying step, and remains relatively unchanged during the high-temperature (Figure 38A) anneal. However, solutions with lower colloidal concentrations allow for a longer crystal growth, where the black perovskite phase appears later into the crystal growth period (Figure 38C-E). Figure 38A-D shows a dense and uniform distribution of growing crystals, resulting in impingement of the grains against one another during the growth stage and providing a full surface coverage. Although Figure 38E does not provide full surface coverage, we observe at t = 45 s the initial growth of the black perovskite phase crystals, originating from individual seeds.

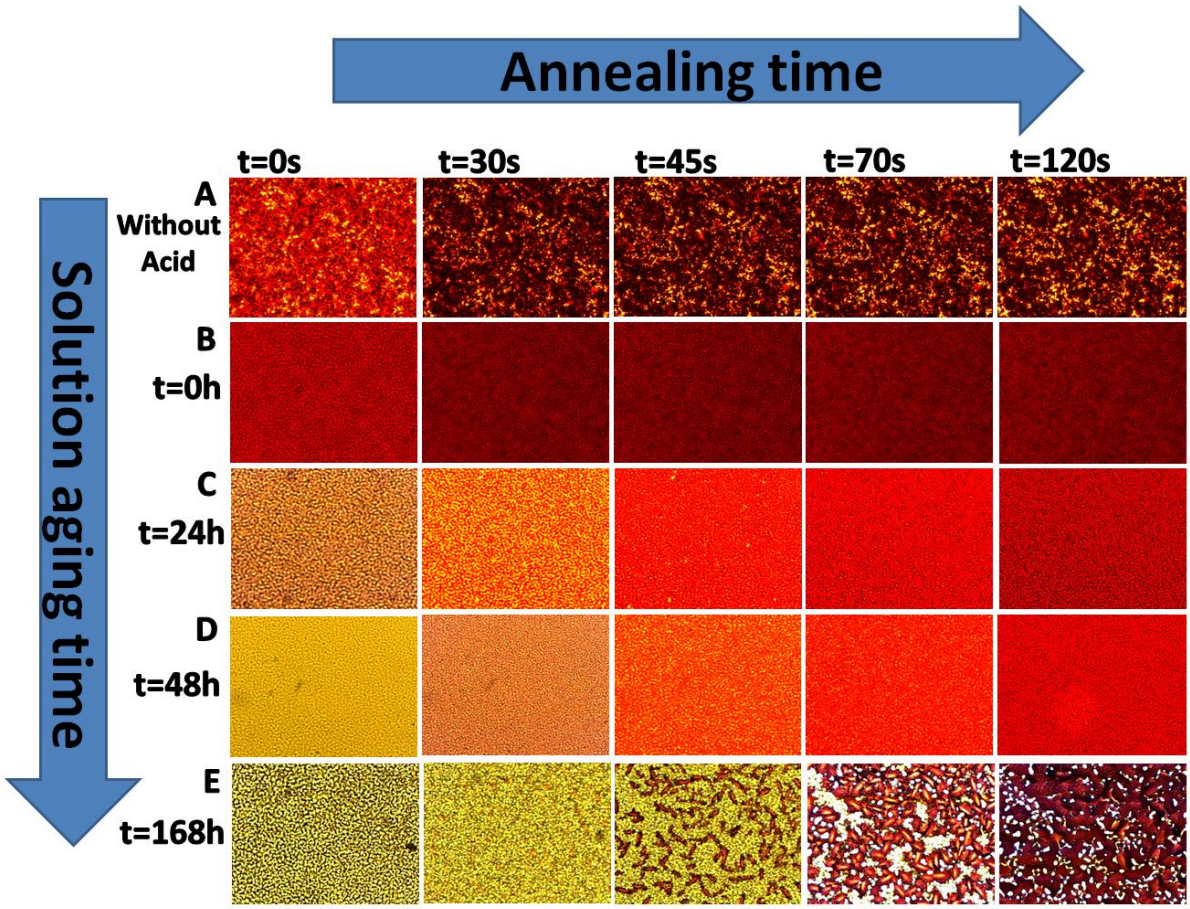


Figure 38: Growth kinetics of the $FA_{0.83}Cs_{0.17}Pb(Br_{0.2}I_{0.8})_3$ perovskite system with various colloid concentrations. *Microscope images using a 50× magnification of post-nucleation thin films heated at 220°C in an air atmosphere; prepared using precursor solutions aged with an acid for a period of time. Precursor solution aged for A) 0h without hydrohalic acids, B) 0h with the addition of acids, C) 24h, D) 48h, E) 168h.*

We now appear to have sufficient information to provide a hypothesis about the impact of the addition of the acids, and the presence of the colloids upon thin film crystallization. The nucleation and growth characteristics of perovskite crystals are both affected by the amount and size of nuclei located in the precursor solution. We propose that the large colloids, inherently present in the $FA_{0.83}Cs_{0.17}Pb(Br_{0.2}I_{0.8})_3$ perovskite precursor solution, act as nucleation sites to initiate the perovskite formation. Thin films prepared with solutions with high scattering light behavior caused by the colloids, undergo rapid perovskite crystallization due to the higher nucleation site density, while films prepared with precursor solutions that have little to no colloids lead to a prolonged crystal growth period due to fewer nucleation sites.

From classical nucleation theory, we know that nucleation can occur in a heterogeneous or a homogeneous manner[148]. In the case of perovskite thin films, nucleation occurs on foreign surfaces

and/or via nuclei; thus heterogeneous nucleation is likely to be the dominant nucleation mechanism. The impact of surface energy on morphology, using n and p-type layers with various wetting properties, has been discussed by Bi et al.[149]. However, the free energy barrier for nucleation can also be lowered with the introduction, or existence of nuclei in the perovskite solution. Let us consider a simplified case of heterogeneous nucleation where a solid, spherically shaped nucleus, immersed in a liquid, is located on a solid surface. The free energy needed for heterogeneous nucleation relates to the corresponding free energy change associated with its homogeneous nucleation multiplied by a factor relating to interfacial tensions γ.[150–152] Since this factor is less than unity, heterogeneous systems have a lower free energy change than homogeneous systems, and thus a lower nucleation barrier.

$$\Delta G_{Heterogeneous} = \Delta G_{Homogeneous} \frac{(2 + cos\,\theta)(1 - cos\,\theta)^2}{4} \tag{60}$$

where θ is the contact angle between the crystalline deposit and the foreign solid surface, corresponding to a wetting angle.

Here, by controlling the concentration of lead polyhalide colloidal dispersion in the precursor solution, we are effectively tuning the interfacial tensions γ between the liquid solution, solid colloid and substrate, thus varying the amount of preferential sites where heterogeneous nucleation occurs. Therefore, even if the colloids are lead polyhalide colloids and not perovskite colloids, we postulate that the colloids offer preferential sites for heterogeneous nucleation and are thus acting as nucleation sites during the crystallization. Incidentally, with few heterogeneous nucleation sites, polycrystalline film growth occurs so sparsely that the growing domains do not fully impinge upon each other, and non-uniform films with pinholes are produced.

In Figure 39 we show the impact of the colloidal concentration on the morphology, grain size and crystallinity of the perovskite films. In Figure 39A-E we show the scanning electron microcopy (SEM) of the perovskite films deposited using various precursor solutions on fluorinated tin oxide (FTO) substrates. The use of an “acid-free” perovskite solution results in a thin film with significant amounts of pinholes and inter-granular cracking. The addition of the acids, which triggers the dissolution of the colloids over, allows for the growth to commence after spinning of the sample. Figure 39A-D show the increase in grain size from ~100 nm without the addition of the acids to several microns for colloid-free solutions under identical annealing conditions. Figure 39E shows the

formation of cube-like crystals grains with distinguishable facets when annealed at a higher temperature, illustrating the compromise between grain size and morphology.

By reducing the density of nucleation sites, we can obtain larger polycrystalline grain domains with a preferred orientation. However, we observe a distinct trade-off between the grain sizes and pinhole density. Since crystal growth not only occurs in the lateral direction, but also in the vertical direction, the formation of grains above 10μm in size tends to be accompanied with undesirable pinholes. Hence, the optimal precursor solution is one that contains a proper colloids concentration in order to provide a pinhole-free film with as large grain morphology as possible. However, it is important to note that this ideal balance depends on the surface energy and roughness of the n or p-type coated substrate. Therefore, the colloidal distribution of the precursor solution can be adjusted for optimum morphology depending on the hydrophobicity of the electron or hole accepting layer that the perovskite will crystallize upon.

In order to understand the impact of this control of thin film growth upon the crystalline quality of the material, we analyze the material quality using two-dimensional X-ray diffraction (XRD^2). By employing image plates or a 2D charged-couple device (CCD) array as detector, this allows us to measure complete Debye-Scherrer cones simultaneously. In contrast to a conventional 1D XRD diffraction profile, we can directly observe the effects of grain size and texture from the 2D diffraction profile. In Figure 39F, we show a series of 2D diffraction patterns of thin films prepared using various precursor solutions. To perform a quantitative analysis, we integrate the intensity along the azimuthal angle over the diffraction pattern arising from the (100) planes that form a Debye–Scherrer ring at ~1 $Å^{-1}$, as we show in Figure 39F and G. We observe that thin films prepared from solutions with high colloid concentrations result in little preference of orientation, where samples exhibited diffraction rings with intensities along the entire arc segment, indicative of fewer crystal domains with preferential orientations. From Figure 39G, we observe three preferential orientations in the orientation distribution, which are located at β = 180°, 127° and 233°. Apart from the β = 180° peak, the origin of the other two peaks can be attributed to the corners of cube-shaped crystallites. Nevertheless, all these peaks exhibit large FWHM values, as we show in Figure 39H, indicating the poor film crystallinity for thin films prepared with large amount of colloids (i.e. without an acid additive). In contrast, we observed significant texturing for thin films prepared from solutions with low amount of colloids. Due to the extended growth period, these thin films exhibit discrete Bragg spots along the identical diffraction ring, indicative of crystal domain orientation. The texturing trend, which we see in the XRD^2, coincides with the trend seen in grain sizes we observe via SEM. Films

prepared with a colloid-free solution and annealed at high temperature, result in XRD[2] diffraction patterns approaching single crystalline quality.

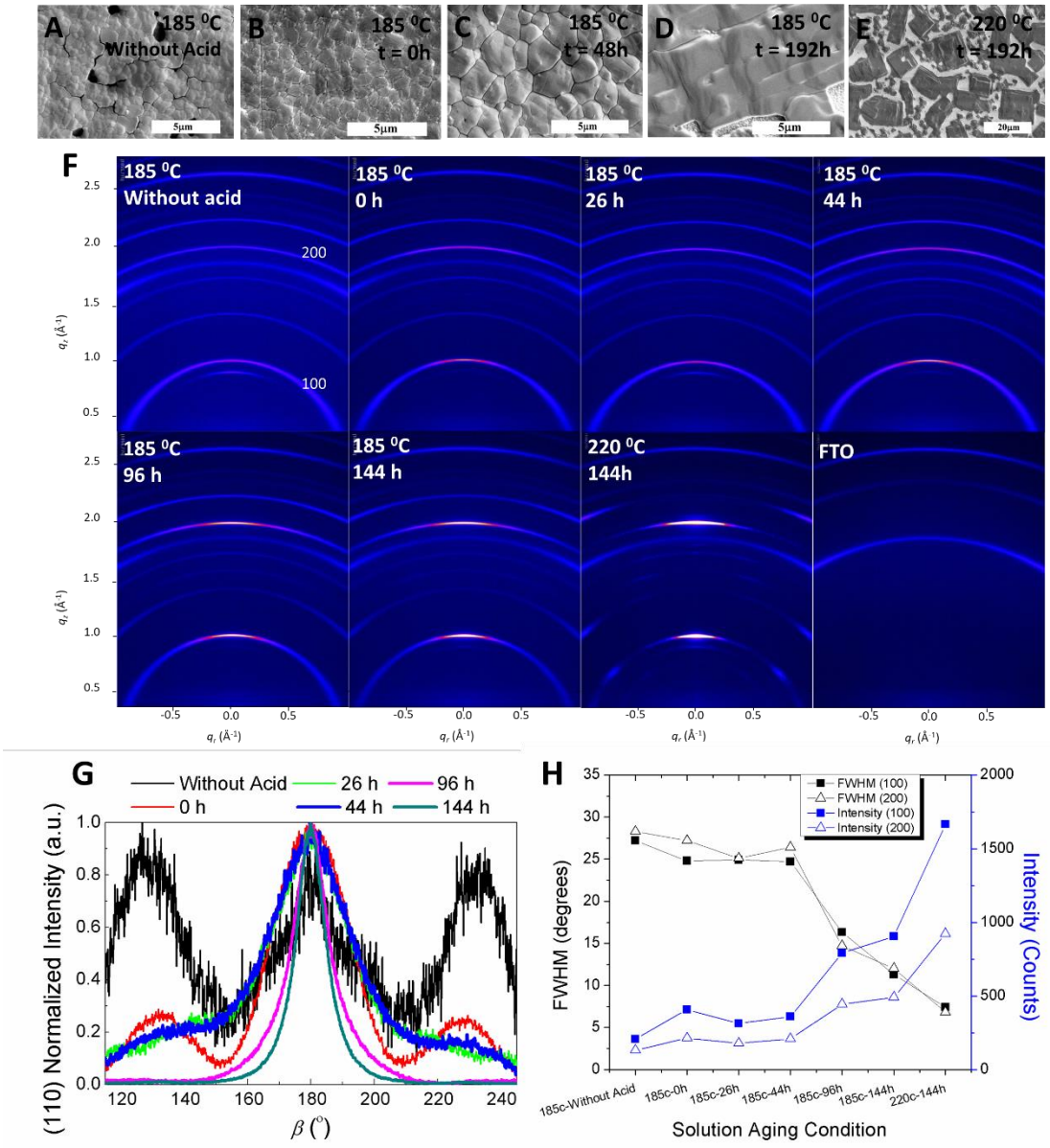


Figure 39: Impact of colloids in the precursor solution on morphology and crystal quality. *A-E) A series of top-view scanning electron microscope (SEM) images of a fully annealed* $FA_{0.83}Cs_{0.17}Pb(Br_{0.2}I_{0.8})_3$ *perovskite thin film prepared with/and without hydrohalic acids, where the solutions were aged for various time periods. F) A series of two-dimensional X-ray diffraction patterns of corresponding thin film after full annealing step. G) Normalized (100) diffraction peak of corresponding perovskite thin film. H) Azimuthal (β) full-width half maximum (FWHM) of (100) and (200) orientation, along with the peak intensity of the (100) and (200) diffraction peak. The two-dimensional X-ray diffraction patterns was measured by Zhiping Wang of the Department of Physics, University of Oxford.*

We further assess the impact of the colloids on crystal quality by conducting a local strain (microstrain) analysis. Different nucleation and crystal growth kinetics of perovskite thin films can be

responsible for variations in microstrain. These small fluctuations in the lattice spacing are induced by the presence of crystal imperfections/structural defects including dislocations, vacancies and stacking faults.[90–92] Here, we quantify the effects of microstrain in our perovskite films by analyzing the peak broadening in the diffraction patterns according to the modified Williamson-Hall method.[91,93,133,153] We show in Figure 40B, a clear reduction in microstrain as we dissolve the colloids in the precursor solution. This allows for a slower crystal growth, minimizing the localized strain within the structure.

In order to characterize the charge carrier mobility in the fully crystalized films, we performed optical-pump terahertz-probe (OPTP) spectroscopy. Figure 40C, we show charge-carrier mobility of the $FA_{0.83}Cs_{0.17}Pb(Br_{0.2}I_{0.8})_3$ perovskite for thin films fabricated with different precursor solutions. We measure more than a twofold increase in charge-carrier mobilities for films processed from solutions with fewer amounts of colloids, from $<10 cm^2V^{-1}s^{-1}$ to $>20 cm^2V^{-1}s^{-1}$. This coincides with the increase in crystallinity and texturing observed in the XRD[2] diffraction patterns and the reduction in microstrain.

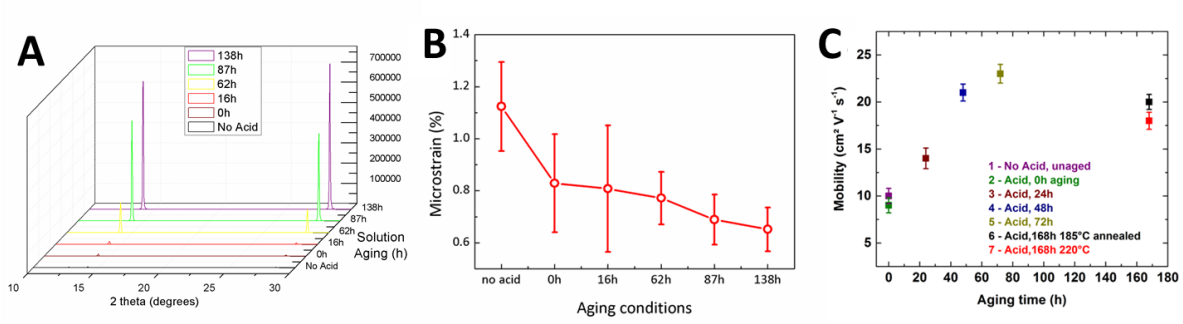


Figure 40: Optoelectronic and crystal properties for $FA_{0.83}Cs_{0.17}Pb(Br_{0.2}I_{0.8})_3$ perovskite prepared with various aging conditions. *A) 1D X-ray diffraction pattern of thin films prepared with various precursor solution. Impact of colloids on crystal lattice and optoelectronics properties. B) Calculated microstrain derived from XRD pattern of samples with different precursor solution aging conditions. C) The effective charge-carrier mobilities, corrected for surface coverage, of a range of perovskite films prepared with precursor solution with various concentrations of colloids. Error bars indicate the range of values obtained. The microstrain was calcualted by Zhiping Wang of the Department of Physics, University of Oxford. The perovskite mobility was measured by Waqaas Rehman of the Department of Physics, University of Oxford.*

We make a specific note about microstrain: microstrain is not a property that is often employed when analyzing perovskite absorbers within the perovskite research community. However, recently several studies, using different perovskite systems, have shown a good correlation between reduced microstrain and enhanced optoelectronic properties[133,154,155]. We suggest that either microstrain itself, or the crystal defects responsible for microstrain, or both are closely related to the defects responsible for negating high optoelectronic quality in these materials. Hence, with respect to

attempting to realize an ideal perovskite semiconductor, minimizing microstrain in the polycrystalline thin-films is likely to be a good metric to assess, and lead to improved optoelectronic quality.

In order to investigate the impact of the differing films in complete solar cells, we fabricated a series of planar heterojunction solar cells using precursor solutions with various colloidal concentrations, the results of which we show in *Figure 41*A. We show the device architecture in *Figure 41*B, consisting of PCBCB [phenyl-C61-butyric acid benzocyclobutene ester], a cross-linkable fullerene derivative,[156,157] acting as the electron-selective layer, $FA_{0.83}Cs_{0.17}Pb(I_{0.8}Br_{0.2})_3$ as perovskite absorber and Li-TFSI–doped [TFSI, bis(trifluoromethanesulfonyl)imide] spiro-OMeTAD [2,2',7, 7'-tetrakis(N,N-di-p-methoxyphenylamine)-9,9'-spirobifluorene] with tBP [4-tert-butylpyridine] additive as the hole-collection layer, capped with a gold cathode. The scanning electron microscope (SEM) cross-section image shows a dense and continuous perovskite film with grain sizes of over 2.5µm. The performance trend is in good accordance with morphology, grain size, crystallinity, microstrain and charge-carrier mobilities. We observe that the optimum device performance is obtained when the solution is aged for approximately two days. We show in Figure 41C the spectral response of a representative $FA_{0.83}Cs_{0.17}Pb(I_{0.8}Br_{0.2})_3$ perovskite solar cells, which yields a current density of 21.5mA cm^{-2}. As shown in Figure 41D, we measured current-density voltage (J-V) characteristics of one of the highest-performing devices under a simulated air mass (AM) 1.5 and 100 mW cm^{-2} of sunlight. This device generated a short-circuit current-density (J_{SC}) of 22.1mA cm^{-2}, a fill-factor (FF) of 0.8, an open-circuit voltage (V_{OC}) of 1.07V, and a power conversion efficiency of 18.8%. Due to the hysteretic behavior of perovskite solar cells, we performed a stabilized efficiency measurement to accurately access the performance of the device. By holding the cell at a fixed maximum power point forward-bias voltage of 0.9V, we measured the power output over time, reaching a stabilized efficiency of 17.9% (Figure 41D).

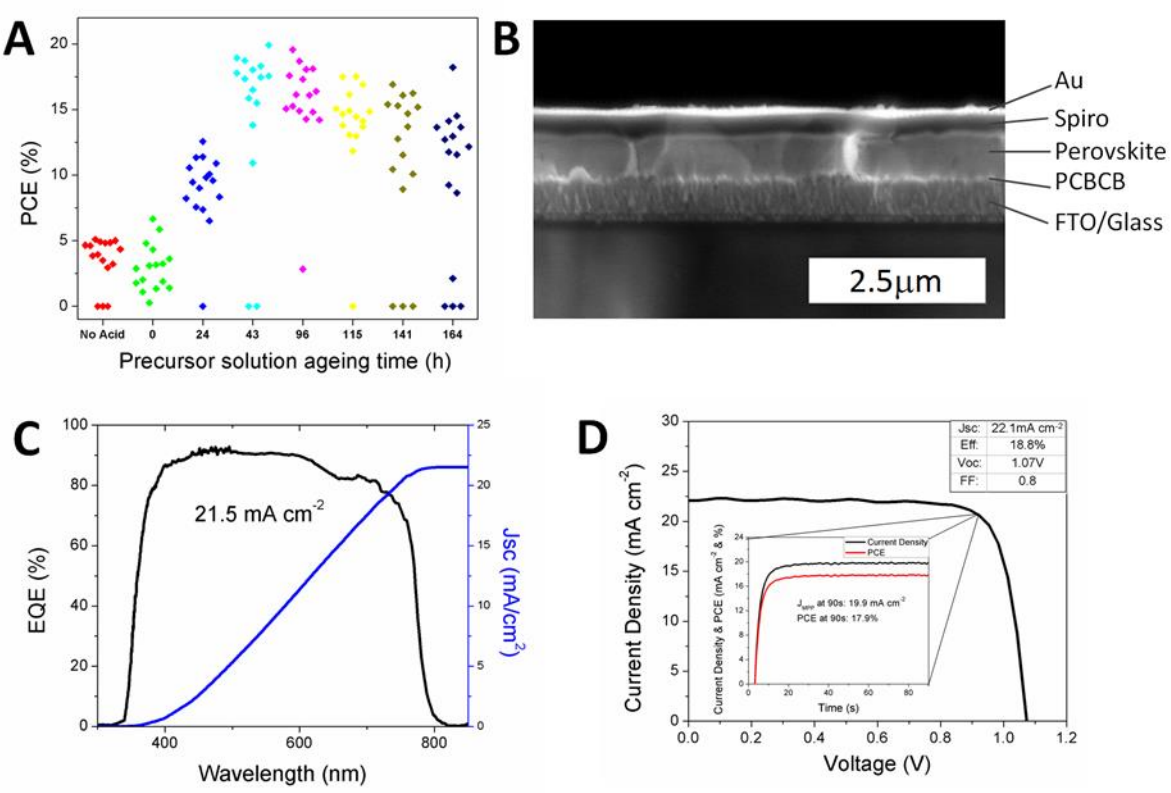


Figure 41: Impact of precursor solution aging time on solar cell device performance. A) Impact of precursor solution aging time on power conversion efficiency. B) Cross-sectional, scanning electron microscope image of a $FA_{0.83}Cs_{0.17}Pb(I_{0.8}Br_{0.2})_3$ planar heterojunction solar cell prepared with a precursor solution aged for 48h using hydrohalic acids C) EQE spectrum measured in short-circuit (J_{SC}) configuration and the integrated current density for the optimized perovskite solar cell. D) Forward bias to short-circuit I-V curve for the best stabilized perovskite device fabricated, measured at a 0.38 V/s scan rate. The inset figure shows the photocurrent density and power conversion efficiency measured at the maximum power point for a 90 s time span.

5.4. Conclusion and outlook

We have established a relationship between the colloid concentration of the precursor solution and the crystal quality and morphology of the perovskite thin film. Hydrohalic acids initiate the dissolution of the lead polyhalide colloids, which appear to act as nucleation sites in the as-cast thin films. We show the clear impact of colloids on the crystal nucleation and growth kinetics of the mixed-cation lead mixed-halide perovskite system. Here, we employed solution aging time as a means to control the size and dispersion of colloids in the precursor solution, which leads to a surprising increase in the grain size, crystallinity and texture. In turn, this improvement in material quality translated in an unexpected two-fold increase in charge-carrier mobility to exceed 20 $cm^2V^{-1}s^{-1}$ and a significant reduction in microstrain. These gains in material and optoelectronic properties lead to a

substantial increase in solar cell devices efficiency, reaching power conversion efficiency of 18.8% and a stabilized efficiency of 17.9%. Further investigation is still needed to identify the mechanisms through which the colloidal dissolution occurs. In addition, it will likely prove to be advantageous to develop means to overcome the trade-off between large grains and uniform pinhole free films.

6. Fully-Solution Processed All-Perovskite Multi-Junction Solar Cells

The work in this chapter has been adapted and reproduced in part with permission from:

David P. McMeekin, Suhas Mahesh, Nakita K. Noel, Matthew T. Klug, JongChul Lim, James M. Ball, Laura Herz, Michael B. Johnston, and Henry J. Snaith

6.1. Context and summary

Multi-junction device architectures can increase the power conversion efficiency of photovoltaic cells beyond the single-junction thermodynamic limit that most currently commercial cells operate within. However, with increased processing complexity, these devices are challenging to produce, particularly by solution-based methods. In this chapter, we demonstrate fully solution-processed, monolithic, all-perovskite tandem and triple-junction solar cells. By employing a highly volatile, low boiling point acetonitrile(CH_3CN)/methylamine(CH_3NH_2) (ACN/MA) solvent-based perovskite system, we show that perovskite junctions can be stacked on one another to create all-solution processed perovskite multi-junction solar cells. By combining $FA_{0.83}Cs_{0.17}Pb(Br_{0.7}I_{0.3})_3$ (1.94 eV) and $MAPbI_3$ (1.57 eV) junctions, we reach monolithic, two-terminal tandem power conversion efficiencies (PCEs) of over 15 % (stabilized), delivering 2.18 V open-circuit voltage. We show that a $MAPb_{0.75}Sn_{0.25}I_3$ (1.34 eV) narrow band gap perovskite material can be processed via an ACN/MA based solvent system. By adding this third narrow-band gap junction and extending the tandem's light absorption to the near-infrared spectrum, we achieve the first proof-of-concept triple-junction perovskite solar cell with an open-circuit voltage of 2.83 V. Through optical and electronic modeling, by integrating our tandem architecture with a state of the art $FA_{0.6}MA_{0.4}Pb_{0.4}Sn_{0.6}I_3$ (1.24 eV), we estimate the conceivable PCE of this triple-junction device architecture to be 26.7%, and show a roadmap to exceed 30% efficiency. Our findings open new possibilities for large-scale, low-cost, printable perovskite multi-junction solar cells.

6.2. Introduction

Metal halide perovskite semiconductors exhibit high performance when integrated in optoelectronic devices such as light-emitting-diodes (LEDs),[66] photo-detectors,[128,129] lasers[158,159] and solar cells.[18,22,23,49,96,97,160,161] These perovskites have a general chemical formula ABX_3 allowing their band gap to be tuned by substituting their chemical constituents, i.e. the A-site cation (methylammonium, formamidinium, cesium), B-site metal cation (lead or tin), or X-site anions (iodide, bromide, chloride). This enables halide perovskite semiconductors to be tuned to absorb specific regions of the solar spectrum,[62,63] and employed in multiple-junction applications, which have the capability of surpassing the Shockley-Queisser[24] and the Tiedje-Yablonovitch thermodynamic efficiency limits.[25] By reducing the difference between the photon energy and the electronic band gap energy, we can effectively minimize charge-carrier thermalization losses, and thus increase the maximum obtainable power conversion efficiency (PCE). In order to reduce the conversion of photon energy into heat, multiple absorber materials with a wide range of band gaps are required. Recently, efficient solar cells employing wide-band gap perovskites have been fabricated by partial substitution of the organic A-site cation with cesium (Cs) to improve their structural, thermal, and light stability.[162–166] Furthermore, narrow band gap materials have also been explored through modifications to the B-site cation, where the partial substitution of lead (Pb) with tin (Sn) results in an anomalous band gap bowing behavior, leading to band gaps approaching 1.2 eV.[64,65,109,167–172]

To date, perovskite solar cells exhibiting record efficiencies have been processed via solution-based fabrication methods, reaching 22.7% in a single junction device.[15,173] The ability to fabricate high quality absorber materials from solution-based processes, in combination with their exceptional optoelectronic properties, has led to the rapid rise of perovskites solar cells. [18,22,23,49,96,97,126,160,161] In recent years, significant breakthroughs have been made in four-terminal (4T)[64,168,174–177] and two-terminal (2T)[64,165,178–180] perovskite-on-silicon,[106,174,175,179,181] perovskite-on-$Cu(In,Ga)Se_2$ (CIGS),[174,176,178] perovskite-on-$Cu_2ZnSn(S,Se)_4$ (CZTSSe)[178] and also perovskite-on-perovskite[64,165,168,177,180,182,183] tandem cells. Tandem solar cells require a semi-transparent electrode and/or recombination layers between each sub-cell, which can be fabricated using a variety of materials and processing methods. These highly conductive transparent layers have been fabricated using silver nanowires (Ag-NWs),[174], N4,N4,N4",N4"-tetra([1,1'-biphenyl]-4-yl)-[1,1':4',1"-terphenyl]-4,4"-diamine doped 2,2'-(perfluoronaphthalene-2,6-diylidene) dimalononitrile (TaTm:F_6-TCNNQ),[180] poly(3,4-ethylenedioxythiophene) polystyrene sulfonate (PEDOT:PSS),[182,184] aluminum doped zinc oxide (AZO)[176], and most notably indium tin oxide (ITO)[106,165,168,177–179,181,185]. These materials can also

be processed using different deposition techniques such as: spray-coating,[174] film transfer lamination,[184] vacuum deposition[180], and sputter coating[106,165,168,176,178,179,181,185]. Sputtered ITO has gained considerable attraction due to its high optical transparency throughout the visible and near-infrared (NIR) region, combined with a low resistivity. [186] Due to its dense and compact nature, this sputtered transparent conductive oxide (TCO) can also serve as a physical barrier to the solvents which are used to process the subsequent material layers. Specifically dimethyl formamide (DMF) and dimethyl sulfoxide (DMSO), both strongly coordinating solvents used in the dissolution of perovskite salts. These solvents rapidly re-dissolve any underlying perovskite layers unless they are protected by a dense pin-hole free layer, such as indium oxide tin oxide (ITO). As recently shown by Eperon, Leijtens et al., monolithic all-perovskite tandem cells, with power conversion efficiencies (PCEs) of over 17%, can be fabricated using this dense, sputtered ITO layer.[64] However, the re-dissolution problem has thus far prevented any experimental realization of an all-solution-processed multi-junction perovskite solar cell, without employing sputter coated ITO.[64] These sputter coated TCOs usually require high vacuum deposition systems and dense buffer layers comprised of nanoparticle (NP) or atomic layer deposition (ALD) layers to prevent the organic and perovskite layers from sputter damage. Furthermore, the lower refractive index of ITO, in comparison to the perovskite absorber layers, introduces significant internal reflective losses, thus limiting the maximum feasible power conversion efficiency.[85]

Herein, we employ an acetonitrile/methylamine (ACN/MA) composite solvent, which was previously introduced by Noel et al.,[76] to enable the sequential processing of perovskite absorber layers upon underlying perovskite devices. This all-solution processed architecture has the potential of being applied to the manufacturing of large area films on both rigid and flexible substrates, using deposition techniques such as roll-to-roll (R2R) processing, blade coating or inkjet printing. In turn, we present an all-solution processed tandem architecture, reaching over 15% stabilized power conversion efficiency (PCE), which delivers 2.18 V open circuit voltage (V_{oc}). Furthermore, we show that the mixed-metal Sn/Pb perovskite $MAPb_{0.75}Sn_{0.25}I_3$, can also be processed via the ACN/MA solvent system, where the reducing nature of MA obviates the need to use SnF_2 to achieve respectable efficiencies, allowing us to obtain a scanned PCE of over 11% (stabilized 10.5%), employing an n-i-p architecture. Using a mixed-metal $MAPb_{0.75}Sn_{0.25}I_3$ perovskite material to extend the light absorption of the multi-junction to 925 nm, we present the first monolithic triple-junction perovskite solar with an open circuit voltage (V_{oc}) of 2.83 V. We utilize an optical and electronic model to validate our experimental results, and reveal the optical losses existing within this specific architecture. We then proceed to model a triple junction perovskite solar cell, using electronic characteristics of currently feasible 1.94/1.57/1.24

eV perovskite materials, showing the possibility of achieving a triple junction device with a 26.7% PCE and corresponding V_{OC} of 3.16 V.

6.3. Results and discussion

All-perovskite monolithic 2T tandems and multi-junction solar cells require a tunnel junction (TJ) or recombination layer to provide a means to create an electronic series connection between the different sub-cells. In turn, the photo-voltage generated from each sub-cell sum, resulting in high voltage devices. However, due to charge conservation, the current density flowing out of each sub-cell must match, and hence the current will be limited by the lowest current density generated from any sub-junction. Thus, in order to maximize the photocurrent density in a 2T monolithic tandem, both sub-cells should generate equal current density, which can be achieved through carefully tuning the band gap and thickness of each junction. Recombination layers between the sub cells must fulfill stringent requirements. Firstly, they must enable ohmic contact to the charge extraction layers, and facilitate recombination of collected electrons and holes without introducing resistive losses. Secondly, they must be as optically transparent as possible to avoid parasitic absorption of light. Thirdly, deposition of the recombination layer should not damage any of the layers beneath, which is typically achieved via introducing "buffer layers" when sputtering, or by using orthogonal solvents for solution processing. Lastly, this interlayer must be a sufficient barrier to solvent penetration to prevent any re-dissolution of underlying perovskite or other electronic layers when subsequently processing another perovskite layer.

Here, we develop a recombination layer and an n-i-p perovskite solar cell architecture that meets these constraints. For the recombination layer, we find that a combination of a PEDOT:PSS layer followed by a ITO nanoparticles layer works well. In the first instance we develop a wide-band gap, purely lead-based perovskite tandem cell by processing a ~1.94 eV top cell on top of 1.57 eV bottom cell. We show in Figure 42 the bang gap as determined by a Tauc plot, along with the device performance of a single junction.

We process the wide band-gap junction first, and hence do not have to overtly consider solvent orthogonality issues. We therefore follow a conventional solution processing route and fabricate $FA_{0.83}Cs_{0.17}Pb(Br_{0.7}I_{0.3})_3$ with 2% (molarity with respect to the Pb) potassium (K^+) additive.[187–191] As we have previously described, we employed a deposition technique utilizing hydrohalic acidic additives to fabricate highly ordered perovskite materials with grains reaching micron sizes in

diameter. Highly crystalline perovskite materials with low energetic disorder have been shown to suppress halide segregation.[103] Furthermore, as recent reports suggest,[187–190,192] we utilize potassium as an additive to suppress ionic migration and reduce the anomalous hysteretic behavior intrinsically present in perovskite solar cells.[193] For this absorber material, in single junction perovskite solar cells, we obtain open-circuit voltages of up to 1.27 V and a stabilized power conversion efficiency of 10.9 %, which we show in Figure 42C. However, although our open-circuit voltages are higher, compared to other ~1.75 eV materials,[142] we note that the voltage losses, with respect to the band gap energy, are greater for this bromide-rich wide-band gap material. Hence, additional efforts may be required to further increase open-circuit voltages and minimize non-radiative losses.

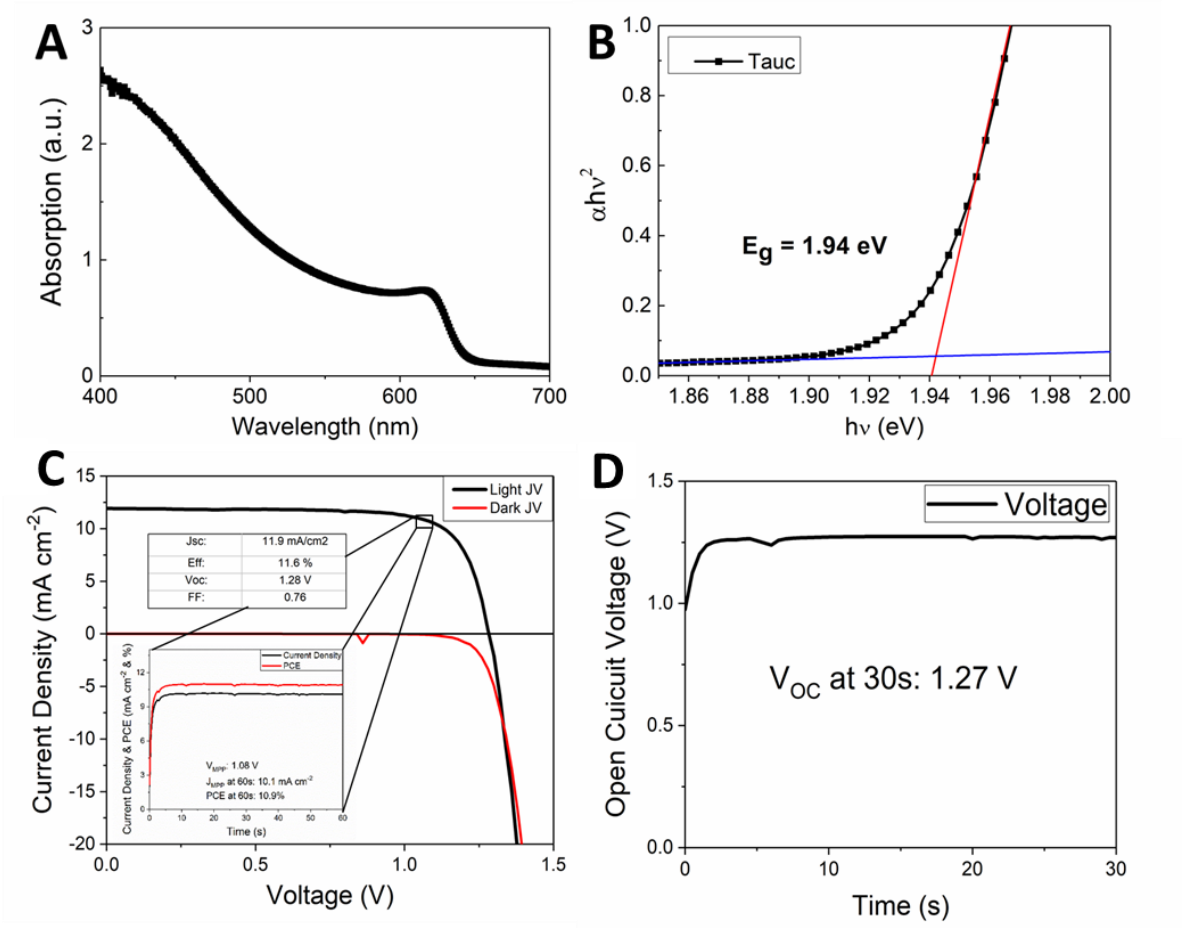


Figure 42: Optical characterization of $FA_{0.83}Cs_{0.17}Pb(Br_{0.7}I_{0.3})_3$ perovskite material with 2% potassium additive and current-voltage characteristic of a SnO_2/PCBM/$FA_{0.83}Cs_{0.17}Pb(Br_{0.7}I_{0.3})_3$/Spiro-OMeTAD perovskite solar cell with 2% mol. potassium (K^+) additive. *A) Absorption spectrum of $FA_{0.83}Cs_{0.17}Pb(Br_{0.7}I_{0.3})_3$ measured with an integration sphere. B) Tauc plot of $FA_{0.83}Cs_{0.17}Pb(Br_{0.7}I_{0.3})_3$ perovskite assuming direct band gap material and fitting of optical band gap from intercept. C) Forward bias to short-circuit current-voltage curve measured under simulated air-mass (AM) 1.5 100 mW cm^{-2} sun light using a 0.25V/s scan rate. The inset figure shows the photocurrent density and*

power conversion efficiency measured at the maximum power point for a 60s time span. D) Stabilized open circuit voltage (V_{oc}) of $FA_{0.83}Cs_{0.17}Pb(Br_{0.7}I_{0.3})_3$ heterojunction perovskite solar cell.

For the bottom cell, which is processed on top of the wide-gap cell, we must consider the issue of dissolution of the underlying perovskite film. If we simply employ one of the standard DMF/DMSO solvent based routes, we completely solvate and discolor the underlying perovskite film, making it evident that our recombination layer is not impermeable to DMF or DMSO. These high boiling point solvents remain on the surface long enough to slowly percolate through solution-processed interlayers, re-dissolve the underlying perovskite layer, thus limiting their usefulness in all-solution processed tandem solar cells. We have previously developed an ACN/MA based composite solvent system for processing perovskite films, which has several distinct advantages.[194] Firstly, it is much more volatile than DMF, enabling very rapid drying. Secondly, the solvation strength can be tuned by varying the amount of methylamine incorporated. We chose the right amount of MA to enable complete dissolution of the salts, but with minimal excess. We found that having an excess amount of MA in solution can have a detrimental impact to the device. Unwanted pinholes in the interlayers may result in methylamine percolating and re-dissolving the perovskite underlayer. Thus, by carefully tuning the MA content in our solutions to obtain a solution at its critical solubility point, we minimize the chance of re-dissolving the underlayer. We find this solubility point by slowly adding a ACN/MA perovskite solution to a neat ACN perovskite dispersion, until the mixture becomes a full perovskite solution. Through this route, we were able to obtain a robust and reliable protocol for fabrication of all-perovskite multi-junction solar cells.

To achieve optimal results, careful tuning of the B-site metal ion content was needed for both $MAPbI_3$ and $MAPb_{0.75}Sn_{0.25}I_3$ perovskite materials processed via the ACN/MA solvent route. In Figure 43A, we show a series of scanning electron microscope (SEM) top view images of an $MAPbI_3$ perovskite film, processed with the ACN/MA solvent system, various non-stoichiometric compositions fabricated on top of the $FA_{0.83}Cs_{0.17}Pb(Br_{0.7}I_{0.3})_3$ top-cell (TC) on a phenyl-C_{61}-butyric acid methyl ester ($PC_{61}BM$) layer. The effects of the non-stoichiometric perovskite precursor solutions have been previously discussed,[195–199] however the research community has yet to agree on which precise non-stoichiometry is ideal. Some studies have shown that excess organic ammonium, leads to performance gains, while other studies showed the benefits of having excess PbI_2 in the precursor solution. However, it is clear that these small stoichiometric changes do impact the perovskite in various ways, ranging from effects on morphology,[196] luminescence [197], trap passivation[198] and stability.[199]

In Figure 43A we show a series of top-view SEM images with various A-site to B-site compositional tuning of the ACN/MA precursor solution, when processed on top of the existing solar cell, ranging from 6% excess MAI to 6% excess PbI_2. We observed an impact on the morphology and surface coverage for precursor solutions with different compositions. In an all-solution processed tandem architecture, it is imperative to eliminate the presence of pinholes, to prevent dissolving underlying layers. We find that the ideal composition for maximizing the single junction cell efficiency includes 3% excess MAI, and proceed to fabricate complete tandem solar cells with this composition. In Figure 43B and Figure 43C, we show a schematic of a 2T tandem along with a corresponding scanning electron microscopy SEM cross-section image. We fabricate the solar cells in the conventional n-i-p architecture, and find that a recombination layer composed of PEDOT:PSS followed by indium tin oxide (ITO) nanoparticles works remarkably well, sandwiched between a 2,2',7,7'-tetrakis(N,N'-di-p-methoxyphenylamine)-9,9'-spirobifluorene (spiro-OMeTAD) p-type charge extraction layer and n-doped $PC_{61}BM$ electron transporter.

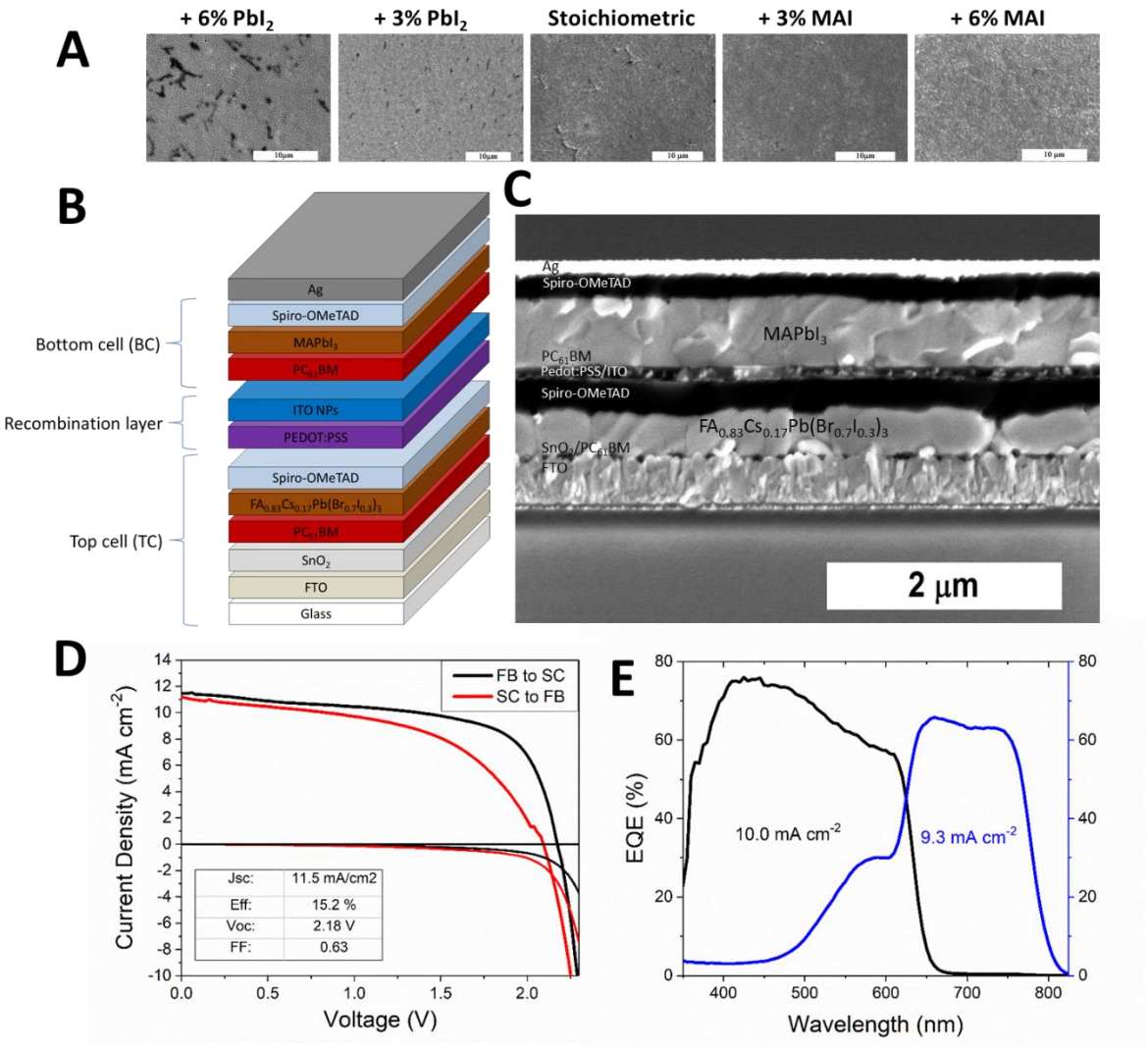
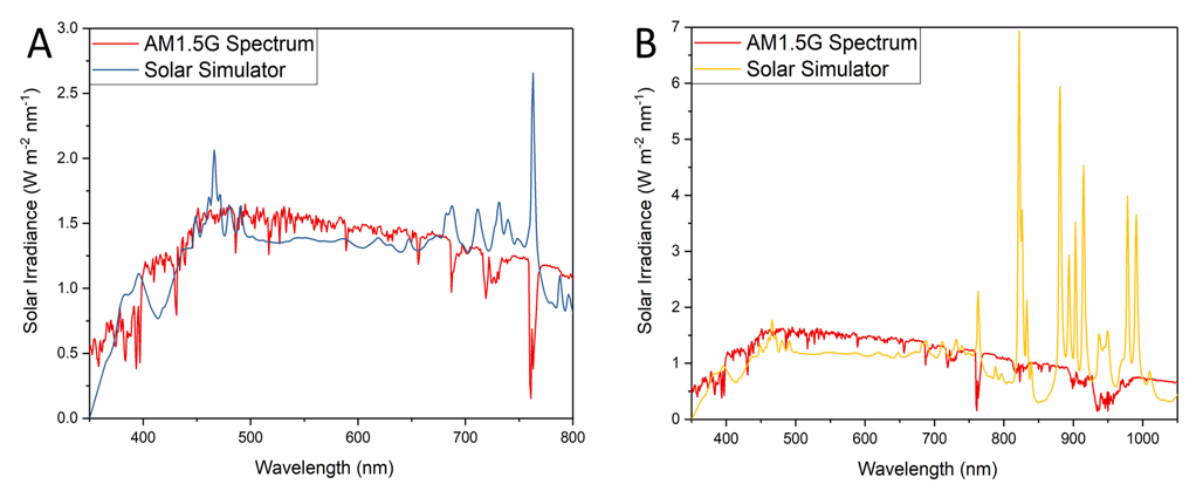


Figure 43: Two-terminal (2T) $FA_{0.83}Cs_{0.17}Pb(Br_{0.7}I_{0.3})_3/MAPbI_3$ tandem perovskite solar cells. *A) Scanning electron microscopy (SEM) image of the top view of $MAPbI_3$ thin film deposited on top of the top-cell (TC) and interlayer, prepared using an acetonitrile(CH_3CN)/methylamine(CH_3NH_2) (ACN/MA) solvent system, ranging from excess 6% PbI_2 to excess 6% MAI. B) Schematics showing an all-solution processed perovskite/perovskite two-terminal (2T) tandem perovskite solar cell. Incoming light will be from below the device. C) SEM cross-section of the 2T perovskite/perovskite tandem. D) J-V characteristics for the champion $FA_{0.83}Cs_{0.17}Pb(Br_{0.7}I_{0.3})_3/MAPbI_3$ tandem heterojunction solar cell, with an equivalent irradiance of 100.4mW cm^{-2}, measured at a 0.25 V/s scan rate. E) EQE spectrum for each sub-cell, and the integrated current density for the tandem perovskite solar cell.*

In Figure 43D, we show the forward and backwards current-density voltage (J-V) characteristics of one of our highest-performing two-terminal tandem solar cells measured under a simulated air mass (AM) 1.5 solar irradiation with a power density of 100.4 mW cm^{-2}. In this work, the recombination layer comprises PEDOT:PSS and indium tin oxide (ITO) nanoparticle (NP) sublayers. We

dilute a high conductivity PEDOT:PSS (Heraus H1000) solution with isopropanol (IPA) and directly spin-coat on the spiro-OMeTAD layer, which acts as both a recombination layer and solvent barrier. We then spin-coat on an ITO layer from a solvent dispersion of ITO nanoparticles (>100nm). The fabricated ITO nanoparticle layer may be porous and non-continuous. However, these nanoparticles, improve the recombination process, due to their high carrier density, which allow holes from PEDOT:PSS and electrons from $PC_{61}BM$ to recombine. The ITO NP layer creates an ohmic contact between both electron and hole-accepting layers, which allows for efficient charge transfer into the recombination layer. This tandem device generated a short-circuit current-density (J_{SC}) of 11.5 mA cm^{-2}, a fill-factor (FF) of 0.63, an open-circuit voltage (V_{oc}) of 2.18 V, and a power conversion efficiency of 15.2% (stabilized). Perovskite solar cells have been prone to hysteretic behavior.[193] Hence, we performed a stabilized efficiency measurement by holding the device at a fixed maximum power point voltage of 1.72 V, reaching a stabilized efficiency of 15.2%. We show in Figure 43E an external quantum efficiency (EQE) of both junctions, with an integrated current density of 10.0 mA cm^{-2} for the top cell and 9.3 mA cm^{-2} for the bottom cell. During the EQE measurement, we applied a voltage bias to the solar cell equal to the V_{oc} of the optically biases sub-cell. This allowed for the EQE to be measured near J_{sc}. We note a slight current-density mismatch between the two sub-cells.

In Figure 44C, we show the calculated mismatch factor for each material used in the multi-junction solar cell. We note that the xenon arc lamp spectrum can be significantly mismatched with the AM1.5G spectrum due to the large intensity spikes in the infrared portion of the spectrum (shown in Figure 44A and B). As a result, specific sub-cells of the multi-junction solar cell may be over or underestimated, especially in the case of multi-junction solar cells. In this specific case here, our tandem cell is bottom cell limited under AM1.5G spectrum, and top cell limited under the solar simulator lamp. To account for these discrepancies, we applied a mismatch factor correction, which corrected our estimated efficiency by approximately -0.4% relative. However, in the case of the triple-junction, a significant mismatch factor arises due to the xenon intensity spikes, which requires a correction of -48.6% in efficiency to account for this mismatch factor. Both correction factors have been applied to the reported efficiencies. Hence, our irradiances are 100.4 mW cm^{-2} and 148.6 mW cm^{-2} for the tandem and triple-junction solar cell, respectively.



C

Architecture	Uncorrected mismatch factor	Mismatch factor after lamp adjusted	Filter for Reference cell
Tandem solar cell	1.050	1.004	KG5
Triple-junction solar cell	1.507	1.486	KG2

Figure 44: Measured solar simulator spectrum compared to the AM1.5G spectrum. *A) Xenon lamp spectrum used for the measurement of the $FA_{0.83}Cs_{0.17}Pb(Br_{0.7}I_{0.3})_3$/$MAPbI_3$ tandem solar cell B) Xenon lamp spectrum used for the measurement of the $FA_{0.83}Cs_{0.17}Pb(Br_{0.7}I_{0.3})_3$/$MAPbI_3$/$MAPb_{0.75}Sn_{0.25}I_3$ triple-junction solar cell C) Table of the calculated mismatch factors for the tandem perovskite solar cell and the triple-junction perovskite solar cell. The solar irradiance spectra were measured by Matt Klug of the Department of Physics, University of Oxford.*

Estimation of voltage losses is a critical metric to access the quality of the recombination interlayers. Using a PEDOT:PSS/ITO NPs interlayers as the recombination layer, we measured a 2T tandem V_{oc} as high as 2.22 V, resulting in a interlayer voltage loss of approximately 150mV, if we assume both sub-cells generated the highest measured single junction V_{oc} of 1.27 V for the top cell and 1.11V for the bottom cell.

Although neat lead-based devices have led to stable perovskite materials, the drive to narrow the bandgap using less stable tin-based perovskites is still highly desirable for tandem applications. As shown in Figure 45, we also studied the impact of non-stoichoimetric precursor solutions on the material properties of the $MAPb_{0.75}Sn_{0.25}I_3$ (with a band gap of 1.34 eV determined from Tauc plots) by tuning the A-site to B-site ratio. In order to keep the intended $MAPb_{0.75}Sn_{0.25}I_3$ perovskite composition, we added excess PbI_2 and SnI_2 at a ratio of 75 to 25. In Figure 45A we show kelvin probe force microscopy (KPFM) images, and observe a stark increase in work function as we incorporate excess metal ions in the $MAPb_{0.75}Sn_{0.25}I_3$ perovskite precursor solution. We also notice slower time-

resolved photoluminescence (PL) decays, which we show in Figure 45B. In Figure 45C we present the transient photo-conductivity for the corresponding samples for a range of excitation densities, measuring maximum perturbation of conductivity decay after photoexcitation by a laser pulse.[200] Similarly, we observe an increase in photo-conductivity for films with excess metals ions, implying higher effective mobility.

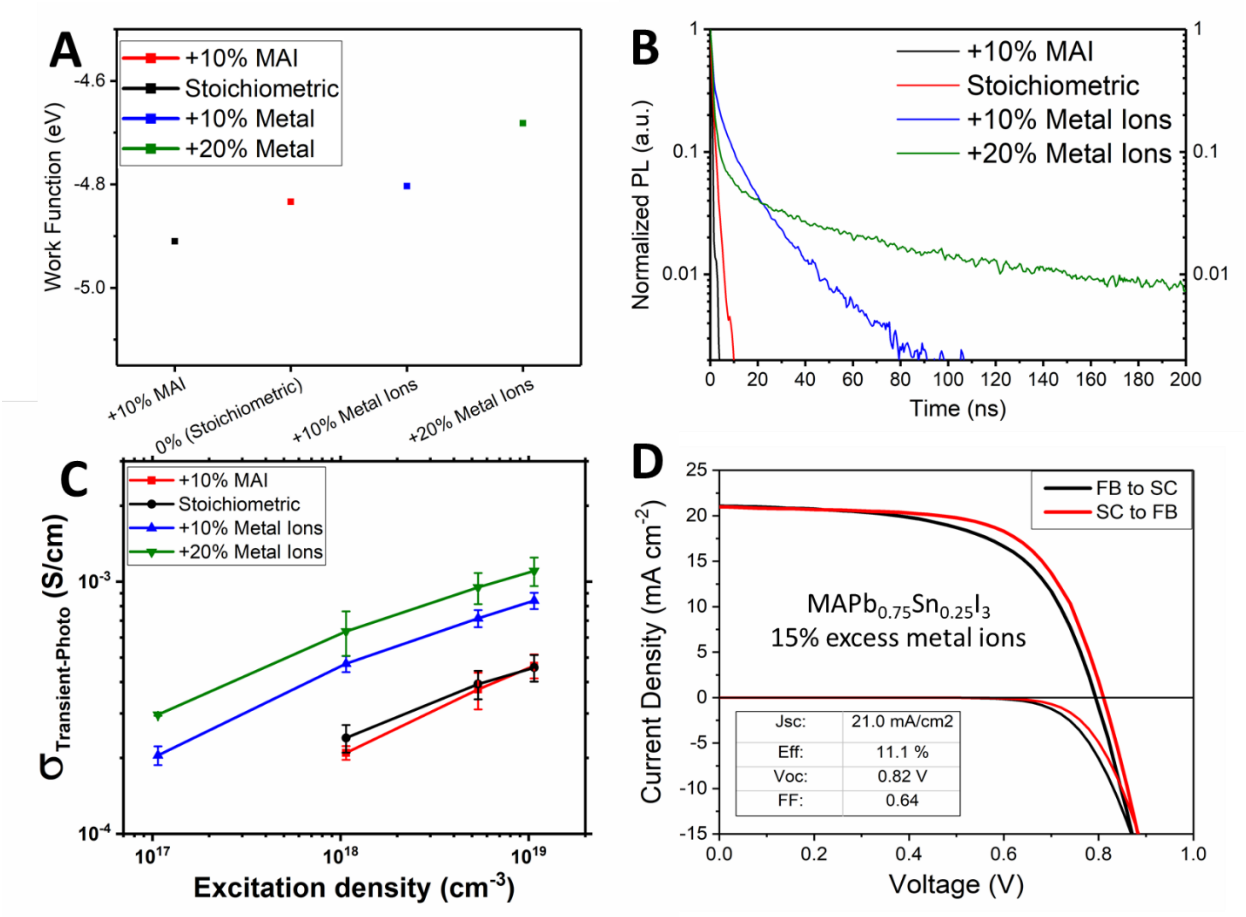


Figure 45: Impact of varying the composition of A to B-site cations for ACN processed $MAPb_{0.75}Sn_{0.25}I_3$ perovskite materials. *A) Kelvin-probe measurement of varying A to B-site stoichiometry B) Normalized time-resolved PL measurements taken at the peak emission wavelength of varying A to B-site stoichiometry C) Impact of A to B-site stoichiometry on the transient photocurrent. D) J-V characteristics of an optimized $MAPb_{0.75}Sn_{0.25}I_3$ single-junction heterojunction solar cell with 15% excess metal ions, measured at a 0.25 V/s scan rate.*

We find that these longer-lived carrier lifetimes and higher photo-conductivities correlate to a substantial increase in device performance, which results in an optimized $MAPb_{0.75}Sn_{0.25}I_3$ PCE of over 11%, as we show in Figure 45D. Surprisingly, we found a substantial difference in optimum A-site

to B-site ratio for tin-lead based perovskite materials compared to neat lead-based perovskites. In the case of Sn/Pb-based perovskite, the research community appears to have consistently observed performance gains when using an excess of tin halides, most notably in the form of tin fluoride (SnF_2)[177,201–204] or tin chloride ($SnCl_2$)[201]. The tin fluoride as an additive has readily been used as a reducing agent with the aim of suppressing the tin oxidation from Sn^{2+} to Sn^{4+}. By suppressing oxidation, we limit Sn^{2+} vacancies, which causes the undesirable p-type behavior found in Sn-based perovskites. In our study here, we rely on MA to act as a reducing agent instead of SnF_2, since SnF_2 poorly dissolves in the ACN/MA solvent system. Amines have been known to act as reducing agents, a phenomenon most often exploited in the synthesis of metal nanoparticles.[205] Here, we exploit the reducing properties of amines, allowing us to effectively replace SnF_2 with MA. We show in Figure 46 a plot of non-optimized devices with various ratios of A-site to B-site cations.

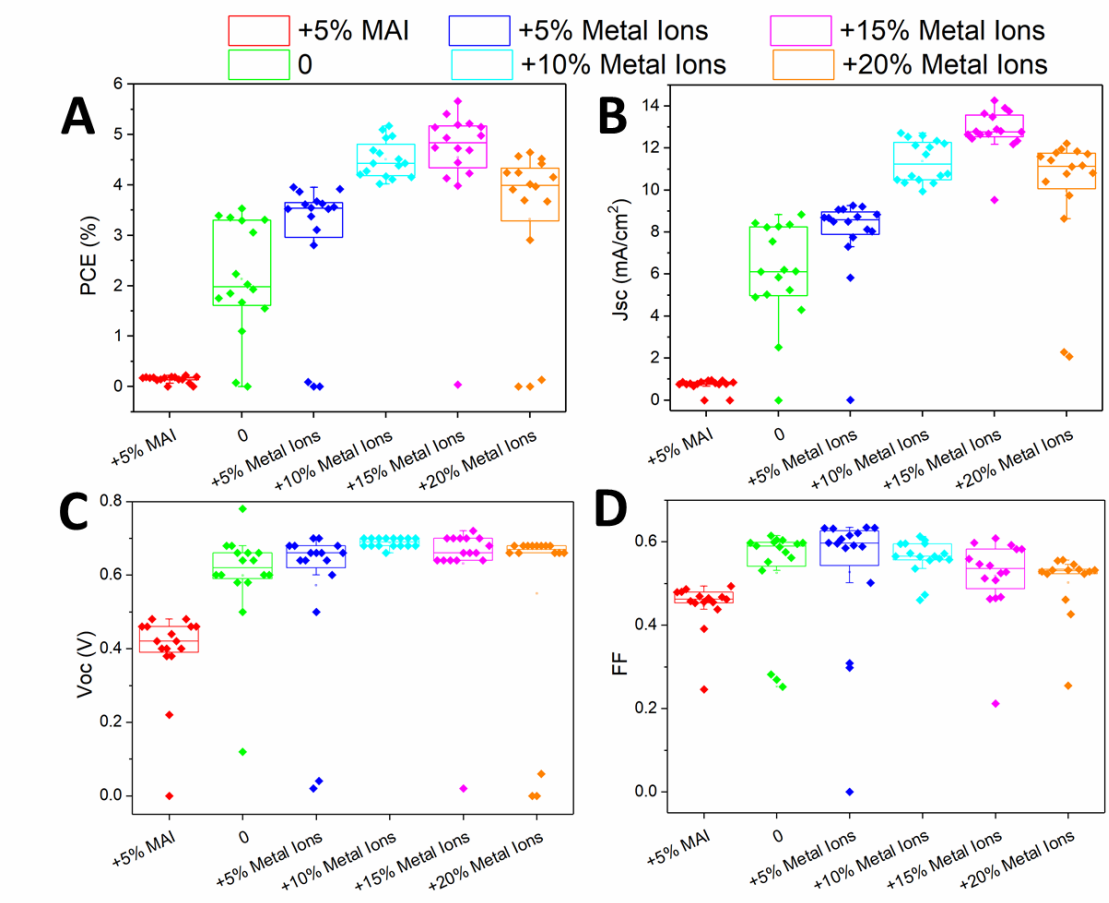


Figure 46: Impact of varying the composition of A to B-site cations of the ACN/MA $MAPb_{0.75}Sn_{0.25}I_3$ single junction perovskite system *on A) power conversion efficiency B) fill-factor C) short-circuit current density D) open-circuit voltage.*

We find that devices with excess MAI produced near-zero PCE and little to no short-circuit density (Jsc), whereas devices with excess amounts of metals ions clearly show an increase in single junction device efficiency, reaching an optimum composition with 15% excess metal ions. Thus, tin-based perovskites not only require a reducing agent to suppress Sn^{+2} to Sn^{+4} oxidation, but also require excess metal ions for optimum performance. This is in agreement with the findings by Song et al., who observed that a non-stoichiometric $CsSnI_3$ perovskite composition of 0.4:1 of CsI:SnI_2 was required for optimum performance when processed under a reducing hydrazine atmosphere.[206] Excess SnI_2 was identified for its role as a "compensator" salt to substitute any Sn^{2+} vacancies that occur as a result of exposure to moisture or oxygen, where Sn^{2+} losses two electrons to become Sn^{4+}. In Figure 45A, we notice a deeper Fermi level for the $MAPb_{0.75}Sn_{0.25}I_3$ perovskite with MAI rich compositions, which is consistent with a higher concentration of Sn^{2+} vacancies, which are expected to lead to p-doping of the perovskite. In contrast, the shallower Fermi levels, which we observed for metal ion rich perovskite films, would correspond to a more intrinsic perovskite material, indicative of fewer Sn^{2+} vacancies. We interpret the increase in carrier lifetimes in the perovskite absorber, which we observe in Figure 45A, to be consistent with and indicate a transition from a highly p-type material to a more intrinsic semiconductor. Furthermore, this change in Fermi level can potentially induce an energetic barrier between the perovskite and the electron or hole accepting layers, in this case, $PC_{61}BM$ and spiro-OMeTAD doped with spiro- $OMeTAD^+$ bis(trifluoromethanesulfonyl)$imide^-$ which we will abbreviate to spiro$(TFSI)_2$, respectively.

In Figure 47, we show the structure and performance characteristics of the first all-perovskite, monolithic, triple-junction solar cell, prepared via a solution processed route. The narrow band gap $MAPb_{0.75}Sn_{0.25}I_3$ perovskite solar cell, described in Figure 45, was processed on top of the dual-junction tandem solar cell architecture described in Figure 43 to fabricate a triple-junction solar cell that absorbs light out to 925 nm. In Figure 47A, we show a schematic of the 2T triple-junction cell comprised of $FA_{0.83}Cs_{0.17}Pb(Br_{0.7}I_{0.3})_3/MAPbI_3/MAPb_{0.75}Sn_{0.25}I_3$, where the $FA_{0.83}Cs_{0.17}Pb(Br_{0.7}I_{0.3})_3$ perovskite is acting as a top-cell, the $MAPbI_3$ perovskite is the middle cell, and the $MAPb_{0.75}Sn_{0.25}I_3$ perovskite is the bottom cell. In Figure 47B we show a corresponding SEM cross-section image. In Figure 47C, we show the forward and backward current-density voltage (J-V) characteristics of one of the "highest-performing" two-terminal triple-junction solar cells measured under 100 mW cm^{-2} simulated air mass (AM) 1.5 and solar irradiation. We measured a PCE of 6.7% (6.4% stabilized), while the highest V_{oc}, which we show in Figure 47D, was measured on a separate device and exhibits a stabilized open-circuit voltage of 2.83 V after 60s.

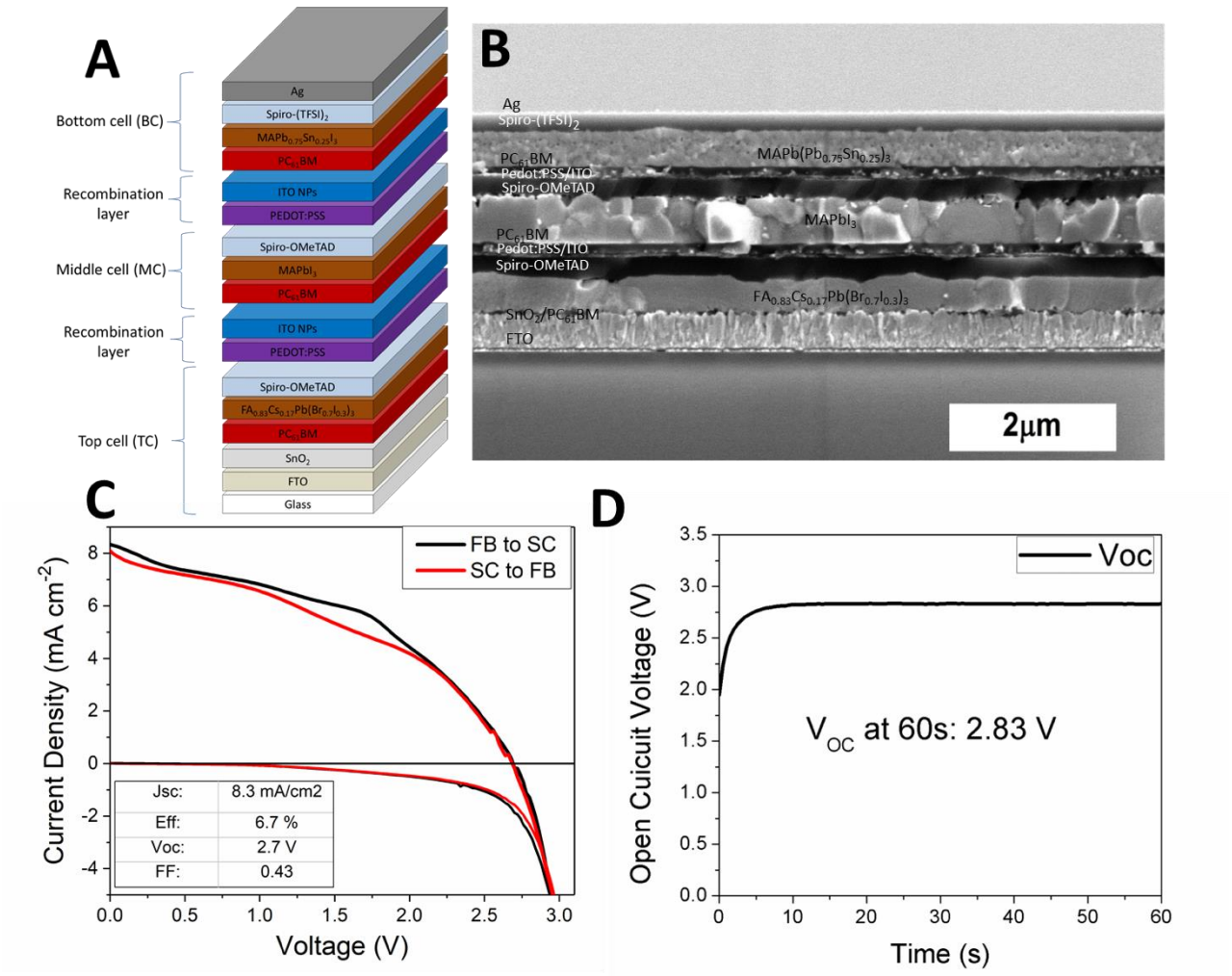


Figure 47: $FA_{0.83}Cs_{0.17}Pb(Br_{0.7}I_{0.3})_3/MAPbI_3/MAPb_{0.75}Sn_{0.25}I_3$ triple-junction perovskite solar cells. *A) Schematics showing an all-solution processed triple-junction two-terminal (2T) perovskite solar cell. Incoming light will be from bellow the device. B) SEM cross-section of the triple-junction 2T all-perovskite tandem. C) J-V characteristics for the champion $FA_{0.83}Cs_{0.17}Pb(Br_{0.7}I_{0.3})_3/MAPbI_3/MAPb_{0.75}Sn_{0.25}I_3$ triple-junction heterojunction solar cell fabricated, with an equivalent irradiance of 148.6 mW cm^{-2}, measured at a 0.25 V/s scan rate. D) Stabilized open circuit voltage (V_{oc}) of triple-junction heterojunction perovskite solar cell measured over a 60s time span.*

We note that the performance of the triple-junction is inferior to that of the double-junction solar cell due to the lower than anticipated short-circuit current-density generated by the $MAPb_{0.75}Sn_{0.25}I_3$ bottom cell. This low photo-generated current is responsible for severely current limiting the entire multi-junction. In *Figure 48*, we show a high performing $FA_{0.83}Cs_{0.17}Pb_{0.5}Sn_{0.5}I_3$ perovskite in a p-i-n architecture, processed with a DMF/DMSO solvent, filtered with a $FA_{0.83}Cs_{0.17}Pb(Br_{0.7}I_{0.3})_3/MAPbI_3$ tandem solar cell without the Ag electrode. Although we note this is not a four-terminal (4T) tandem measurement since we did not employ a semi-transparent electrode

upon the top tandem stack, this measurement allows us to roughly estimate the expected efficiency gain if higher performances and lower band gaps were obtained with ACN/MA solvent system route. As we show in *Figure 48*C, a junction based on $FA_{0.83}Cs_{0.17}Pb_{0.5}Sn_{0.5}I_3$ with a 1.22 eV absorption onset, 15.5% PCE (stabilized) can be obtained when unfiltered and 2.4% PCE (stabilized) when filtered with the $FA_{0.83}Cs_{0.17}Pb(Br_{0.7}I_{0.3})_3/MAPbI_3$ tandem. Thus, a narrow band gap material could potentially boost the $FA_{0.83}Cs_{0.17}Pb(Br_{0.7}I_{0.3})_3/MAPbI_3$ by more than 2.4%, reaching 17.5% PCE. We also note that this measurement includes an air gap between the tandem and the narrow bandgap single-junction solar cell, and an additional PEDOT:PSS layer which would otherwise not be present in the standard monolithic triple-junction solar cell. For these reasons we measure a lower integrated current density from the EQE, shown in *Figure 48*B.

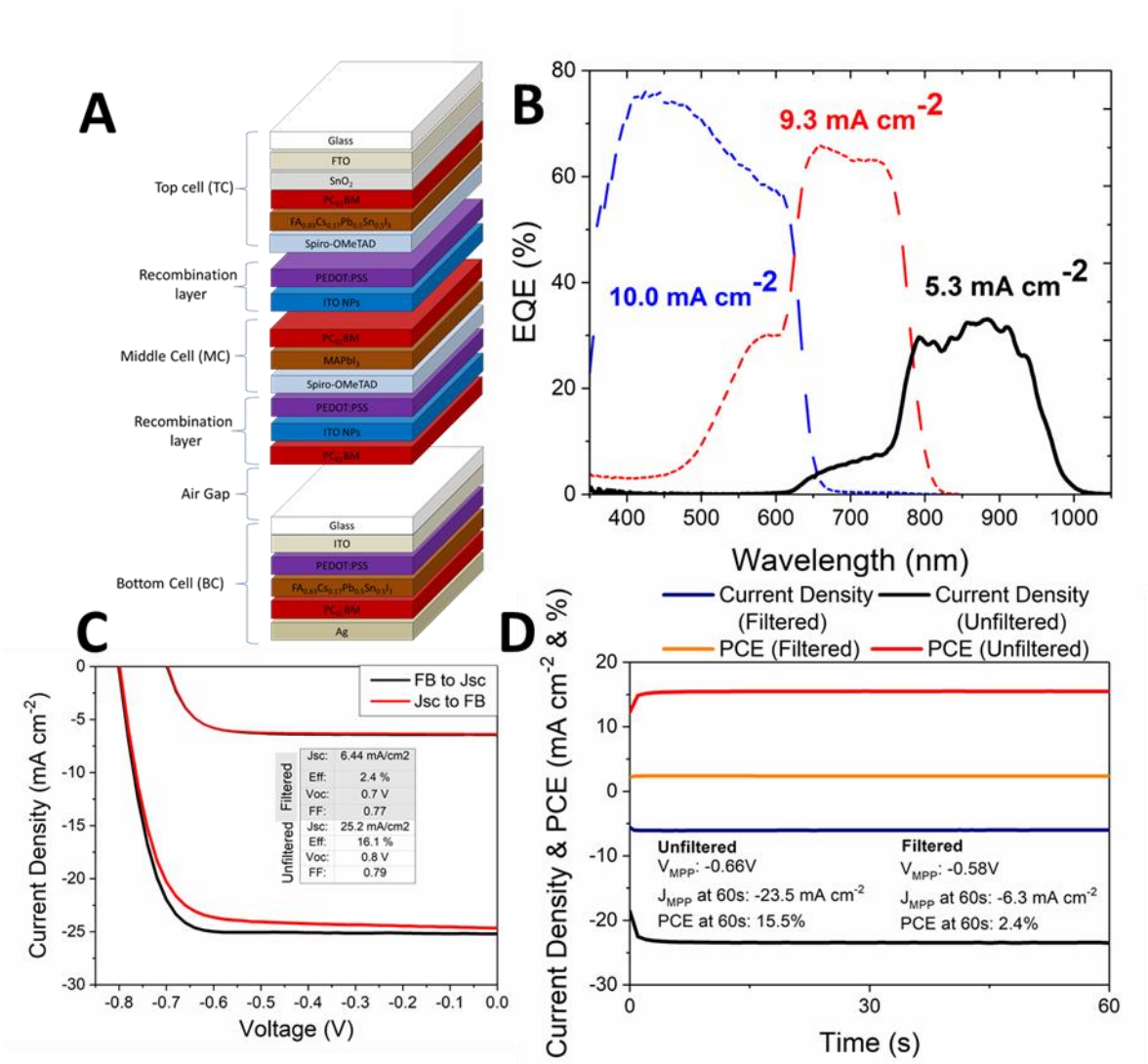


Figure 48: Architecture and device characterization of a $FA_{0.83}Cs_{0.17}Pb_{0.5}Sn_{0.5}I_3$ filtered with a $FA_{0.83}Cs_{0.17}Pb(Br_{0.7}I_{0.3})_3/MAPbI_3$ dual-junction solar cells. *A) Schematics showing the filtering of the $FA_{0.83}Cs_{0.17}Pb_{0.5}Sn_{0.5}I_3$ perovskite with an all-solution processed perovskite/perovskite two-terminal (2T) $FA_{0.83}Cs_{0.17}Pb(Br_{0.7}I_{0.3})_3/MAPbI_3$ tandem perovskite solar cell. B) EQE spectrum for a $FA_{0.83}Cs_{0.17}Pb_{0.5}Sn_{0.5}I_3$ (solid line) filtered with a $FA_{0.83}Cs_{0.17}Pb(Br_{0.7}I_{0.3})_3/MAPbI_3$ dual-junction solar cells, and the integrated current density for the tandem perovskite solar cell. We also show alongside, the EQE spectrum for each sub-cell of the $FA_{0.83}Cs_{0.17}Pb(Br_{0.7}I_{0.3})_3/MAPbI_3$ tandem perovskite solar cell with an opaque electrode, and the integrated current density for the tandem perovskite solar cell. C) J-V characteristics for the champion a $FA_{0.83}Cs_{0.17}Pb_{0.5}Sn_{0.5}I_3$ unfiltered and filtered with a $FA_{0.83}Cs_{0.17}Pb(Br_{0.7}I_{0.3})_3/MAPbI_3$ dual-junction solar cell fabricated, measured at a 0.25 V/s scan rate. C) Photocurrent density and power conversion efficiency measured at the maximum power point for a 60s time span of the $FA_{0.83}Cs_{0.17}Pb_{0.5}Sn_{0.5}I_3$ unfiltered and filtered solar cell. A mismatch factor of 1.486 has been applied to the PCE. The $FA_{0.83}Cs_{0.17}Pb_{0.5}Sn_{0.5}I_3$ was prepared by Matt Klug of the Department of Physics, University of Oxford.*

As reported by Hörantner et al., all-perovskite triple junction solar cells employing perovskite absorbers with similar band gaps to those which we have used in the present work, should be capable

of outperforming single and double-junction efficiencies. The modelling of Hörantner et al. shows that an optimized 1.22 eV band gap material should current match the two wider band gap sub-cells of 2.04 eV and 1.58 eV, delivering a theoretical maximum J_{SC} of 12 mA cm^{-2}, a V_{oc} of 3.54 V and a PCE of 36.6 %.[85] However, this performance can only be obtained with optically transparent interlayers to reduce parasitic absorption and reflection losses. In Fig. S16, we show the optical properties of each interlayer which we have used in our multi-junction stack. We note that the thick ~100nm $PC_{61}BM$ layer employed in the interlayer structure is responsible for the majority of the parasitic absorption and reflection losses.

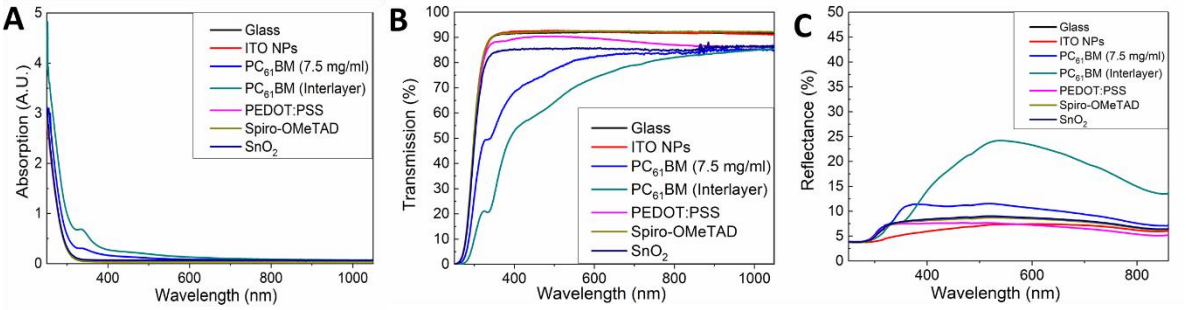


Figure 49: Optical properties of the recombination interlayer and hole and electron accepting layers. *A) Absorption measured from 250nm to 1050nm of glass, indium-tin oxide nanoparticles (ITO NPs), phenyl-C61-butyric acid methyl ester ($PC_{61}BM$), phenyl-C61-butyric acid methyl ester ($PC_{61}BM$), poly(3,4-ethylenedioxythiophene) polystyrene sulfonate (PEDOT:PSS), (2,2',7,7'-tetrakis(N,N'-di-p-methoxyphenylamine)-9,9'-spirobifluorene) (Spiro-OMeTAD). B) Transmission measurement C) Reflectance measurement.*

To assess the true potential of this fully-solution processed all-perovskite multi-junction solar cell architecture, we employed a similar optical and electrical model to that used by Hörantner et al., to simulate this semiconductor stack and reveal where improvements can be made to further increase the performance of multi-junction devices. Using our experimental thicknesses, in combination with the extracted electrical characteristics of the state-of-the-art single junction perovskite cells, we present in Figure 50A-B an estimation of the performance of our tandem stack, and the corresponding modeled external quantum efficiency spectrum. We estimate that our tandem solar cell (sub cells with 1.94 eV and 1.57 eV bandgaps) can be increased to nearly 19% by combining the electrical characteristics of our current champion $FA_{0.83}Cs_{0.17}Pb(Br_{0.7}I_{0.3})_3$ with a best-in-class ACN/MA $MAPbI_3$. We then proceed to model a stack with identical absorber and interlayer materials (shown in Figure 50C-D), but with a state of the art $MAPbI_3$, processed via a DMF/DMSO route, an optimized perovskite thicknesses, interlayers with thickness' down to 50nm, and a MgF_2 anti-reflective coating. These

improvements allow the tandem cell to reach a 21.8% PCE. In Figure 50, we also modeled an optimized stack with an enhanced top cell with improved electrical characteristics, assuming an electroluminescence efficiency (EQE_{EL}) of 1%, a series resistance (R_S) of $4 \cdot 10^{-2}\ \Omega\ cm^2$ and a shunt resistance (R_{SH}) of $10M\Omega\ cm^2$ for the $FA_{0.83}Cs_{0.17}Pb(Br_{0.7}I_{0.3})_3$,[207] which increased the attainable PCE to 26.8%. Figure 50 and Figure 50F reveal the performance of our triple junction architecture, assuming perovskite thicknesses optimized for current-matching, state-of-art $MAPbI_3$ and $FA_{0.6}MA_{0.4}Pb_{0.4}Sn_{0.6}I_3$ perovskite sub-cells, and an anti-reflective coating is added on top. We can see that a 26.7% PCE can be achieved by using optimized thickness, and over 30% PCE triple junction efficiency is within reach by improving the V_{oc} of the top cell. We detail the specific layer thicknesses for each simulation, along with details of these in the supplementary information.

To date, practical all-perovskite monolithic multi-junction solar cells have yet to surpass the efficiency of their state-of-the-art single-junction counterparts. These junctions require significant improvements in light management to reduce reflection and parasitic absorption losses. A central loss is the inability to generate a comparatively high V_{oc} from the wide band gap cells. Furthermore, the layer deposition uniformity has to be improved, in order to enable sub-50 nm thick charge extraction and recombination layers to be realized. As the field progresses, we expect these losses to be mitigated, and hence allow fully-solution processed multi-junction to outperform state of the art single-junction efficiencies.

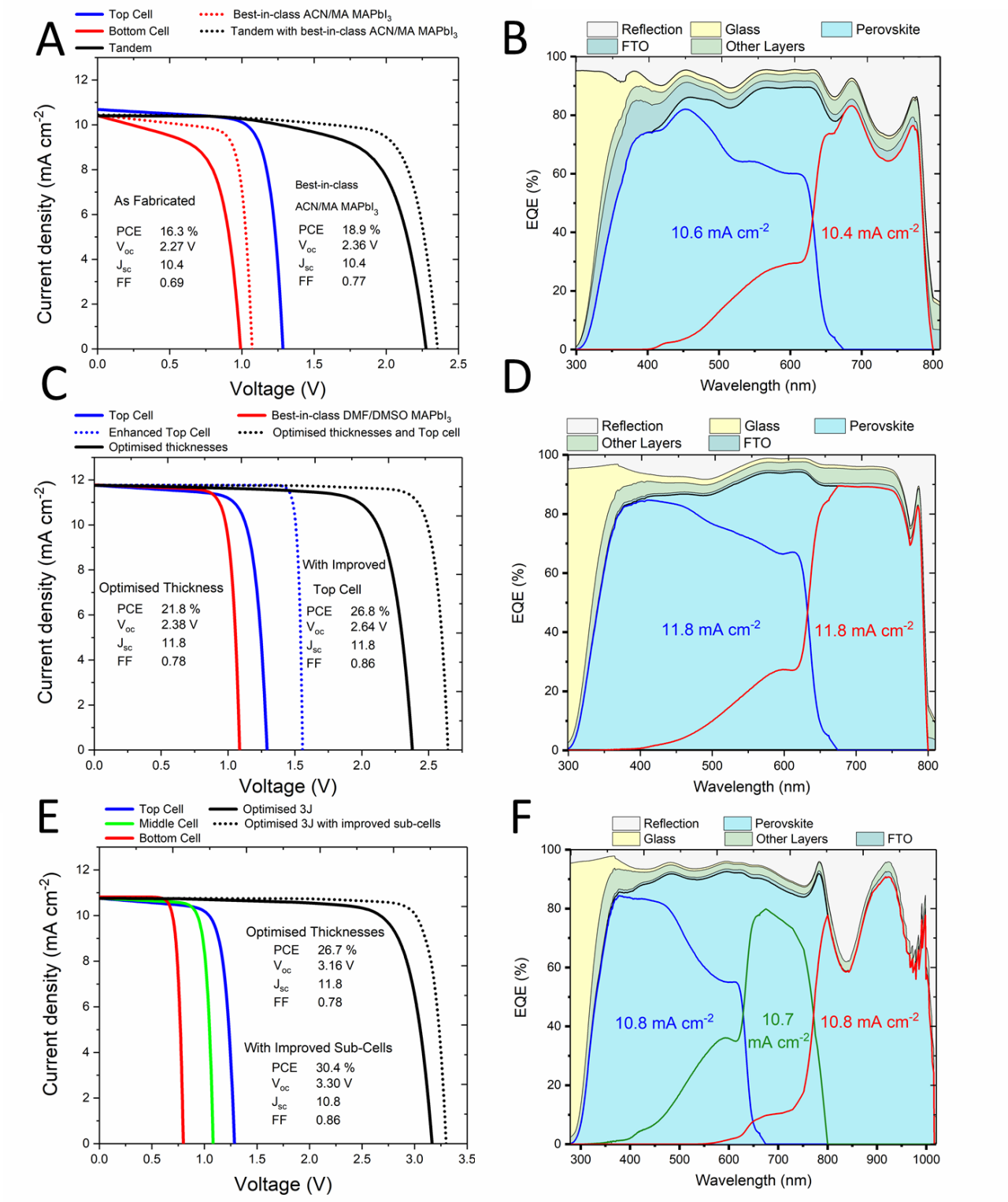


Figure 50: Optical and electrical modelling of multi-junction perovskite solar cells. *A) Calculated J-V characteristics and B) external quantum efficiency (EQE) for the fully-solution processed $FA_{0.83}Cs_{0.17}Pb(Br_{0.7}I_{0.3})_3$/$MAPbI_3$ tandem solar cell, with current single junction experimental data and with best-in-class ACN/MA $MAPbI_3$ single junction cell. C) Calculated J-V characteristics and D) external quantum efficiency of a $FA_{0.83}Cs_{0.17}Pb(Br_{0.7}I_{0.3})_3$/$MAPbI_3$ tandem solar cell assuming optimized layers thicknesses, sub 50 nm interlayer, MgF_2 anti-reflection coating, and an enhanced TC performance. E)*

J-V characteristics and F) EQE for a $FA_{0.83}Cs_{0.17}Pb(Br_{0.7}I_{0.3})_3$/$MAPbI_3$/$FA_{0.6}MA_{0.4}Pb_{0.4}Sn_{0.6}I_3$ triple-junction architecture, assuming optimized layers thicknesses, sub 50 nm interlayer, MgF_2 anti-reflection coating, and an enhanced TC performance. The modeling was carried out by Suhas Mahesh of the Department of Physics, University of Oxford.

6.4. Conclusion and outlook

The fully-solution processed all-perovskite multi-junction solar cells which we have presented open new avenues for the large-scale manufacture of highly efficient multi-junction architectures. We show that these tandem architectures can be achieved using a highly volatile ACN/MA-based solvent system, which enabled sequential stacking of different energy gap perovskite absorbers. Using a highly transparent and effective PEDOT:PSS/ITO NPs recombination layer, we have fabricated the first fully-solution processed monolithic $FA_{0.83}Cs_{0.17}Pb(Br_{0.7}I_{0.3})_3$/$MAPbI_3$ tandem solar cell, reaching a stabilized power conversion efficiency of 15.2%. By adding a narrow band-gap $MAPb_{0.75}Sn_{0.25}I_3$ perovskite junction, we extended the multi-junction's light absorption to 925 nm and fabricated the first triple-junction perovskite solar cell, reaching a record high 2.83 V_{oc}. Further work is needed to reduce the V_{oc} losses for ~2 eV wide-band gap perovskite materials. Improvements in performance of the narrow band gap will also be required to reach the full potential of triple-junction perovskite solar cells.

7. Conclusion and Outlook

The work presented in this thesis is aimed at addressing key concerns when employing organic-inorganic perovskite materials for tandem applications. One critical issue that limited the use of perovskite absorbers for tandem applications was their inability to form stable material for specific band gaps. This is especially crucial for tandem solar cells, to generate equal current densities in all sub-cells. In the case of the $MAPb(I_{(1-x)}Br_x)_3$ perovskite, this system crystalizes in a three-dimensional corner-sharing perovskite structure for every composition between the neat iodide and neat bromide, allowing the ability to tune its band gap from 1.57 to 2.3 eV.[62] However, the methylammonium cation is highly volatile, which results in poor thermal stability, thus limiting its use outside laboratory settings, since solar modules can easily reach temperatures above 65 °C in outdoor conditions. Furthermore, the $MAPb(I_{(1-x)}Br_x)_3$ perovskite system suffers from immediate halide segregation under illumination, which causes electronic disorder, thus lowering the overall attainable voltage. On the other hand, the $FAPb(I_{(1-x)}Br_x)_3$ perovskite structure has been shown to be more thermally stable than the MA-based structure,[63] however, this perovskite system exhibits poor crystallization necessary for mixed-halide compositions to attain a desired band gap for current-matching with c-Si solar cell. Finally, $CsPb(I_{(1-x)}Br_x)_3$, a completely inorganic perovskite system, can sustain temperatures over 300 °C, which allows for impressive thermal stabilities. However, this perovskite system suffers from structural instabilities when at room temperature, where they quickly revert back to a wide-band gap, yellow, non-corner sharing (face-sharing) orthorhombic perovskite structure. Hence, in this thesis we have introduced, characterized and discussed a $FA_{(1-x)}Cs_xPb(I_{(1-y)}Br_y)_3$ mixed-cation lead mixed-halide perovskite system to address these limiting factors for perovskite material in tandem solar cells applications.

In chapter 4, we presented a $FA_{(1-x)}Cs_xPb(I_{(1-y)}Br_y)_3$ mixed-cation lead mixed-halide perovskite system that is suitable for tandem applications. By partially substituting the organic FA^+ cation with an inorganic Cs^+ cation, we were able to crystalize and stabilize the perovskite structure throughout the iodide to bromide compositional range. This perovskite offers a high degree of crystallinity and texturing, which provides a low level of energetic disorder. Furthermore, we show that the $FA_{(1-x)}Cs_xPb(I_{(1-y)}Br_y)_3$ perovskite system mitigates the impact of segregation compared to its methylammonium lead mixed-halide perovskite counterparts. As well by removing the volatile methylammonium (MA^+) cation from the perovskite system, and stabilizing the $FAPbI_3$ structure with Cs^+, greater thermal stability was obtained. With a specific $FA_{0.83}Cs_{0.17}Pb(I_{0.6}Br_{0.4})_3$ perovskite

composition with an optical band gap of 1.74 eV, we were able to achieve an efficiency of 17.1%(16% stabilized) with an open-circuit voltage of 1.2V. Finally, using this novel material, we could achieve a PCE of 22.4% (19.8% stabilized) using a four-terminal perovskite/c-Si tandem architecture.

In chapter 5, we studied the perovskite precursor solution and the role of hydrohalic acids (HI/HBr). Using dynamic light scattering (DLS) measurement, we showed that precursor solutions displayed strong Tyndal effect caused by micron-sized colloids consisting of undissolved lead polyhalide salts. However, these salts can be dissolved with the addition of hydrohalic acids over a period of a few days. Depending on the amount of colloids inherently present in the precursor solution, we observed distinct variations in crystallization kinetics and thin film morphology of the perovskite. We hypothesize that these colloids act as seeds and serve as nucleation sites to initiate the growth of the perovskite crystal. By tuning the colloid concentration in the precursor solution, we were able to obtain highly crystalline material with micro-sized grains and pinhole free morphology. In turn, we observed a significant reduction in microstrain and a two-fold increase in charge-carrier mobilities between films prepared with and without acidic additives, resulting in an improvement in device performance.

In chapter 6, we demonstrated the first two-terminal fully solution-processed all-perovskite multi-junction solar cell. We showed that by using an acetonitrile/methylammonium-based solvent system, we could sequentially process perovskite layers on top of one another, without any solvent damage to the underlying perovskite. By combining $FA_{0.83}Cs_{0.17}Pb(Br_{0.7}I_{0.3})_3$ (1.94 eV) and $MAPbI_3$ (1.57 eV) junctions, we reached two-terminal tandem power conversion efficiencies (PCEs) of over 15 % (stabilized), delivering 2.18 V open-circuit voltage. We also showed the first proof-of-concept triple-junction all perovskite solar cell delivering over 2.83 V. Although the tandem and triple-junction solar cells have yet to surpass single junction efficiencies, these multi-junction solar cell architectures have the potential to surpass the Shockley-Queisser limit. Through optical and electronic modeling, we estimate the conceivable PCE of this triple-junction device architecture to be 26.7%, and show a roadmap to exceed 30% efficiency. Most notably, use of the ACN/MA solvents opens new avenues for fabricating multi-junction solar cells with large-scale, low-cost, solution-processing deposition techniques such as roll-to-roll, doctor-blading and inkjet printing.

To sum up, this thesis has presented critical results and conclusions that will enable perovskite solar cells to be implemented in tandem architectures with c-Si or with another perovskite material to create multi-junction solar cells. These architectures have the potential to surpass conventional single-junction c-Si, which makes perovskite multi-junction solar cells a viable contender for commercial applications. Perovskite solar cells can be fabricated inexpensively due to low material

and processing costs, and combined with high performances, perovskite solar cells have tremendous potential as third-generation solar cells. However, perovskite materials require an additional and crucial property to fully flourish as a photovoltaic absorber: stability. Without this last component, perovskite solar cells will remain as a laboratory experiment, and will never translate into a commercially viable product, produced in large-scale industrial application. This thesis hopes to address these challenges by introducing a highly stable and efficient $FA_{(1-x)}Cs_xPb(I_{(1-y)}Br_y)_3$ perovskite system, suitable for tandem applications. Furthermore, using hydrohalic acids as additives, we described a fabrication method to obtain highly ordered and crystalline perovskite materials. We finally implemented this material in a fully-solution processed multi-junction architecture, compatible with large-scale, low costs deposition techniques. These scientific contributions are geared toward the commercialization of perovskite solar cells, in hopes of revolutionizing the energy market to the point where photovoltaics can outcompete fossil fuels.

8. References

1. Ritchie, H. & Roser, M. Energy Production & Changing Energy Sources. *OurWorldInData.org* (2018). Available at: https://ourworldindata.org/energy-production-and-changing-energy-sources. (Accessed: 22nd February 2018)
2. The World Bank Open Data. GDP per unit of energy use (constant 2011 PPP $ per kg of oil equivalent). (2018). Available at: https://data.worldbank.org/. (Accessed: 23rd February 2018)
3. Fedechko, R. *et al.* Hydrocarbon combustion - Energy Education. Available at: http://energyeducation.ca/encyclopedia/Hydrocarbon_combustion. (Accessed: 24th February 2018)
4. Burton, G. *Salters advanced chemistry. Chemical ideas*. (Heinemann, 2000).
5. Anderson, T. R., Hawkins, E. & Jones, P. D. CO2, the greenhouse effect and global warming: from the pioneering work of Arrhenius and Callendar to today's Earth System Models. *Endeavour* **40,** 178–187 (2016).
6. Lacis, A. A., Schmidt, G. A., Rind, D. & Ruedy, R. A. Atmospheric CO2: principal control knob governing Earth's temperature. *Science* **330,** 356–9 (2010).
7. Bullock, M. A. & Grinspoon, D. H. The stability of climate on Venus. *J. Geophys. Res. Planets* **101,** 7521–7529 (1996).
8. Hughes, T. P. *et al.* Spatial and temporal patterns of mass bleaching of corals in the Anthropocene. *Science* **359,** 80–83 (2018).
9. Hughes, T. P. *et al.* Global warming and recurrent mass bleaching of corals. *Nature* **543,** 373–377 (2017).
10. Preston, B. L. & Jones. Climate Change Impacts on Australia and the Benefits of Early Action to Reduce Global Greenhouse Gas Emissions. (2006).
11. Walker, P. Climate Change as a Driver of Humanitarian Crises and Response. *Feinstein Int. Cent.* (2012).
12. International Renewable Energy Agency (IRENA). Renewable power generation costs in 2017. (2018).
13. Manahan, S. E. *Environmental chemistry*. (CRC Press, 2005).
14. Ribeyron, P.-J. Crystalline silicon solar cells: Better than ever. *Nat. ENERGY* **2,** (2017).
15. National Renewable Energy Laboratory. NREL Efficiency Chart. *https://www.nrel.gov/pv/assets/images/efficiency-chart.png* (2017). Available at: https://www.nrel.gov/pv/assets/images/efficiency-chart.png. (Accessed: 25th November 2017)
16. Kittel, C. *Introduction to solid state physics*. (Wiley, 2005).
17. Kojima, A., Teshima, K., Shirai, Y. & Miyasaka, T. Organometal Halide Perovskites as Visible-Light Sensitizers for Photovoltaic Cells. *J. Am. Chem. Soc.* **131,** 6050–6051 (2009).
18. Lee, M. M., Teuscher, J., Miyasaka, T., Murakami, T. N. & Snaith, H. J. Efficient Hybrid Solar Cells Based on Meso-Superstructured Organometal Halide Perovskites. *Science* **338,** 643–647 (2012).
19. Mitzi, D. B., Wang, S., Feild, C. A., Chess, C. A. & Guloy, A. M. Conducting Layered

Organic-inorganic Halides Containing <110>-Oriented Perovskite Sheets. *Science* **267,** 1473–1476 (1995).

20. Mitzi, D. B., Feild, C. A., Schlesinger, Z. & Laibowitz, R. B. Transport, Optical, and Magnetic Properties of the Conducting Halide Perovskite CH3NH3SnI3. *J. Solid State Chem.* **114,** 159–163 (1995).

21. Mitzi, D. B., Feild, C. A., Harrison, W. T. A. & Guloy, A. M. Conducting tin halides with a layered organic-based perovskite structure. *Nature* **369,** 467–469 (1994).

22. Kim, H.-S. *et al.* Lead Iodide Perovskite Sensitized All-Solid-State Submicron Thin Film Mesoscopic Solar Cell with Efficiency Exceeding 9%. *Sci. Rep.* **2,** 591 (2012).

23. Liu, M., Johnston, M. B. & Snaith, H. J. Efficient planar heterojunction perovskite solar cells by vapour deposition. *Nature* **501,** 395–8 (2013).

24. Shockley, W. & Queisser, H. J. Detailed Balance Limit of Efficiency of *p-n* Junction Solar Cells. *J. Appl. Phys.* **32,** 510–519 (1961).

25. Tiedje, T., Yablonovitch, E., Cody, G. D. & Brooks, B. G. Limiting efficiency of silicon solar cells. *IEEE Trans. Electron Devices* **31,** 711–716 (1984).

26. Hoke, E. T. *et al.* Reversible photo-induced trap formation in mixed-halide hybrid perovskites for photovoltaics. *Chem. Sci.* **6,** 613–617 (2014).

27. Nelson, J. *The Physics of Solar Cells*. (PUBLISHED BY IMPERIAL COLLEGE PRESS AND DISTRIBUTED BY WORLD SCIENTIFIC PUBLISHING CO., 2003). doi:10.1142/p276

28. Würfel, P. & Würfel, U. *Physics of solar cells : from basic principles to advanced concepts*. (Wiley-VCH, 2009).

29. Kittel, C. *Introduction to Solid State Physics.* (Wiley, 2011).

30. Hook, J. R. (John R. . & Hall, H. E. (Henry E. *Solid state physics*. (John Wiley & Sons, 2010).

31. Klocek, P. *Handbook of infrared optical materials*. (M. Dekker, 1991).

32. Van Zeghbroeck, B. V. *Principles of semiconductor devices and heterojunctions*. (Prentice Hall, 2010).

33. Nichols, K. G. & Vernon, E. V. *Transistor Physics*. (Springer Netherlands, 1966).

34. Tong, X. C. *Advanced materials for integrated optical waveguides*.

35. Goetzberger, A. (Adolf), Knobloch, J. & Voss, B. *Crystalline silicon solar cells*. (Wiley, 1998).

36. Yi, T. *et al.* Investigating the Intercalation Chemistry of Alkali Ions in Fluoride Perovskites. *Chem. Mater.* **29,** 1561–1568 (2017).

37. Langley ', R. H., Schmitz, C. K. & Langley, M. B. of Some Fluoride Perovskites An Undergraduate Experiment in Solid State Chemistry.

38. Tiwari, A., Gerhardt, R. A. & Szutkowska, M. *Advanced Ceramic Materials.* (Wiley, 2016).

39. Goldschmidt, V. M. Die Gesetze der Krystallochemie. *Naturwissenschaften* **14,** 477–485 (1926).

40. Travis, W., Glover, E. N. K., Bronstein, H., Scanlon, D. O. & Palgrave, R. G. On the application of the tolerance factor to inorganic and hybrid halide perovskites: a revised system. *Chem. Sci.* **7,** 4548–4556 (2016).

41. Filip, M. R., Eperon, G. E., Snaith, H. J. & Giustino, F. Steric engineering of metal-halide

perovskites with tunable optical band gaps. *Nat. Commun.* **5,** 5757 (2014).

42. Karlin, K. D. & Wiley InterScience (Online service). *Progress in inorganic chemistry. Volume 47*. (Wiley, 1998).

43. Shannon, R. D. & Prewitt, C. T. Effective Ionic Radii in Oxides and Fluorides*. *Acta Cryst. J. Sci. lnstrum. Acta Cryst. Acta Chem. Scand. SFLS. Imp. Coll. Sci. Technol. Acta Cryst. KITAIGORODSKII, k. I. Acta Cryst* **16,** 981–601 (1963).

44. Shannon, R. D. Revised Effective Ionic Radii and Systematic Studies of Interatomie Distances in Halides and Chaleogenides. *Acta Cryst* **32,** (1976).

45. Wells, H. L. Über die Cäsium- und Kalium-Bleihalogenide. *Zeitschrift für Anorg. Chemie* **3,** 195–210 (1893).

46. Topsöe, H. Krystallographisch-chemische Untersuchungen homologer Verbindungen. *Z. Krist.* **8,** 246–296 (1884).

47. Weber, D. CH3NH3PbX3, ein Pb(II)-System mit kubischer Perowskitstruktur CH3NH3PbX3, a Pb(II)-System with Cubic Perovskite Structure. **33,** 1443–1445 (1978).

48. Weber, D. A Sn(II)-System with Cubic Perovskite Structure. *Inst. für Anorg. Chemie der Univ. Stuttgart* **33,** 862–865 (1978).

49. Stranks, S. D. *et al.* Electron-hole diffusion lengths exceeding 1 micrometer in an organometal trihalide perovskite absorber. *Science* **342,** 341–344 (2013).

50. Dvorak, M., Wei, S.-H. & Wu, Z. Origin of the Variation of Exciton Binding Energy in Semiconductors. *Phys. Rev. Lett.* **110,** 16402 (2013).

51. Miyata, A. *et al.* Direct measurement of the exciton binding energy and effective masses for charge carriers in organic–inorganic tri-halide perovskites. *Nat. Phys.* **11,** 582–587 (2015).

52. Lin, Q., Armin, A., Nagiri, R. C. R., Burn, P. L. & Meredith, P. Electro-optics of perovskite solar cells. *Nat. Photonics* **9,** 106–112 (2015).

53. Sun, S. *et al.* The origin of high efficiency in low-temperature solution-processable bilayer organometal halide hybrid solar cells. *Energy Environ. Sci.* **7,** 399–407 (2014).

54. D'Innocenzo, V. *et al.* Excitons versus free charges in organo-lead tri-halide perovskites. *Nat. Commun.* **5,** 3586 (2014).

55. Hirasawa, M., Ishihara, T., Goto, T., Uchida, K. & Miura, N. Magnetoabsorption of the lowest exciton in perovskite-type compound (CH3NH3)PbI3. *Phys. B Condens. Matter* **201,** 427–430 (1994).

56. Even, J., Pedesseau, L. & Katan, C. Analysis of Multivalley and Multibandgap Absorption and Enhancement of Free Carriers Related to Exciton Screening in Hybrid Perovskites. *J. Phys. Chem. C* **118,** 11566–11572 (2014).

57. Shi, D. *et al.* Solar cells. Low trap-state density and long carrier diffusion in organolead trihalide perovskite single crystals. *Science* **347,** 519–22 (2015).

58. Dong, Q. *et al.* Electron-hole diffusion lengths > 175 m in solution-grown CH3NH3PbI3 single crystals. *Science* **347,** 967–970 (2015).

59. Shi, D. *et al.* Low trap-state density and long carrier diffusion in organolead trihalide perovskite single crystals. *Science* **347,** 519–22 (2015).

60. Herz, L. M. Charge-Carrier Dynamics in Organic-Inorganic Metal Halide Perovskites. *Annu. Rev. Phys. Chem.* **67,** 65–89 (2016).

61. De Wolf, S. *et al.* Organometallic Halide Perovskites: Sharp Optical Absorption Edge and Its

Relation to Photovoltaic Performance. *J. Phys. Chem. Lett.* **5,** 1035–1039 (2014).

62. Noh, J. H., Im, S. H., Heo, J. H., Mandal, T. N. & Seok, S. Il. Chemical management for colorful, efficient, and stable inorganic-organic hybrid nanostructured solar cells. *Nano Lett.* **13,** 1764–9 (2013).

63. Eperon, G. E. *et al.* Formamidinium lead trihalide: a broadly tunable perovskite for efficient planar heterojunction solar cells. *Energy Environ. Sci.* **7,** 982–988 (2014).

64. Eperon, G. E. *et al.* Perovskite-perovskite tandem photovoltaics with optimized band gaps. *Science* **354,** 861–865 (2016).

65. Hao, F., Stoumpos, C. C., Chang, R. P. H. & Kanatzidis, M. G. Anomalous Band Gap Behavior in Mixed Sn and Pb Perovskites Enables Broadening of Absorption Spectrum in Solar Cells. *J. Am. Chem. Soc.* **136,** 8094–8099 (2014).

66. Sadhanala, A. *et al.* Preparation of Single-Phase Films of CH3NH3Pb(I1-xBrx)3 with Sharp Optical Band Edges. *J. Phys. Chem. Lett.* **5,** 2501–5 (2014).

67. Yong, S.-M., Tsvetkov, N., Larina, L., Ahn, B. T. & Kim, D. K. Ultrathin SnO2 layer for efficient carrier collection in dye-sensitized solar cells. *Thin Solid Films* **556,** 503–508 (2014).

68. Zhang, Y. *et al.* Two-Step Grain-Growth Kinetics of Sub-7 nm SnO_2 Nanocrystal under Hydrothermal Condition. *J. Phys. Chem. C* **119,** 19505–19512 (2015).

69. Rossbauer, S., Müller, C. & Anthopoulos, T. D. Comparative Study of the N-Type Doping Efficiency in Solution-processed Fullerenes and Fullerene Derivatives. *Adv. Funct. Mater.* **24,** n/a-n/a (2014).

70. Wang, Z. *et al.* Efficient and Air-Stable Mixed-Cation Lead Mixed-Halide Perovskite Solar Cells with n-Doped Organic Electron Extraction Layers. *Adv. Mater.* **29,** 1604186 (2017).

71. Kim, S. S., Bae, S. & Jo, W. H. Performance enhancement of planar heterojunction perovskite solar cells by n-doping of the electron transporting layer. *Chem. Commun.* **51,** 17413–17416 (2015).

72. Wei, P. *et al.* 2-(2-Methoxyphenyl)-1,3-dimethyl-1 *H* -benzoimidazol-3-ium Iodide as a New Air-Stable n-Type Dopant for Vacuum-Processed Organic Semiconductor Thin Films. *J. Am. Chem. Soc.* **134,** 3999–4002 (2012).

73. Naab, B. D. *et al.* Mechanistic Study on the Solution-Phase n-Doping of 1,3-Dimethyl-2-aryl-2,3-dihydro-1 *H* -benzoimidazole Derivatives. *J. Am. Chem. Soc.* **135,** 15018–15025 (2013).

74. Wei, P., Oh, J. H., Dong, G. & Bao, Z. Use of a 1 *H* -Benzoimidazole Derivative as an *n* -Type Dopant and To Enable Air-Stable Solution-Processed *n* -Channel Organic Thin-Film Transistors. *J. Am. Chem. Soc.* **132,** 8852–8853 (2010).

75. Nguyen, W. H., Bailie, C. D., Unger, E. L. & McGehee, M. D. Enhancing the Hole-Conductivity of Spiro-OMeTAD without Oxygen or Lithium Salts by Using Spiro(TFSI) $_2$ in Perovskite and Dye-Sensitized Solar Cells. *J. Am. Chem. Soc.* **136,** 10996–11001 (2014).

76. Noel, N. K. *et al.* A low viscosity, low boiling point, clean solvent system for the rapid crystallisation of highly specular perovskite films. *Energy Environ. Sci.* **10,** 145–152 (2017).

77. Centurioni, E. Generalized matrix method for calculation of internal light energy flux in mixed coherent and incoherent multilayers. *Appl. Opt.* **44,** 7532 (2005).

78. Jain, A. & Kapoor, A. Exact analytical solutions of the parameters of real solar cells using Lambert W -function. *Sol. Energy Mater. Sol. Cells* **81,** 269–277 (2004).

79. Hadipour, A., de Boer, B. & Blom, P. W. M. Device operation of organic tandem solar cells. *Org. Electron.* **9,** 617–624 (2008).

80. K??nig, T. A. F. *et al.* Electrically tunable plasmonic behavior of nanocube-polymer nanomaterials induced by a redox-active electrochromic polymer. *ACS Nano* **8,** 6182–6192 (2014).

81. Ball, J. M. *et al.* Optical properties and limiting photocurrent of thin-film perovskite solar cells. *Energy Environ. Sci.* **8,** 602–609 (2015).

82. Gevaerts, V. S., Koster, L. J. A., Wienk, M. M. & Janssen, R. A. J. Discriminating between Bilayer and Bulk Heterojunction Polymer:Fullerene Solar Cells Using the External Quantum Efficiency. *ACS Appl. Mater. Interfaces* **3,** 3252–3255 (2011).

83. Filipič, M. *et al.* CH3NH3PbI3 perovskite / silicon tandem solar cells: characterization based optical simulations. *Opt. Express* **23,** A263--A278 (2015).

84. Johnson, P. B. & Christy, R. W. Optical Constants of the Noble Metals. *Phys. Rev. B* **6,** 4370–4379 (1972).

85. Hörantner, M. T. *et al.* The Potential of Multijunction Perovskite Solar Cells. *ACS Energy Lett.* **2,** 2506–2513 (2017).

86. Löper, P. *et al.* Complex Refractive Index Spectra of $CH_3NH_3PbI_3$ Perovskite Thin Films Determined by Spectroscopic Ellipsometry and Spectrophotometry. *J. Phys. Chem. Lett.* **6,** 66–71 (2015).

87. Shin, S. S. *et al.* Colloidally prepared La-doped BaSnO 3 electrodes for efficient , photostable perovskite solar cells. **6620,** (2017).

88. Prasanna, R. *et al.* Band Gap Tuning via Lattice Contraction and Octahedral Tilting in Perovskite Materials for Photovoltaics. *J. Am. Chem. Soc.* **139,** 11117–11124 (2017).

89. Shin, S. S. *et al.* Colloidally prepared La-doped BaSnO3electrodes for efficient, photostable perovskite solar cells. *Science* **356,** 167–171 (2017).

90. Robinson, I. & Harder, R. Coherent X-ray diffraction imaging of strain at the nanoscale. *Nat. Mater.* **8,** 291–298 (2009).

91. Pramanick, A. *et al.* Microdomain dynamics in single-crystal <math> <mrow> <mi>BaTiO<mi><mn>$_3$</mn></msub> </mrow> </math> during paraelectric-ferroelectric phase transition measured with time-of-flight neutron scattering. *Phys. Rev. B* **92,** 174103 (2015).

92. Williamson, G. . & Hall, W. . X-ray line broadening from filed aluminium and wolfram. *Acta Metall.* **1,** 22–31 (1953).

93. Zhao, Y. & Zhang, J. Microstrain and grain-size analysis from diffraction peak width and graphical derivation of high-pressure thermomechanics. *J. Appl. Crystallogr.* **41,** 1095–1108 (2008).

94. Shah, A. Photovoltaic Technology: The Case for Thin-Film Solar Cells. *Science* **285,** 692–698 (1999).

95. Kagan, C. R. Organic-Inorganic Hybrid Materials as Semiconducting Channels in Thin-Film Field-Effect Transistors. *Science* **286,** 945–947 (1999).

96. Kojima, A., Teshima, K., Shirai, Y. & Miyasaka, T. Organometal Halide Perovskites as Visible-Light Sensitizers for Photovoltaic Cells. *J. Am. Chem. Soc.* **131,** 6050–6051 (2009).

97. Burschka, J. *et al.* Sequential deposition as a route to high-performance perovskite-sensitized solar cells. *Nature* **499,** 316–9 (2013).

98. Green, M. a., Ho-Baillie, A. & Snaith, H. J. The emergence of perovskite solar cells. *Nat. Photonics* **8,** 506–514 (2014).

99. Jeon, N. J. *et al.* Solvent engineering for high-performance inorganic-organic hybrid perovskite solar cells. *Nat. Mater.* **13,** 1–7 (2014).

100. Jeon, N. J. *et al.* Compositional engineering of perovskite materials for high-performance solar cells. *Nature* **517,** 476–480 (2015).

101. Yang, W. S. *et al.* High-performance photovoltaic perovskite layers fabricated through intramolecular exchange. *Science* **348,** 1234–1237 (2015).

102. Conings, B. *et al.* Intrinsic Thermal Instability of Methylammonium Lead Trihalide Perovskite. *Adv. Energy Mater.* **5,** n/a-n/a (2015).

103. Rehman, W. *et al.* Charge-Carrier Dynamics and Mobilities in Formamidinium Lead Mixed-Halide Perovskites. *Adv. Mater.* n/a-n/a (2015). doi:10.1002/adma.201502969

104. Bailie, C. D. *et al.* Semi-transparent perovskite solar cells for tandems with silicon and CIGS. *Energy Environ. Sci.* **8,** 956–963 (2015).

105. Löper, P. *et al.* Organic-inorganic halide perovskite/crystalline silicon four-terminal tandem solar cells. *Phys. Chem. Chem. Phys.* **17,** 1619–29 (2015).

106. Albrecht, S. *et al.* Monolithic perovskite/silicon-heterojunction tandem solar cells processed at low temperature. *Energy Environ. Sci.* **9,** 81–88 (2016).

107. Binek, A., Hanusch, F. C., Docampo, P. & Bein, T. Stabilization of the Trigonal High Temperature Phase of Formamidinium Lead Iodide. *J. Phys. Chem. Lett.* **6,** 150316103833007 (2015).

108. Pang, S. *et al.* NH 2 CH═NH 2 PbI 3 : An Alternative Organolead Iodide Perovskite Sensitizer for Mesoscopic Solar Cells. *Chem. Mater.* **26,** 1485–1491 (2014).

109. Stoumpos, C. C., Malliakas, C. D. & Kanatzidis, M. G. Semiconducting tin and lead iodide perovskites with organic cations: phase transitions, high mobilities, and near-infrared photoluminescent properties. *Inorg. Chem.* **52,** 9019–38 (2013).

110. Pellet, N. *et al.* Mixed-organic-cation perovskite photovoltaics for enhanced solar-light harvesting. *Angew. Chem. Int. Ed. Engl.* **53,** 3151–7 (2014).

111. Stranks, S. D. & Snaith, H. J. Metal-halide perovskites for photovoltaic and light-emitting devices. *Nat. Nanotechnol.* **10,** 391–402 (2015).

112. Lee, J.-W. *et al.* Formamidinium and Cesium Hybridization for Photo- and Moisture-Stable Perovskite Solar Cell. *Adv. Energy Mater.* **5,** 1501310 (2015).

113. Choi, H. *et al.* Cesium-doped methylammonium lead iodide perovskite light absorber for hybrid solar cells. *Nano Energy* **7,** 80–85 (2014).

114. Tvingstedt, K. *et al.* Radiative efficiency of lead iodide based perovskite solar cells. *Sci. Rep.* **4,** 6071 (2014).

115. De Wolf, S. *et al.* Organometallic Halide Perovskites: Sharp Optical Absorption Edge and Its Relation to Photovoltaic Performance. *J. Phys. Chem. Lett.* **5,** 1035–1039 (2014).

116. Milot, R. L., Eperon, G. E., Snaith, H. J., Johnston, M. B. & Herz, L. M. Temperature-Dependent Charge-Carrier Dynamics in CH 3 NH 3 PbI 3 Perovskite Thin Films. *Adv. Funct. Mater.* n/a-n/a (2015). doi:10.1002/adfm.201502340

117. Tress, W. *et al.* Predicting the Open-Circuit Voltage of CH 3 NH 3 PbI 3 Perovskite Solar Cells Using Electroluminescence and Photovoltaic Quantum Efficiency Spectra: the Role of Radiative and Non-Radiative Recombination. *Adv. Energy Mater.* **5,** n/a-n/a (2015).

118. Snaith, H. J. Estimating the Maximum Attainable Efficiency in Dye-Sensitized Solar Cells. *Adv. Funct. Mater.* **20,** 13–19 (2010).

119. Rau, U. Reciprocity relation between photovoltaic quantum efficiency and electroluminescent emission of solar cells. *Phys. Rev. B* **76,** 85303 (2007).

120. Mazzarella, L. *et al.* p-type microcrystalline silicon oxide emitter for silicon heterojunction solar cells allowing current densities above 40 mA/cm2. *Appl. Phys. Lett.* **106,** 23902 (2015).

121. National Renewable Energy Laboratory. NREL Efficiency Chart. *http://www.nrel.gov/ncpv/images/efficiency_chart.jpg* (2016).

122. Yang, W. S. *et al.* Iodide management in formamidinium-lead-halide-based perovskite layers for efficient solar cells. *Science* **356,** 1376–1379 (2017).

123. Wei, Z., Chen, H., Yan, K. & Yang, S. Inkjet Printing and Instant Chemical Transformation of a $CH_3NH_3PbI_3$/Nanocarbon Electrode and Interface for Planar Perovskite Solar Cells. *Angew. Chemie Int. Ed.* **53,** 13239–13243 (2014).

124. Li, S.-G. *et al.* Inkjet printing of $CH_3NH_3PbI_3$ on a mesoscopic TiO 2 film for highly efficient perovskite solar cells. *J. Mater. Chem. A* **3,** 9092–9097 (2015).

125. Barrows, A. T. *et al.* Efficient planar heterojunction mixed-halide perovskite solar cells deposited via spray-deposition. *Energy Environ. Sci.* **7,** 2944–2950 (2014).

126. Kagan, C. R., Mitzi, D. B. & Dimitrakopoulos, C. D. Organic-Inorganic Hybrid Materials as Semiconducting Channels in Thin-Film Field-Effect Transistors. *Science* **286,** 945–947 (1999).

127. Tan, Z.-K. *et al.* Bright light-emitting diodes based on organometal halide perovskite. *Nat. Nanotechnol.* **9,** 687–692 (2014).

128. Dou, L. *et al.* Solution-processed hybrid perovskite photodetectors with high detectivity. *Nat. Commun.* **5,** 5404 (2014).

129. Fang, Y., Dong, Q., Shao, Y., Yuan, Y. & Huang, J. Highly narrowband perovskite single-crystal photodetectors enabled by surface-charge recombination. *Nat. Photonics* **9,** 679–686 (2015).

130. Chang, C.-Y. *et al.* Tuning Perovskite Morphology by Polymer Additive for High Efficiency Solar Cell. *ACS Appl. Mater. Interfaces* **7,** 4955–4961 (2015).

131. Chen, C.-C. *et al.* Perovskite/polymer monolithic hybrid tandem solar cells utilizing a low-temperature, full solution process. *Mater. Horiz.* **2,** 203–211 (2015).

132. Xu, J. *et al.* Perovskite–fullerene hybrid materials suppress hysteresis in planar diodes. *Nat. Commun.* **6,** 7081 (2015).

133. Wang, J. T.-W. *et al.* Efficient perovskite solar cells by metal ion doping. *Energy Environ. Sci.* **9,** 2892–2901 (2016).

134. Gong, X. *et al.* Controllable Perovskite Crystallization by Water Additive for High-Performance Solar Cells. *Adv. Funct. Mater.* **25,** 6671–6678 (2015).

135. Zhang, W. *et al.* Enhanced optoelectronic quality of perovskite thin films with hypophosphorous acid for planar heterojunction solar cells. *Nat. Commun.* **6,** 10030 (2015).

136. Li, X. *et al.* Improved performance and stability of perovskite solar cells by crystal crosslinking with alkylphosphonic acid ω-ammonium chlorides. *Nat. Chem.* **7,** 703–711 (2015).

137. Soe, C. M. M. *et al.* Room Temperature Phase Transition in Methylammonium Lead Iodide Perovskite Thin Films Induced by Hydrohalic Acid Additives. *ChemSusChem* **9,** 2656–2665 (2016).

138. Pan, J. *et al.* Room-Temperature, Hydrochloride-Assisted, One-Step Deposition for Highly Efficient and Air-Stable Perovskite Solar Cells. *Adv. Mater.* **28,** 8309–8314 (2016).

139. Wang, F., Yu, H., Xu, H. & Zhao, N. HPbI $_3$: A New Precursor Compound for Highly Efficient Solution-Processed Perovskite Solar Cells. *Adv. Funct. Mater.* **25,** 1120–1126 (2015).

140. Nayak, P. K. *et al.* Mechanism for rapid growth of organic?inorganic halide perovskite crystals. *Nat. Commun.* **7,** 13303 (2016).

141. Yan, K. *et al.* Hybrid Halide Perovskite Solar Cell Precursors: Colloidal Chemistry and Coordination Engineering behind Device Processing for High Efficiency. *J. Am. Chem. Soc.* **137,** 4460–4468 (2015).

142. McMeekin, D. P. *et al.* A mixed-cation lead mixed-halide perovskite absorber for tandem solar cells. *Science* **351,** 151–5 (2016).

143. Li, Z. *et al.* Stabilizing Perovskite Structures by Tuning Tolerance Factor: Formation of Formamidinium and Cesium Lead Iodide Solid-State Alloys. *Chem. Mater.* **28,** 284–292 (2016).

144. Yi, C. *et al.* Entropic Stabilization of Mixed A-Cation ABX_3 Metal Halide Perovskites for High Performance Perovskite Solar Cells. *Energy Environ. Sci.* **9,** 656–662 (2015).

145. Eperon, G. E. *et al.* Inorganic caesium lead iodide perovskite solar cells. *J. Mater. Chem. A* **3,** 19688–19695 (2015).

146. Wang, Q. *et al.* Scaling behavior of moisture-induced grain degradation in polycrystalline hybrid perovskite thin films. *Energy Environ. Sci.* **10,** 516–522 (2017).

147. Bi, D. *et al.* Polymer-templated nucleation and crystal growth of perovskite films for solar cells with efficiency greater than 21%. *Nat. Energy* **1,** 16142 (2016).

148. Mullin, J. W. (John W. *Crystallization.* (Butterworth-Heinemann, 2001).

149. Bi, C. *et al.* Non-wetting surface-driven high-aspect-ratio crystalline grain growth for efficient hybrid perovskite solar cells. *Nat. Commun.* **6,** 7747 (2015).

150. Hidalgo-Álvarez, R. *Structure and functional properties of colloidal systems*. (CRC Press, 2010).

151. Fisher, J. C., Hollomon, J. H. & Turnbull, D. Nucleation. *J. Appl. Phys.* **19,** 775–784 (1948).

152. Thanh, N. T. K., Maclean, N. & Mahiddine, S. Mechanisms of Nucleation and Growth of Nanoparticles in Solution. *Chem. Rev.* **114,** 7610–7630 (2014).

153. Zheng, X. *et al.* Improved Phase Stability of Formamidinium Lead Triiodide Perovskite by Strain Relaxation. *ACS Energy Lett.* **1,** 1014–1020 (2016).

154. Yang, Z. *et al.* Stabilized Wide Bandgap Perovskite Solar Cells by Tin Substitution. *Nano Lett.* **16,** 7739–7747 (2016).

155. Zheng, X. *et al.* Improved Phase Stability of Formamidinium Lead Triiodide Perovskite by Strain Relaxation. *ACS Energy Lett.* **1,** 1014–1020 (2016).

156. Wojciechowski, K. *et al.* Cross-Linkable Fullerene Derivatives for Solution-Processed n–i–p Perovskite Solar Cells. *ACS Energy Lett.* **1,** 648–653 (2016).

157. Deb, N. *et al.* Thermo-cross-linkable fullerene for long-term stability of photovoltaic devices. *J. Mater. Chem. A* **3,** 21856–21863 (2015).

158. Jia, Y., Kerner, R. A., Grede, A. J., Rand, B. P. & Giebink, N. C. Continuous-wave lasing in an organic–inorganic lead halide perovskite semiconductor. *Nat. Photonics* **11,** 784–788 (2017).

159. Zhu, H. *et al.* Lead halide perovskite nanowire lasers with low lasing thresholds and high quality factors. *Nat. Mater.* **14,** 636–642 (2015).

160. Malinkiewicz, O. *et al.* Perovskite solar cells employing organic charge-transport layers. *Nat. Photonics* **8,** 128–132 (2013).

161. Im, J.-H., Lee, C.-R., Lee, J.-W., Park, S.-W. & Park, N.-G. 6.5% Efficient Perovskite Quantum-Dot-Sensitized Solar Cell. *Nanoscale* **3,** 4088–93 (2011).

162. McMeekin, D. P. *et al.* A mixed-cation lead mixed-halide perovskite absorber for tandem solar cells. *Science* **351,** 151–155 (2016).

163. Beal, R. E. *et al.* Cesium Lead Halide Perovskites with Improved Stability for Tandem Solar Cells. *J. Phys. Chem. Lett.* **7,** 746–51 (2016).

164. Sutton, R. J. *et al.* Bandgap-Tunable Cesium Lead Halide Perovskites with High Thermal Stability for Efficient Solar Cells. *Adv. Energy Mater.* **6,** n/a-n/a (2016).

165. Rajagopal, A. *et al.* Highly Efficient Perovskite-Perovskite Tandem Solar Cells Reaching 80% of the Theoretical Limit in Photovoltage. *Adv. Mater.* **29,** 1702140 (2017).

166. Chen, S. *et al.* Exploring the Stability of Novel Wide Bandgap Perovskites by a Robot Based High Throughput Approach. *Adv. Energy Mater.* 1701543 (2017). doi:10.1002/aenm.201701543

167. Noel, N. K. *et al.* Lead-free organic–inorganic tin halide perovskites for photovoltaic applications. *Energy Environ. Sci.* **7,** 3061–3068 (2014).

168. Yang, Z. *et al.* Stable Low-Bandgap Pb-Sn Binary Perovskites for Tandem Solar Cells. *Adv. Mater.* **28,** 8990–8997 (2016).

169. Rajagopal, A., Liang, P.-W., Chueh, C.-C., Yang, Z. & Jen, A. K.-Y. Defect Passivation via a Graded Fullerene Heterojunction in Low-Bandgap Pb–Sn Binary Perovskite Photovoltaics. *ACS Energy Lett.* **2,** 2531–2539 (2017).

170. Li, L. *et al.* High efficiency planar Sn–Pb binary perovskite solar cells: controlled growth of large grains via a one-step solution fabrication process. *J. Mater. Chem. C* **5,** 2360–2367 (2017).

171. Lee, S. & Kang, D.-W. Highly Efficient and Stable Sn-Rich Perovskite Solar Cells by Introducing Bromine. *ACS Appl. Mater. Interfaces* **9,** 22432–22439 (2017).

172. Liao, W. *et al.* Fabrication of Efficient Low-Bandgap Perovskite Solar Cells by Combining Formamidinium Tin Iodide with Methylammonium Lead Iodide. *J. Am. Chem. Soc.* **138,** 12360–12363 (2016).

173. Eames, C. *et al.* Ionic transport in hybrid lead iodide perovskite solar cells. *Nat. Commun.* **6,** 7497 (2015).

174. Bailie, C. D. *et al.* Semi-transparent perovskite solar cells for tandems with silicon and CIGS. *Energy Environ. Sci.* **8,** 956–963 (2015).

175. Werner, J. *et al.* Efficient Near-Infrared-Transparent Perovskite Solar Cells Enabling Direct Comparison of 4-Terminal and Monolithic Perovskite/Silicon Tandem Cells. *ACS Energy Lett.* **1,** 474–480 (2016).

176. Pisoni, S. *et al.* Flexible NIR-transparent perovskite solar cells for all-thin-film tandem photovoltaic devices. *J. Mater. Chem. A* **5,** 13639–13647 (2017).

177. Zhao, D. *et al.* Low-bandgap mixed tin–lead iodide perovskite absorbers with long carrier lifetimes for all-perovskite tandem solar cells. *Nat. Energy* **2,** 17018 (2017).

178. Todorov, T., Gershon, T., Gunawan, O., Sturdevant, C. & Guha, S. Perovskite-kesterite monolithic tandem solar cells with high open-circuit voltage. *Appl. Phys. Lett.* **105,** 173902 (2014).

179. Werner, J. *et al.* Efficient Monolithic Perovskite/Silicon Tandem Solar Cell with Cell Area >1 cm ^{2}. *J. Phys. Chem. Lett.* **7,** 161–166 (2016).

180. Forgács, D. *et al.* Efficient Monolithic Perovskite/Perovskite Tandem Solar Cells. *Adv. Energy Mater.* **7,** 1602121 (2017).

181. Bush, K. A. *et al.* 23.6%-efficient monolithic perovskite/silicon tandem solar cells with improved stability. *Nat. Energy* **2,** 17009 (2017).

182. Sheng, R. *et al.* Monolithic Wide Band Gap Perovskite/ Perovskite Tandem Solar Cells with Organic Recombination Layers. *J. Phys. Chem. C* acs.jpcc.7b05517 (2017). doi:10.1021/acs.jpcc.7b05517

183. Zhao, D. *et al.* Four-Terminal All-Perovskite Tandem Solar Cells Achieving Power Conversion Efficiencies Exceeding 23%. *ACS Energy Lett.* 305–306 (2018). doi:10.1021/acsenergylett.7b01287

184. Jiang, F. *et al.* A two-terminal perovskite/perovskite tandem solar cell. *J. Mater. Chem. A* **4,** 1208–1213 (2016).

185. Wu, Y. *et al.* Monolithic perovskite/silicon-homojunction tandem solar cell with over 22% efficiency. *Energy Environ. Sci.* **10,** 2472–2479 (2017).

186. Ellmer, K. Past achievements and future challenges in the development of optically transparent electrodes. *Nat. Photonics* **6,** 809–817 (2012).

187. Tang, Z. *et al.* Hysteresis-free perovskite solar cells made of potassium-doped organometal halide perovskite. *Sci. Rep.* **7,** 12183 (2017).

188. Nam, J. K. *et al.* Potassium Incorporation for Enhanced Performance and Stability of Fully Inorganic Cesium Lead Halide Perovskite Solar Cells. *Nano Lett.* **17,** 2028–2033 (2017).

189. Muzammal uz Zaman, M. *et al.* Potassium doped methylammonium lead iodide (MAPbI3) thin films as a potential absorber for perovskite solar cells; structural, morphological, electronic and optoelectric properties. *Phys. B Condens. Matter* **522,** 57–65 (2017).

190. Bu, T. *et al.* A novel quadruple-cation absorber for universal hysteresis elimination for high efficiency and stable perovskite solar cells. *Energy Environ. Sci.* **10,** 2509–2515 (2017).

191. Abdi-Jalebi, M. *et al.* Maximizing and stabilizing luminescence from halide perovskites with potassium passivation. *Nature* **555,** 497–501 (2018).

192. Abdi-Jalebi, M. *et al.* Maximising and Stabilising Luminescence in Metal Halide Perovskite Device Structures.

193. Snaith, H. J. *et al.* Anomalous Hysteresis in Perovskite Solar Cells. *J. Phys. Chem. Lett.* **5,** 1511–1515 (2014).

194. McMeekin, D. P. *et al.* Crystallization Kinetics and Morphology Control of Formamidinium-Cesium Mixed-Cation Lead Mixed-Halide Perovskite via Tunability of the Colloidal Precursor Solution. *Adv. Mater.* 1607039 (2017). doi:10.1002/adma.201607039

195. Roldán-Carmona, C. *et al.* High efficiency methylammonium lead triiodide perovskite solar cells: the relevance of non-stoichiometric precursors. *Energy Environ. Sci.* **8,** 3550–3556 (2015).

196. Yang, M. *et al.* Perovskite ink with wide processing window for scalable high-efficiency solar cells. *Nat. Energy* **2,** 17038 (2017).

197. Bi, D. *et al.* Efficient luminescent solar cells based on tailored mixed-cation perovskites. *Sci. Adv.* **2,** e1501170–e1501170 (2016).

198. Chen, Q. *et al.* Controllable Self-Induced Passivation of Hybrid Lead Iodide Perovskites

toward High Performance Solar Cells. *Nano Lett.* **14,** 4158–4163 (2014).

199. Jacobsson, T. J. *et al.* Unreacted PbI_2 as a Double-Edged Sword for Enhancing the Performance of Perovskite Solar Cells. *J. Am. Chem. Soc.* **138,** 10331–10343 (2016).

200. Leijtens, T., Lim, J., Teuscher, J., Park, T. & Snaith, H. J. Charge Density Dependent Mobility of Organic Hole-Transporters and Mesoporous TiO_2 Determined by Transient Mobility Spectroscopy: Implications to Dye-Sensitized and Organic Solar Cells. *Adv. Mater.* **25,** 3227–3233 (2013).

201. Marshall, K. P., Walker, M., Walton, R. I. & Hatton, R. A. Enhanced stability and efficiency in hole-transport-layer-free CsSnI3 perovskite photovoltaics. *Nat. Energy* **1,** 16178 (2016).

202. Lee, S. J. *et al.* Fabrication of Efficient Formamidinium Tin Iodide Perovskite Solar Cells through SnF_2 –Pyrazine Complex. *J. Am. Chem. Soc.* **138,** 3974–3977 (2016).

203. Kumar, M. H. *et al.* Lead-Free Halide Perovskite Solar Cells with High Photocurrents Realized Through Vacancy Modulation. *Adv. Mater.* **26,** 7122–7127 (2014).

204. Kontos, A. G. *et al.* Structural Stability, Vibrational Properties, and Photoluminescence in $CsSnI_3$ Perovskite upon the Addition of SnF_2. *Inorg. Chem.* **56,** 84–91 (2017).

205. and, J. D. S. N. & Blanchard*, G. J. Formation of Gold Nanoparticles Using Amine Reducing Agents. (2006). doi:10.1021/LA060045Z

206. Song, T.-B., Yokoyama, T., Aramaki, S. & Kanatzidis, M. G. Performance Enhancement of Lead-Free Tin-Based Perovskite Solar Cells with Reducing Atmosphere-Assisted Dispersible Additive. *ACS Energy Lett.* **2,** 897–903 (2017).

207. Hörantner, M. T. & Snaith, H. J. Predicting and optimising the energy yield of perovskite-on-silicon tandem solar cells under real world conditions. *Energy Environ. Sci.* **10,** 1983–1993 (2017).